



**TÉCNICO**  
LISBOA

# **Surrogate-based Multidisciplinary Design Optimization of a Canard Configuration VTOL UAV**

**Tiago Alexandre Salreta de Jesus**

Thesis to obtain the Master of Science Degree in

## **Aerospace Engineering**

Supervisors: Prof. Afzal Suleman  
Dr. José Lobo do Vale

### **Examination Committee**

Chairperson: Prof. Fernando José Parracho Lau  
Supervisor: Prof. Afzal Suleman  
Member of the Committee: Prof. Frederico José Prata Rente Reis Afonso

**January 2021**



## **Acknowledgments**

First I would like to express my gratitude to Professor Afzal Suleman for the provided opportunity to work on my master thesis at the university of Victoria and to experience a different culture in Canada, and also for always being available to help and support us whenever we needed.

I would also like to thank the whole team from the Center for Aerospace Research that welcomed us and facilitated our integration in the group, specially Dr. José Vale for guiding me through the whole process, for all the patience, flexibility and experienced advice.

A huge appreciation to my parents and closest family who raised me and for all love and sacrifice that allowed me to get here.

Lastly, it could not go without mentioning all my friends that accompanied me through this journey in the last five years, both those who shared this experience in Canada with me, as well as the ones at home, with whom I enjoyed good moments, good laughs, eased more stressful times and for being partners in work and adventures.



## Resumo

Esta tese aborda uma otimização multidisciplinar (MDO), com base em modelos de aproximação, de um veículo aéreo não tripulado (UAV), com uma configuração canard de asa fixa, com capacidade de decolagem e aterragem vertical (VTOL). Realiza-se uma otimização aeroestrutural de multifidelidade detalhada, incluindo a asa, canard, superfícies verticais e fuselagem. A otimização é motivada principalmente pela missão atribuída e pelos requisitos de estabilidade e manobrabilidade, com o objetivo de maximizar o alcance.

Modelos de aproximação com base em modelos Kriging são gerados quer para a função objetivo, quer para as restrições. De modo a melhorar os modelos e evitar uma exploração excessiva do espaço de soluções, são utilizados métodos de procura que combinam métodos como WB2 (critério de Watson e Barnes) e *Expected Improvement* (EI) durante a procura de um ótimo global, ou um ótimo local que permita melhorias significativas. A evolução das configurações e dos modelos de aproximação ao longo do processo iterativo de otimização são ilustradas através de tabelas e gráficos relativos a parâmetros de performance, seguidos de uma análise descritiva bem como uma discussão da evolução de todo o processo juntamente com os resultados obtidos.

Uma análise da melhor configuração alcançada fornece uma estimativa da massa estrutural que corresponde a 16.84% da massa máxima de decolagem (MTOM), uma velocidade de perda de  $27.61\text{m/s}$  além de um coeficiente de planeio ( $L/D$ ) de 16.59 em cruzeiro, e 7.90 em velocidade máxima.

**Palavras-chave:** Multiobjetivo, multifidelidade, aeroestrutural, Kriging, *Expected Improvement*, projeto aeronáutico



## Abstract

This thesis presents a surrogate based multidisciplinary design optimization (MDO) of a fixed-wing canard configuration vertical take-off and landing (VTOL) unmanned aerial vehicle (UAV). A detailed multi-fidelity aero-structural optimization including wing, canard, vertical surfaces as well as fuselage is carried out primarily motivated by the envisioned mission profile and stability and maneuverability requirements with the objective of maximizing range.

Kriging based surrogate models are generated for both objective function and constraints. A combination of WB2 (Watson and Barnes criterion) and Expected Improvement (EI) search methods with engineering knowledge is used for surrogate models enrichment and avoid excessive exploration of the design space while aiming to achieve the global, or a local optimum that allows significant improvements. The evolution of the configurations, along with the approximation models during the iterative optimization process are illustrated using tables and plots showing performance metrics parameters, followed by an examination and discussion of the whole process evolution along with the obtained results.

An analysis of the best configuration reached provides an estimation of a represented structural mass of 16.84% of the Maximum Take-Off Mass (MTOM), a stall speed of  $27.61\text{m/s}$  in addition to lift-to-drag ratios ( $L/D$ ) of 16.59 in cruise and 7.90 in dash.

**Keywords:** Multiobjective, multi-fidelity, aero-structural, Kriging, Expected Improvement, aircraft design



I declare that this document is an original work of my own authorship and that it fulfills all the requirements of the Code of Conduct and Good Practices of the Universidade de Lisboa.



# Contents

Acknowledgments . . . . .	iii
Resumo . . . . .	v
Abstract . . . . .	vii
List of Tables . . . . .	xiii
List of Figures . . . . .	xv
Nomenclature . . . . .	xvii
Glossary . . . . .	xxiii
<b>1 Introduction</b>	<b>1</b>
1.1 Motivation . . . . .	1
1.2 Project Overview/Conceptual Design Synthesis . . . . .	1
1.3 State of the art . . . . .	2
1.4 Objectives . . . . .	5
1.5 Thesis Outline . . . . .	5
<b>2 Theoretical Background</b>	<b>7</b>
2.1 Multidisciplinary Analysis . . . . .	7
2.1.1 Structural Analysis . . . . .	7
2.1.2 Aerodynamic Analysis . . . . .	9
2.2 Optimization Problem . . . . .	13
2.2.1 Basic concepts and problem formulation . . . . .	13
2.2.2 Multiobjective Optimization-Pareto frontier and Weighted sum method [97] . . . . .	14
2.3 Sampling Plan . . . . .	15
2.3.1 Latin-Hypercube Sampling . . . . .	15
2.3.2 Space-filling metrics - Pairwise Distances . . . . .	16
2.4 Surrogate Model . . . . .	16
2.4.1 Kriging Model [93] . . . . .	16
2.5 Surrogate Search . . . . .	18
2.5.1 Prediction based . . . . .	18
2.5.2 Expected Improvement . . . . .	18
2.5.3 WB2 and WB2S . . . . .	19

2.5.4	Constrained search - Probability of feasibility . . . . .	20
2.6	Optimization algorithm - Genetic Algorithm . . . . .	20
<b>3</b>	<b>Optimization Problem - Implementation</b>	<b>23</b>
3.1	Problem Formulation . . . . .	23
3.1.1	Mission Requirements . . . . .	23
3.1.2	Objective Function . . . . .	25
3.1.3	Design Variables and Parameterization . . . . .	26
3.1.4	Constraints . . . . .	27
3.1.5	Optimization Statement . . . . .	29
3.2	MDA Procedure . . . . .	29
3.2.1	Discipline Coupling . . . . .	29
3.2.2	Aerodynamic Loading estimation . . . . .	32
3.2.3	Structural Analysis . . . . .	32
3.2.4	CFD Analysis . . . . .	33
3.3	MDO methodology . . . . .	35
3.3.1	Surrogate models . . . . .	35
3.3.2	Search Algorithm . . . . .	36
3.3.3	Optimization Cycle . . . . .	43
<b>4</b>	<b>Post-Processing</b>	<b>45</b>
4.1	Discussion of Results . . . . .	45
4.2	Characterization and validation of final design . . . . .	51
4.2.1	Computational Validation . . . . .	56
<b>5</b>	<b>Conclusions</b>	<b>69</b>
5.1	Achievements . . . . .	69
5.2	Future Work . . . . .	70
	<b>Bibliography</b>	<b>73</b>
<b>A</b>	<b>Geometric parameterization</b>	<b>85</b>
A.1	Wing . . . . .	86
A.2	Winglet . . . . .	87
A.3	Canard . . . . .	88
A.4	Fin . . . . .	89
A.5	Fuselage . . . . .	90
A.6	Stacking of laminate layers . . . . .	91

# List of Tables

3.1	Aircraft requirements for forward flight. . . . .	24
3.2	Design variables plus correspondent lower and upper bounds. . . . .	28
3.3	Materials properties. . . . .	31
3.4	Cross-validation results for the Tsai-Wu and structural mass models, with a constant and a linear regression. . . . .	36
3.5	Test optimization results for each method, including an indication of convergence along with the number of iterations. . . . .	39
3.6	Test optimization results for WB2 and WB2S, including an indication of convergence along with the number of iterations. . . . .	41
4.1	Cross-validation results for the Tsai-Wu and structural mass models, with a constant and a linear regression. . . . .	46
4.2	Cross-validation results for the Tsai-Wu, structural mass and ( $L/D$ ) models, with a constant and a linear regression. . . . .	46
4.3	Values of the design variables for the final design. . . . .	52
4.4	Mode shapes and respective frequencies. . . . .	60



# List of Figures

1.1	Mission profile. . . . .	2
1.2	Reoccurrence rate of the different problem formulations and types of objectives for the analyzed case studies. . . . .	3
2.1	Wing approximated by a system of vortices. . . . .	10
2.2	Representation of the different angles in a local section of a three-dimensional wing. . . . .	10
2.3	Objectively ranked design points in multiobjective optimization. . . . .	14
2.4	Pareto frontier generation using the weighted sum method. . . . .	15
2.5	A $4 \times 4$ Latin square. . . . .	15
3.1	Wing representation. . . . .	27
3.2	Fuselage geometry. . . . .	28
3.3	MDA architecture. . . . .	30
3.4	Stacking sequence of the wingbox skin with the addition of new layers. . . . .	31
3.5	Outer mold line of an example configuration. . . . .	32
3.6	Structural model of an example configuration. . . . .	32
3.7	Deformed structure shape relative to undeformed shape. . . . .	33
3.8	Evaluation of Tsai-Wu failure criterion. . . . .	33
3.9	Mesh convergence test for the CFD analysis. . . . .	34
3.10	CFD mesh. . . . .	34
3.11	Representation of the Branin function. . . . .	37
3.12	Variation of the influence of the probability of feasibility with the variable $n$ . . . . .	38
3.13	Relevant properties of 'ga' function. . . . .	38
3.14	Fifth iteration prediction of sampling plan 12 with WB2+PF method. . . . .	40
3.15	Sixth iteration prediction of sampling plan 12 with WB2+PF method. . . . .	40
3.16	Eighteenth iteration prediction of sampling plan 2 with WB2 and WB2s methods. . . . .	41
3.17	Fiftieth iteration prediction of sampling plan 4 with WB2 method. . . . .	42
3.18	Optimization iteration cycle. . . . .	43
4.1	Evolution of $m_S$ along the optimization. . . . .	47
4.2	Evolution of $(L/D)$ along the optimization. . . . .	47
4.3	Evolution of the Tsai-Wu failure index along the optimization. . . . .	48

4.4	Evolution of the objective function along the optimization. . . . .	49
4.5	Evolution of range ratio, $R/R_{ref0}$ along the optimization. . . . .	49
4.6	Pareto frontier. . . . .	51
4.7	Representation of the structure of the final configuration. . . . .	52
4.8	Representation of the outer shape of the final configuration. . . . .	52
4.9	Aircraft dimensions. . . . .	53
4.10	Stream lines around the aircraft. . . . .	54
4.11	Pressure distribution on the surface and on the symmetry plane of the aircraft. . . . .	54
4.12	Tsai-Wu failure index values on entire structure. . . . .	55
4.13	Tsai-Wu failure index values on critical regions. . . . .	55
4.14	Distribution of the number of layers of wingbox skin along half span. . . . .	56
4.15	Distribution of the number of layers of wingbox spars along half span. . . . .	56
4.16	$C_L vs. \alpha$ curve for final configuration. . . . .	57
4.17	$C_D vs. \alpha$ curve for final configuration. . . . .	57
4.18	$C_m vs. \alpha$ curve for final configuration. . . . .	57
4.19	Drag polar for the final configuration. . . . .	58
4.20	$(L/D) vs. C_L$ curve for final configuration. . . . .	58
4.21	$C_D vs. \alpha$ curves the wing, canard and fuselage of the final configuration. . . . .	59
4.22	$C_L vs. \alpha$ curves for the two lifting surfaces of the final configuration. . . . .	59
4.23	Mode shape 1 general aircraft deformation and undeformed aircraft contours. . . . .	61
4.24	Mode shape 1 total deformation on critical region. . . . .	61
4.25	Mode shape 2 general aircraft deformation and undeformed aircraft contours. . . . .	61
4.26	Mode shape 2 total deformation on critical region. . . . .	62
4.27	Mode shape 3 general aircraft deformation and undeformed aircraft contours. . . . .	62
4.28	Mode shape 3 total deformation on critical region. . . . .	62
4.29	Mode shape 4 general aircraft deformation and undeformed aircraft contours. . . . .	62
4.30	Mode shape 4 total deformation on critical region. . . . .	63
4.31	Mode shape 5 general aircraft deformation and undeformed aircraft contours. . . . .	63
4.32	Mode shape 5 total deformation on critical region. . . . .	63
4.33	Mode shape 6 general aircraft deformation and undeformed aircraft contours. . . . .	64
4.34	Mode shape 6 total deformation on critical region. . . . .	64
4.35	Mode shape 7 general aircraft deformation and undeformed aircraft contours. . . . .	64
4.36	Mode shape 7 total deformation on critical region. . . . .	65
4.37	Mode shape 8 general aircraft deformation and undeformed aircraft contours. . . . .	65
4.38	Mode shape 8 total deformation on critical region. . . . .	65
4.39	Mode shape 9 general aircraft deformation and undeformed aircraft contours. . . . .	66
4.40	Mode shape 9 total deformation on critical region. . . . .	66
4.41	Mode shape 10 general aircraft deformation and undeformed aircraft contours. . . . .	66
4.42	Mode shape 10 total deformation on critical region. . . . .	67

A.1	Winglet position. . . . .	87
A.2	Canard tube section parameterization. . . . .	89
A.3	Geometry of fuselage spar. . . . .	90



# Nomenclature

## Greek symbols

$\alpha$	Angle of attack.
$\alpha_0$	Airfoil section zero lift angle.
$\alpha_{2D}$	Airfoil section flow angle.
$\alpha_i$	Airfoil section downwash induced flow angle.
$\alpha_{stall}$	Stall angle.
$\Gamma$	Circulation (vortex strength).
$\gamma$	Twist angle.
$\epsilon$	Kriging model error representing fluctuations around the trend.
$\eta$	Propeller efficiency.
$\kappa$	Thermal conductivity coefficient.
$\Lambda$	Sweep angle.
$\lambda$	Taper ratio.
$\mu$	Dynamic viscosity.
$\mu_m$	Kriging model mean response.
$\nu$	Poisson's ratio.
$\rho$	Density.
$\rho_c$	Carbon fiber composite density.
$\sigma^2$	Variance of the Gaussian distribution.
$\sigma_i$	Stress tensor components.
$\sigma_{x,y,z_{max}}$	Tensile strength in $x$ , $y$ and $z$ directions.
$\sigma_{x,y,z_{min}}$	Compressive strength in $x$ , $y$ and $z$ directions.

$\tau_{xy,yz,xzmax}$  Shear strength in  $xy$ ,  $yz$  and  $xz$  planes.

$\Phi$  Cumulative distribution function.

$\phi$  Probability density function.

$\Phi_d$  Dissipation function.

$\chi$  Feasible set of design points.

$\Psi$  Correlation matrix.

$\psi$  Correlations vector between observed data and new prediction.

$\omega$  Turbulent frequency.

### **Roman symbols**

$a_0$  Lift slope for two-dimensional section.

$adx_{afl}$  Non-dimensional chordwise coordinate of NACA 4-Digits airfoil.

$ady_{afl}$  Non-dimensional transverse coordinate of NACA 4-Digits airfoil for vertical surfaces.

$adz_{afl}$  Non-dimensional transverse coordinate of NACA 4-Digits airfoil for horizontal surfaces.

$AR$  Aspect ratio.

$b$  Span.

$BSFC$  Brake specific fuel consumption.

$c$  Chord.

$C_D$  Coefficient of drag.

$C_{D0}$  Zero lift drag coefficient.

$c_{disc}$  Chord at the position of discontinuity in the chord distribution.

$\bar{c}_f$  Fin mean aerodynamic chord.

$C_L$  Coefficient of lift.

$C_{L2D}$  Two-dimensional section lift coefficient.

$C_m$  Coefficient of moment.

$c_{root}$  Chord at the root.

$c_{tip}$  Chord at the tip.

$c_{trans}$  Chord at the wing-winglet transition.

$C_{VT}$  Vertical tail volume coefficient.

$cbr$	Airfoil maximum camber.
$D$	Drag.
$d_{fuse}$	Spanwise dimension of the fuselage.
$D_i$	Lift induced drag.
$E$	Elastic modulus.
$E[\cdot]$	Expected value.
$\bar{e}$	Average relative error.
$e_{max}$	Maximum relative error.
$F^a$	Applied load vector.
$F_{ij}$	Strength tensors.
$F^r$	Reaction load vector.
$f_S$	Search function.
$G$	Shear modulus.
$g$	Acceleration of gravity.
$h_{fuse}$	Height of the fuselage spar.
$h_n$	Nominal thickness of laminate composite layer .
$i$	Internal energy.
$I(\cdot)$	Improvement.
$i_c$	Incidence angle of canard.
$K$	Total stiffness matrix.
$k$	Turbulent kinetic energy.
$k_e$	Element stiffness matrix.
$K_n$	Static margin.
$k_{se}$	Squared exponential kernel function.
$L$	Lift.
$l_c$	Longitudinal distance between the aerodynamic centers of wing and canard.
$l_f$	Longitudinal distance between the aerodynamic center of the fin and the center of gravity.
$l_{fuse}$	Length of the fuselage spar.

$l_w$	Longitudinal distance between the aerodynamic center of the wing and the center of gravity.
$l_{xtr_{front}}$	Distance between the canard aerodynamic center and the front edge of the fuselage spar.
$m_f$	Final mass of the aircraft at the end of the mission segment.
$m_i$	Initial mass of the aircraft.
$m_S$	Structural mass of the aircraft.
$p$	Pressure.
$P[\cdot]$	Probability.
$p_c$	Canard airfoil maximum camber position.
$p_f$	Fin airfoil maximum camber position.
$p_w$	Wing airfoil maximum camber position.
$p_{wgl_t}$	Winglet airfoil maximum camber position.
$pos_{bot}$	Lower bound for the vertical position of the canard.
$pos_{fspar}$	Relative chordwise position of wing front spar.
$pos_{top}$	Upper bound for the vertical position of the canard.
$R$	Range.
$r$	Auxiliary distance in parameterization of wing-winglet transition.
$r_{tube}$	Canard tube radius.
$S$	Surface area.
$s^2$	Kriging model variance estimate.
$S_E$	Energy source.
$S_{Lc}$	Longitudinal compressive strength.
$S_{Lt}$	Longitudinal tensile strength.
$S_M$	Momentum source.
$S_S$	In-plane shear strength.
$S_{Tc}$	Transverse compressive strength.
$S_{Tt}$	Transverse tensile strength.
$T$	Temperature.
$t$	Maximum airfoil relative thickness.

$thk_{disc}$  Thickness at the position of discontinuity.

$thk_{fuse}$  Thickness of the fuselage spar.

$thk_{root}$  Thickness at the wing root.

$thk_{tip}$  Thickness at the wing tip.

$thk_{tube}$  Thickness of the canard tube.

**U** Velocity vector.

$u_n$  Nodal displacement vector.

$u, v, w$  Velocity Cartesian components.

$V_\infty$  Free-stream airspeed.

$V_{cr}$  Cruise speed.

$V_{stall}$  Stall speed.

**w** Vector of weights for multiobjective optimization.

$w_i$  Induced downwash velocity.

$x_{afl}$  Chordwise coordinate of NACA 4-Digits airfoil.

$x_{dim_i}$  Longitudinal dimension of original fuselage.

$x_l$  Chordwise coordinates of NACA 4-Digits airfoil lower surface.

$x_{rot}$  Chordwise position of the elastic axis of the wing.

$x_{scale}$  Longitudinal scaling factor of fuselage.

$x_{tube}$  Chordwise coordinates of canard tube section.

$x_u$  Chordwise coordinates of NACA 4-Digits airfoil upper surface.

$\mathcal{Y}$  Criterion space.

$y_{\gamma_{disc}}$  Spanwise position of wing twist distribution discontinuity.

$y_{afl}$  Transverse coordinate of NACA 4-Digits airfoil for vertical surfaces.

$y_{c_{disc}}$  Spanwise position of wing chord distribution discontinuity.

$y_{dim_i}$  Spanwise dimension of original fuselage.

$y_{scale}$  Spanwise scaling factor of fuselage.

$z_{afl}$  Transverse coordinate of NACA 4-Digits airfoil for horizontal surfaces.

$z_c$  Vertical distance between the aerodynamic centers of wing and canard.

$z_{cbr}$	Mean camber line.
$z_{dim_i}$	Transverse dimension of original fuselage.
$z_l$	Transverse coordinates of NACA 4-Digits airfoil lower surface.
$z_{scale}$	Transverse scaling factor of fuselage.
$z_t$	Thickness distribution of airfoil.
$z_{tube}$	Transverse coordinates of canard tube section.
$z_u$	Transverse coordinates of NACA 4-Digits airfoil upper surface.
$z_w$	Vertical distance between the aerodynamic center of wing and the center of gravity.

### Subscripts

$\alpha = 0$	Value for an angle of attack of zero degrees.
$c$	Property of the canard.
$f$	Property of the Fin.
$i, j, k$	Computational indexes.
$max$	Maximum value.
$min$	Minimum value.
$x, y, z$	Cartesian components.
$ref$	Reference condition.
$ref_0$	Initial reference condition.
$skin$	Property of the wingbox skin.
$spar$	Property of the wing spar.
$trim$	Trim condition.
$w$	Property of the wing.
$wgl$	Property of the winglet.

### Superscripts

$\hat{\phantom{x}}$	Prediction.
T	Transpose.

# Glossary

<b>AoA</b>	Angle of Attack
<b>CfAR</b>	Center for Aerospace Research
<b>CFD</b>	Computational Fluid Dynamics
<b>CFRP</b>	Carbon Fiber Reinforced Polymer
<b>CO</b>	Collaborative Optimization
<b>CoG</b>	Center of Gravity
<b>CSM</b>	Computational Structural Mechanics
<b>DRDC</b>	Defense Research and Development Canada
<b>EI</b>	Expected Improvement
<b>FEA</b>	Finite Element Analysis
<b>FEM</b>	Finite Element Method
<b>FVM</b>	Finite Volume Method
<b>GA</b>	Genetic Algorithm
<b>HF</b>	High Fidelity
<b>LF</b>	Low Fidelity
<b>LLT</b>	Lifting Line Theory
<b>MAC</b>	Mean Aerodynamic Chord
<b>MAD</b>	Magnetic Anomaly Detection
<b>MDA</b>	Multidisciplinary Design Analysis
<b>MDF</b>	Multidisciplinary Design Feasible
<b>MDO</b>	Multidisciplinary Design Optimization
<b>MF</b>	Multi-Fidelity
<b>MLE</b>	Maximum Likelihood Estimation
<b>MSE</b>	Mean Squared Error
<b>MTOM</b>	Maximum Take-off Mass
<b>NACA</b>	National Advisory Committee for Aeronautics
<b>OML</b>	Outer Mold Line
<b>PF</b>	Probability of Feasibility
<b>SFOC</b>	Special Flight Operations Certificate
<b>SI</b>	International System of Units

<b>SST</b>	Shear Stress Transport
<b>UAV</b>	Unmanned Aerial Vehicle
<b>UD</b>	Unidirectional
<b>VTOL</b>	Vertical Take-Off and Landing
<b>WB2</b>	Watson and Barnes search criterion

# Chapter 1

## Introduction

### 1.1 Motivation

In recent years, the importance of the development process and aircraft design have been increasing. This is due mainly to the emergence of more demanding requirements. As society evolves, manufacturers are pressured to produce aircraft that perform better, are more efficient and that are less harmful for the environment. Having a higher-level aircraft design tool will provide the manufacturers leverage over the competition.

Multidisciplinary design optimization (MDO) is a field of engineering that is a very useful tool of choice in the development of new aircraft or improvement of already existing designs. It makes use of numerical and analytic methods to develop models integrating multiple disciplines, such as aerodynamics, structures, stability, performance, among others. MDO aims to reach an optimal or near-optimal solution, which in the case of aerospace design, corresponds to a configuration that meets the requirements and extends the objectives of the mission it is proposed to accomplish.

This process can be very time demanding and computationally expensive when optimizing a whole aircraft, as it is a complex engineering design problem requiring simulations that can take multiple minutes, hours or even days to execute. One way to lighten the burden is to use surrogate models, which are approximation models that mimic the behavior of the simulation models as closely as possible, being cheaper to evaluate, thus achieving results faster and making use of less resources. This way, it is possible to reduce the computational and overall project cost of the whole optimization.

### 1.2 Project Overview/Conceptual Design Synthesis

This project focuses on a surrogate based multiobjective and multidisciplinary design optimization of an aircraft, involving both structural and aerodynamic variables. It is necessary to perform aerodynamic, as well as structural analyses to guarantee trimming and stability, in addition to the required strength and integrity of the structure, respectively. The mentioned aircraft is a vertical take-off and landing (VTOL) unmanned aerial vehicle (UAV) that is being developed by the University of Victoria Centre for

Aerospace Research (CfAR) in collaboration with Defense Research and Development Canada (DRDC), and it is meant to be used by the Canadian Air Force for magnetic detection of submarines to protect the Canadian borders. The aircraft will be equipped with a magnetic anomaly detection (MAD) sensor which will be used for the purpose. The aircraft mission, represented in figure 1.1, involves a vertical take-off and climb to minimum height segment followed by a transition to forward flight segment. The following segment is cruise at approximately 100m above sea level. After cruise, the mission is completed by a transition to axial flight and a vertical landing.

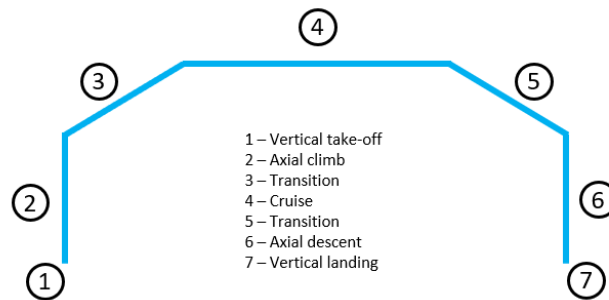


Figure 1.1: Mission profile.

The design of this UAV was started by Bruno Luís and some results and decisions from the conceptual and preliminary design done in his master thesis [1] that were preserved should be pointed out and are listed below:

- A fixed-wing canard configuration;
- Fuselage shape;
- Vertical tail volume coefficient ( $C_{VT}$ ) equal to 0.02 for directional stability.

### 1.3 State of the art

Methodology along with computer capacity to solve aircraft MDO problems are constantly evolving. This evolution is broadly verified by the differences between the most recent advancements back in 1997 [2] and those in 2018 [3].

There has been a continuous expansion of the research on MDO, namely on integration tools [4], more efficient optimization methods [5–7], partition architectures [8] as well as improved analysis capacity [9].

Regarding the formulation of optimization problems for aerial vehicles, the most used objectives are related with mission performance, weight, and aerodynamics, with the first two corresponding to approximately 46% and 39% of the case studies, respectively [3]. Although the vast majority is used in single objective problems, some cases consider a combination of multiple objectives, either by combining them in one single function or by solving a multiobjective problem [10–12]. The charts on figure 1.2 depict this trend.

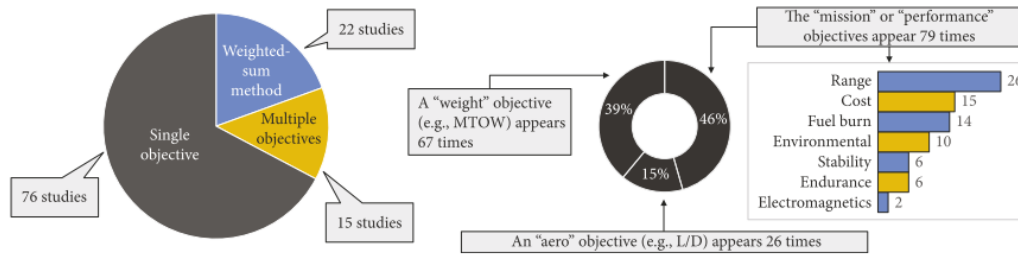


Figure 1.2: Reoccurrence rate of the different problem formulations (left) and types of objectives (right) for the analyzed case studies.[3]

On the other hand, constraints are usually case-dependent limit conditions [13, 14]. Other more general criteria can be included like mission requirements for general aviation [15–17], as well as safety regulations and performance minima that are required for certification [10, 15, 18–22].

The analysis of an aircraft configuration or component comprises various disciplines, making use of determined disciplinary models, which compose the framework of the optimization.

The disciplines with more models found in aircraft MDO are weight estimation, aerodynamics, structural behavior and propulsion. In a preliminary or conceptual stage of design, simpler models are considered: aerodynamic predictions are made using empirical equations [18, 21] or panel methods [23, 24], weight is also estimated by empirical equations [18, 25] or statistical data [26, 27], while propulsion can be assessed by statistical approximations [28, 29] as well as by the application of scaling factors to tables of already existing engine data [13, 30, 31]. Differently, in detailed design, a Computational Fluid Dynamics (CFD) analysis is preferred [32, 33] for the aerodynamic evaluation, weight is usually estimated from a simplified structural analysis [23, 28, 34–36] and, to increase fidelity, Computational Structural Mechanics (CSM) simulations [29, 32, 37, 38], as well as simulation models for the specific engine used [11, 19, 39–45] can be included.

Geometric models, trim and stability, and performance are also commonly used as support elements. The first is important to be robust enough to provide the desired detail, and also adaptable to cover the design space [30, 31, 45, 46]. Further, geometric models are frequently used to represent the aircraft in aerodynamic and structural analyses [29, 35, 39, 47–49]. Trim is achieved by allowing the control surfaces parameters to vary [16, 23, 38, 50–52] and stability is determined by calculating the stability derivatives and relating them with empirical equations [19, 27, 44, 53–55] or by using metrics, such as the static margin [25, 26, 56]. Mission performance can be evaluated if enough data concerning weight, aerodynamics and propulsion is gathered [13, 18, 21, 26, 31, 39, 40, 48, 57].

In addition, there are some supplementary models that are increasingly being included in the frameworks. These can include not only the flight dynamics and control [22, 23, 33, 58, 59], estimations of the emissions of harmful gases [26, 31, 43, 44, 60] or noise levels and propagation [32, 35, 45, 48, 60–63], but also cost models comprising production planning [26, 31, 44] or operating costs [10, 30, 64, 65], among others.

The accuracy required and the available resources determine the level of fidelity selected for the

Multidisciplinary Design Analysis (MDA), which is a compromise between the robustness and speed of the calculations and the precision in the representation of the problem. Frameworks that allow to alternate between different levels of fidelity are a regular practice [4, 10, 47, 48, 53, 66, 67].

Low Fidelity (LF) approximations are often employed in conceptual design as they provide satisfactory results at low computational costs [16, 26, 35, 47, 63, 64, 68]. However, for unusual configurations the physical phenomena may not be well replicated [20, 40, 58].

On the other hand, in a detailed design stage or for the assessment of unconventional concepts, a High Fidelity (HF) approach proves to be more adequate [34, 37, 45, 69]. Moreover, not as reoccurring as LF, HF can be exploited to increase reliability of a design [16, 37]. Although HF requires extended computational times due to the development of more complex models and higher computational demands [30, 58, 70–72], research is being conducted to implement HF from an early design stage to reduce uncertainty [30, 70, 73].

Additionally, medium fidelity tools provide a trade-off between LF and HF. It can consist on two possible approaches. One possibility is the refinement of LF simulations, such as Euler solvers [28, 69] or higher-order panel methods codes [39, 49] for aerodynamic analyses, and a more global CSM simulation for structural analyses. Alternatively, medium fidelity can be achieved by simplification of HF models, specifically, coarse CFD simulations [74] and the use of simplified geometries [29, 34] in aerodynamic and structural analyses, respectively.

Further, Multi-Fidelity (MF) can also be implemented to improve computational efficiency. LF is used for a faster exploration of the design space at an initial stage while HF is applied to the selected region of interest [7, 19, 75–77]. MF also proved to ease the transition from conceptual to detailed design [30, 78].

Other important aspect of MDO is the selection of a framework architecture to set the coupling, as well as to define partitions and solving sequence between the different disciplines. This topic has been thoroughly researched. Said research is condensed and explained in [8] for multiple architectures. The three most frequently used architectures are multidisciplinary design feasible (MDF), collaborative optimization (CO) and asymmetric approaches similar to CO but less partitioned [3].

Commonly used, MDF has a global optimizer controlling all design variables and constraints, providing consistent results at the end of each iteration. Although, a complete analysis cycle is required for every global evaluation, thus increasing the computational cost. Its implementation is simple and effective for the decomposition of coupled disciplines [13, 15, 25, 29, 30, 32, 33, 39–41, 53, 75, 78–83].

CO is a distributed architecture where each disciplinary subprocess corresponds to an optimization, allowing parallel analysis. This increases efficiency, however, a feasible solution is not always attained [3]. The partition is usually discipline-based as each individual model is analyzed and optimized independently [57, 84, 85].

Similarly to CO, in asymmetric approaches the problem is also decomposed into local optimization processes that run independently for each global evaluation, considering a set of local design variables, constraints and objectives. Conversely, a global optimizer at a higher level controls a reduced number of global variables. Considering local processes reduces complexity at higher levels [10, 29, 37, 50, 61, 66, 86–88]

Surrogate models are often used to increase the efficiency of the optimization by replacing HF simulations with approximation models that mimic the behavior of the system. Although its use allows to reduce the optimization time, the existence of large deviations from the real models is a possible disadvantage.

These models are mostly employed to replace CFD simulations [12, 17, 25, 35, 37, 81, 84, 89–91] and CSM codes [17, 28, 30, 41, 81, 84, 90] but can also be utilized in other applications like aircraft dynamics, noise propagation, mission specifications and engine performance [10, 11, 28, 35, 39, 41, 42, 56, 70, 92].

Probabilistic surrogate models like Kriging [93] are frequently used in numerous case studies [13, 17, 28, 35, 42, 70, 72, 75–77, 81, 84, 89, 90, 92, 94, 95]. Kriging based model adaptations are also being considered more recently [6, 96]. Methods to improve the implementation of surrogates are being developed, aiming to efficiently update existing models with new samples [6, 10, 35, 37, 42, 56, 70, 72, 90, 91, 96]. For this purpose, selection criteria, such as the Expected Improvement (EI) [97], are being used to search the models directly [72, 90, 94, 95], or combined to create more balanced criteria [6, 96]. An alternative approach is to apply the surrogates to specific important regions of the design space, increasing the accuracy of the approximations [35, 39, 91].

As MDO usually considers approximations and simplifications, a validation is fundamental to confirm the obtained results and make sure they are reliable. This is of additional relevance for surrogate based optimization. Validation is mostly performed by one of three methods, being these, HF simulations [16, 23, 25, 34, 35, 37, 40, 48, 49, 59, 75, 98, 99], using existing data from similar aircraft [11, 15, 19, 39, 64, 71, 82, 84, 88, 98] and building physical scale and subscale prototypes for experimental testing [24, 34, 45, 55, 69, 74, 83, 100, 101].

## 1.4 Objectives

The ultimate goal of this thesis is to obtain an optimal, or near-optimal design for the whole aircraft from a surrogate-based MDO. This broad target can be divided in the following substeps:

1. Define the optimization problem, namely, the objective, constraints and the design variables;
2. Develop and implement the parametric geometric model of the aircraft based on the chosen design variables;
3. Build the computational models for the HF structural and aerodynamic analysis;
4. Assemble a database with the results of the structural and aerodynamic analysis on multiple design points;
5. Create a surrogate approximation model from the database mentioned in the previous point;
6. Retrieve optimized design configurations from the surrogate optimization;
7. Select, validate and describe the achieved optimal design for the UAV.

## 1.5 Thesis Outline

Additionally, there are four more chapters in this report. Below follows a summarized description of each one of them.

### **Chapter 2: Theoretical Background**

In this chapter, a brief description of the theoretical models implemented throughout this thesis, as well as some concepts and definitions are presented to provide the reader with the background knowledge necessary to follow the discussion of the whole process.

### **Chapter 3: Optimization problem - Implementation**

The third chapter describes the whole process of the optimization. Starting with the formulation of the problem, including the definition of the objective function, together with the selection of the appropriate design variables and constraints, according with the provided requirements.

A detailed characterization of the analysis architecture, and of the way each UAV configuration is evaluated is also included.

Additionally, the reasoning behind the employed surrogate models and search methods is explained and discussed.

### **Chapter 4: Post-Processing**

This chapter depicts the acquired results along the optimization, as well as a detailed examination of its evolution.

Further, a description and more complete characterization and validation of the final achieved design are presented.

### **Chapter 5: Conclusions**

The last chapter overviews the achievements made throughout this project, regarding the established objectives. Some observations about the optimization are also provided, including advantages and detected setbacks. Finally, the next steps in the design of the aircraft are listed, together with suggestions for future work.

## Chapter 2

# Theoretical Background

### 2.1 Multidisciplinary Analysis

The MDO of an aircraft requires solving problems to obtain values for physical quantities spanning across multiple disciplines. For the specific optimization addressed in this thesis, the analysis involves two major disciplines, such as, structures and aerodynamics. The two disciplines are coupled as the structural analysis uses the aerodynamic loading previously obtained from the aerodynamic analysis.

#### 2.1.1 Structural Analysis

Regarding the structures, a Finite Element Analysis (FEA) is performed making use of the ANSYS Mechanical APDL software [102]. The structural integrity of the UAV is evaluated by implementing the Tsai-Wu failure criterion to check if there is structural failure due to exceeding stress limits.

The theory behind the used Finite Element Method (FEM) plus the employed failure criterion in the context of composite materials is explained in subsections 2.1.1.1 and 2.1.1.2.

##### 2.1.1.1 FEM - ANSYS Mechanical APDL

The FEM is an approximate method used to solve and find a solution to the structural governing equations, that otherwise would be expensive or impossible to obtain from analytic methods.

The whole domain is represented by a collection of simple subdomains called elements, forming a mesh. At each element the physical process in study is approximated by functions of the desired type (usually polynomials) and algebraic equations that relate the values of the solution at a finite number of preselected points designated element nodes. Finally, the element equations are assembled by imposing interelement continuity of the solution as well as balance of interelement forces or other physical quantities.[103]

The desired simulation is represented by a static analysis in ANSYS Mechanical APDL [102]. It is valid for all degrees of freedom. Further, it does not take into account inertial and damping effects except static acceleration fields. [104]

The overall equilibrium equation that represents the mechanical behavior of the approximated structure is given by:

$$[K]\{u_n\} = \{F\} \Leftrightarrow [K]\{u_n\} = \{F^a\} + \{F^r\}, \quad (2.1)$$

where,  $[K]$  = total stiffness matrix =  $\sum_{m=1}^N [k_e]$ ,  $N$  is the number of elements,  $[k_e]$  is the element stiffness matrix,  $\{u_n\}$  is the nodal displacement vector,  $\{F^r\}$  is the reaction load vector and  $\{F^a\}$  is the applied load vector, which can account for applied nodal loads, acceleration loads, thermal loads, as well as pressure loads.

The stiffness matrix is calculated from the material properties together with the geometric dimensions. Knowing the element stiffness matrix, that is, the "force-displacement" relationship for each structural element, the "force-displacement" relationship for the complete structure is assembled using standard matrix methods. [104]

### 2.1.1.2 Tsai-Wu failure criterion

Composites are anisotropic materials, which means that the properties depend on the material directions. Thus, failure criteria for these materials are more complex than those used for isotropic materials as they need to consider strength in all independent directions.

Laminate composites are classified as orthotropic materials, thus having properties that are different in three mutually orthogonal directions [105]. Considering a single ply of a laminate, there are five independent strength constants that correspond to maximum allowed in-plane stresses in the principal axes. They are defined as follows:

- $S_{Lt}$  - Longitudinal tensile strength
- $S_{Lc}$  - Longitudinal compressive strength
- $S_{Tt}$  - Transverse tensile strength
- $S_{Tc}$  - Transverse compressive strength
- $S_S$  - In-plane shear strength

Tsai and Wu suggested a quadratic criterion for a six-dimensional stress space, in which failure occurs if the following is verified:

$$F_i \sigma_i + F_{ij} \sigma_i \sigma_j = 1 \quad i, j = 1, \dots, 6, \quad (2.2)$$

wherein  $\sigma_{1,2,3}$  are the direct stresses in each of the principal directions, the remaining stress components are  $\sigma_4 = \tau_{23}$ ,  $\sigma_5 = \tau_{31}$ ,  $\sigma_6 = \tau_{12}$  and  $F_i$  and  $F_{ij}$  are strength tensors [106].

For a single orthotropic ply of a laminate, subject to plane stress, equation 2.2 is simplified to [106]:

$$F_1 \sigma_{11} + F_2 \sigma_{22} + F_6 \tau_{12} + F_{11} \sigma_{11}^2 + F_{22} \sigma_{22}^2 + F_{66} \tau_{12}^2 + 2F_{12} \sigma_{11} \sigma_{22} = 1, \quad (2.3)$$

where the strength coefficients can be determined by the following expressions:

$$\begin{aligned}
F_1 &= \frac{1}{S_{Lt}} - \frac{1}{S_{Lc}}; \\
F_2 &= \frac{1}{S_{Tt}} - \frac{1}{S_{Tc}}; \\
F_6 &= 0; \\
F_{11} &= \frac{1}{S_{Lt}S_{Lc}}; \\
F_{22} &= \frac{1}{S_{Tt}S_{Tc}}; \\
F_{66} &= \frac{1}{S_S^2}.
\end{aligned} \tag{2.4}$$

However, the in-plane interaction term  $F_{12}$  must be discovered by a bi-axial tensile test. In such test, the shear stress  $\tau_{12}$  is null and the stress state will correspond to an equal tensile stress in both principal directions,  $\sigma_{11} = \sigma_{22} = \sigma$ . Then, by replacing the known stresses and coefficients in equation 2.3,  $F_{12}$  can be calculated by [105]:

$$F_{12} = \frac{1}{2\sigma^2} \left[ 1 - \left( \frac{1}{S_{Lt}} - \frac{1}{S_{Lc}} + \frac{1}{S_{Tt}} - \frac{1}{S_{Tc}} \right) \sigma - \left( \frac{1}{S_{Lt}S_{Lc}} + \frac{1}{S_{Tt}S_{Tc}} \right) \sigma^2 \right]. \tag{2.5}$$

Nevertheless, it is possible to estimate  $F_{12}$  with the relation [105]:

$$-\frac{1}{2}(F_{11}F_{22})^{1/2} \leq F_{12} \leq 0. \tag{2.6}$$

Unlike other simpler criteria, one advantage of the Tsai-Wu failure criterion is that it takes into account the interaction between different stress components. Moreover, it has a good compatibility with experimental data[105][107][108].

## 2.1.2 Aerodynamic Analysis

There are two separate stages of the aerodynamic analysis. A LF calculation of the aerodynamic loads based on Prandtl's Lifting Line Theory (LLT) and also a HF CFD analysis performed with ANSYS CFX [109].

A brief theoretical insight on both Prandtl's LLT and CFD simulation is presented on subsections 2.1.2.1 and 2.1.2.2, respectively.

### 2.1.2.1 Prandtl's Lifting Line Theory [110]

Prandtl's LLT is used to demonstrate the aerodynamic behavior of straight three-dimensional wings. Although it considers wing twist as well as varying chord and airfoil along span, it does not take into account dihedral or sweep on the wing. This theory assumes inviscid incompressible flow and it can be considered a good approximation for wings with an aspect ratio  $AR \geq 4$ .

By observation of real wings, it is known that finite wings induce circulation extending from tip to tip. Moreover, a vortex that extends far into the flow field behind the wing is shed from each wingtip. This behavior can be approximated by replacing the wing with multiple horseshoe vortices with different but constant strengths. Each vortex is formed by a bound vortex in the spanwise direction, plus two trailing vortices, one on each side, that extend to infinity behind the wing. The representation of said approximation is shown in figure 2.1.

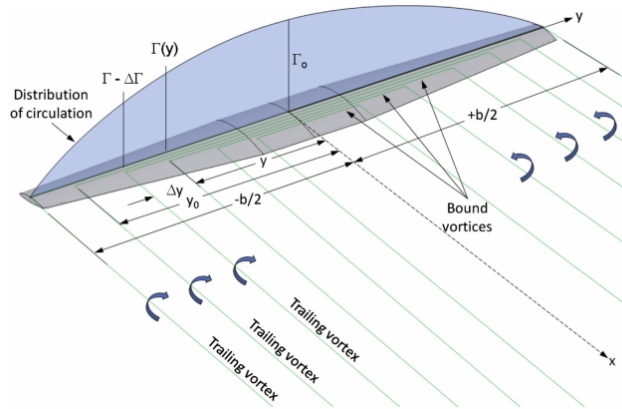


Figure 2.1: Wing approximated by a system of vortices [110].

This allows for a distribution of circulation  $\Gamma(y)$  along span, where  $y$  corresponds to a specific spanwise station, which is transformed into angular form to simplify posterior calculations:

$$y = \frac{b}{2} \cos(\theta), \quad \theta \in [0, \pi], \quad (2.7)$$

where  $b$  is the wingspan.

The spanwise distribution of vortex strengths is represented by a Fourier sine series of  $N$  elements:

$$\Gamma(\theta) = 2bV_\infty \sum_{n=1}^N A_n \sin(n\theta), \quad (2.8)$$

where,  $V_\infty$  denotes the free-stream airspeed and  $A_n$  are the coefficients of the Fourier series that will be determined and used for the aerodynamic characterization of the lifting surface.

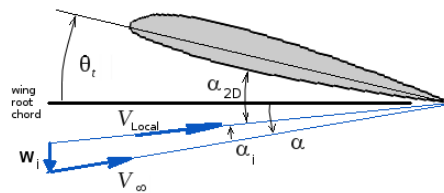


Figure 2.2: Representation of the different angles in a local section of a three-dimensional wing [111].

The trailing vortex sheet induces a downwash on the wing displayed on figure 2.2 for each spanwise

section. The velocity of the induced downwash  $w_i$  is given by:

$$w_i = V_\infty \frac{\sum_{n=1}^N A_n \sin(n\theta)}{\sin\theta}. \quad (2.9)$$

Also from figure 2.2, the downwash angle is then:

$$\alpha_i = \frac{w_i}{V_\infty}. \quad (2.10)$$

It verifies that the local flow angle at each section is equal to the sum of the three-dimensional wing's angle of attack ( $\alpha$ ), plus the section twist ( $\gamma$ ) minus the downwash angle [111]:

$$\alpha_{2D} = \alpha - \alpha_i + \gamma. \quad (2.11)$$

Knowing that the two-dimensional section lift coefficient is a function of the local flow and the bound vortex strength at this span location, it is possible to rearrange the relation expression:

$$\begin{aligned} C_{L_{2D}} &= a_0(\alpha_{2D} - \alpha_0) = \frac{2\Gamma}{V_\infty c} \\ \Leftrightarrow \Gamma &= \frac{1}{2} a_0 V_\infty c (\alpha - \alpha_i + \gamma - \alpha_0), \end{aligned} \quad (2.12)$$

where,  $a_0$ ,  $c$  and  $\alpha_0$  are the lift slope, the chord and the zero lift angle for the considered section, respectively.

Equations 2.8 and 2.12 can be combined to form the monoplane equation. Considering the simplification  $\mu = \frac{a_0 c}{4b}$ , the latest is given by:

$$\sum_{n=1}^N (A_n \sin(n\theta)(\sin\theta + n\mu)) = \mu(\alpha + \gamma - \alpha_0) \sin\theta. \quad (2.13)$$

In order to solve for the coefficients  $A_n$ , the previous equation is applied for all  $N$  spanwise stations and then used to build the aerodynamic influence matrix:

$$\begin{aligned} \begin{bmatrix} \sin\theta_1(\sin\theta_1 + \mu) & \sin(2\theta_1)(\sin\theta_1 + 2\mu) & \cdots & \sin(N\theta_1)(\sin\theta_1 + N\mu) \\ \sin\theta_2(\sin\theta_2 + \mu) & \sin(2\theta_2)(\sin\theta_2 + 2\mu) & \cdots & \sin(N\theta_2)(\sin\theta_2 + N\mu) \\ \vdots & \vdots & \ddots & \vdots \\ \sin\theta_N(\sin\theta_N + \mu) & \sin(2\theta_N)(\sin\theta_N + 2\mu) & \cdots & \sin(N\theta_N)(\sin\theta_N + N\mu) \end{bmatrix} \begin{Bmatrix} A_1 \\ A_2 \\ \vdots \\ A_N \end{Bmatrix} = \\ = \begin{Bmatrix} \mu(\alpha + \gamma_1 - \alpha_{0_1}) \sin\theta_1 \\ \mu(\alpha + \gamma_2 - \alpha_{0_2}) \sin\theta_2 \\ \vdots \\ \mu(\alpha + \gamma_N - \alpha_{0_N}) \sin\theta_N \end{Bmatrix}. \end{aligned} \quad (2.14)$$

Subsequently, with all the  $A_n$  coefficients calculated, the lift, and accordingly the lift induced drag, are obtained from the following expressions, respectively:

$$L = \rho V_\infty \int_{-\frac{b}{2}}^{\frac{b}{2}} \Gamma(y) dy , \quad (2.15)$$

$$D_i = -\rho \int_{-\frac{b}{2}}^{\frac{b}{2}} w_i(y) \Gamma(y) dy \Rightarrow D_i = \frac{\rho V_\infty^2}{2} b^2 \pi \sum n A_n^2 . \quad (2.16)$$

### 2.1.2.2 CFD - ANSYS CFX

ANSYS CFX [109] uses element based finite volume method (FVM). This method consists on a discretization of the spatial domain in non-overlapping elements or finite volumes forming a three-dimensional mesh. These volumes preserve information about determined quantities like mass, momentum and energy.

Following, there is the integration of the differential equations over each element to generate algebraic equations that are then solved to determine the solution.

In FVM, the flux entering a given volume is identical to that leaving the adjacent volume, making it a rigorously conservative method [112].

The governing differential equations in ANSYS CFX [109] are the unsteady Navier-Stokes equations. These are composed by the five equations, 2.17, 2.18, 2.19, 2.20 and 2.21, which respectively represent the conservation of mass, momentum in the three directions and energy [113]:

$$\frac{\partial \rho}{\partial t} + \nabla \cdot (\rho \mathbf{U}) = 0 , \quad (2.17)$$

$$\rho \frac{Du}{Dt} = -\frac{\partial p}{\partial x} + \nabla \cdot (\mu \nabla u) + S_{M_x} , \quad (2.18)$$

$$\rho \frac{Dv}{Dt} = -\frac{\partial p}{\partial y} + \nabla \cdot (\mu \nabla v) + S_{M_y} , \quad (2.19)$$

$$\rho \frac{Dw}{Dt} = -\frac{\partial p}{\partial z} + \nabla \cdot (\mu \nabla w) + S_{M_z} , \quad (2.20)$$

$$\rho \frac{Di}{Dt} = -p \nabla \cdot \mathbf{U} + \nabla \cdot (\kappa \nabla T) + \Phi_d + S_i . \quad (2.21)$$

where,  $\mathbf{U} = \{u, v, w\}$  represents the velocity vector,  $p$  is the pressure,  $\rho$  is the air density,  $\mu$  is the dynamic viscosity,  $S_M$  is the momentum source,  $i$  is the internal energy,  $\kappa$  is the thermal conductivity,  $T$  is temperature,  $S_i = S_E - \mathbf{U} \cdot S_M$ , with  $S_E$  being the energy source and finally,  $\Phi_d$  is the dissipation function that considers the effects due to viscous stresses.

This set of equations, together with a turbulence model, can model accurately both laminar and turbulent flows without additional information. Nonetheless, to be solved directly, turbulent flows usually require a computing power many orders of magnitude higher than available today [114]. Thus, it is necessary to apply turbulence models to predict the effects of turbulence.

The implemented model is the Shear Stress Transport (SST). This is a two-equation model based on  $k$ - $\omega$ , that uses two transport equations, one for the turbulent kinetic energy,  $k$ , and other for the turbulent frequency,  $\omega$ , assuming that the turbulence viscosity is linked to the turbulent kinetic energy and turbulent frequency [114]. The difference is that SST also accounts for the transport of the turbulent shear stress, giving highly accurate predictions of the onset and the amount of flow separation under adverse pressure gradients [114].

## 2.2 Optimization Problem

### 2.2.1 Basic concepts and problem formulation

Before proceeding with a more detailed description of optimization methods and algorithms, it is important to clarify concepts and introduce definitions that are used throughout this thesis.

The first major step in optimization is to define the optimization problem itself, starting with the selection of what to optimize. According to the requirements and desired goals, an objective function  $f$  is defined. The objective function is a quantitative measure of how good a design is, thus allowing to compare two designs.

Each design is defined by a set of parameters on which  $f$  depends on. The parameters that are allowed to vary in the design process are designated design variables. A  $k$ -dimensional vector of values corresponding to  $k$  different design variables is called a design point ( $x$ ). The combination of the domain for each design variable forms the design space.

Most complex engineering optimization problems have design limitations. In aircraft design, these may correspond to weight restrictions or performance minima, for example. Each limitation is specified by a constraint. Constraints can be applied either to design variables, in which case are considered bounds, or to dependent outcomes, such as having a specified maximum lift coefficient. Constraints may also be divided in equalities and inequalities, depending on if they are written with = or if they are defined with  $<$ ,  $>$ ,  $\leq$  or  $\geq$ , respectively.

Thus, it is possible to state the optimization problem as [97]:

$$\begin{aligned}
 & \text{minimize} && f(x) \\
 & \text{w.r.t} && x \in \chi \\
 & \text{subject to} && h_p = 0, \quad p = 1, 2, \dots, N_h \\
 & && g_m \geq 0, \quad m = 1, 2, \dots, N_g
 \end{aligned} \tag{2.22}$$

where  $h$  is the vector of equality constraints,  $g$  is the vector of inequality constraints, that includes the bounds on design variables, and  $\chi$  is the feasible set of design points corresponding to the region of the domain in  $\mathbb{R}^k$  where all constraints are satisfied.

Additionally, the notation  $\mathcal{Y}$  is used when referring to the criterion space, which is the image of  $\chi$  through  $f$ .

## 2.2.2 Multiobjective Optimization-Pareto frontier and Weighted sum method [97]

In complex aerospace design problems is often advantageous to make an optimization with multiple objectives simultaneously to reach a balanced and overall optimal solution. Multiple objectives imply the existence of multiple optima. It is then essential to prioritize the existing objectives in order to select the most adequate solution. A Pareto frontier is a useful tool for decision-making regarding trade-offs between objectives. Before presenting the definition of a Pareto frontier it is necessary to point out the concept of Pareto optimality. A design point ( $x$ ) is considered Pareto optimal if it does not exist an  $x' \in \chi$  such that  $x'$  dominates  $x$ . Having this, it is also fundamental to clarify the meaning of dominance in the previous definition. In multiobjective optimization,  $x$  dominates  $x'$  if and only if

$$f_i(x) \leq f_i(x') \text{ for all } i \text{ in } \{1, \dots, m\} \quad (2.23)$$

and  $f_i(x) < f_i(x')$  for some  $i$ ,

where,  $m$  is the number of different objectives and  $\mathbf{f} = \{f_1, \dots, f_m\}$  is the objective function that returns a  $m$ -dimensional vector of values  $\mathbf{y}$ , in which each dimension corresponds to one objective. In other words, a point is Pareto optimal if it is impossible to improve one objective without making, at least, one other objective worse. Such relation is illustrated in figure 2.3.

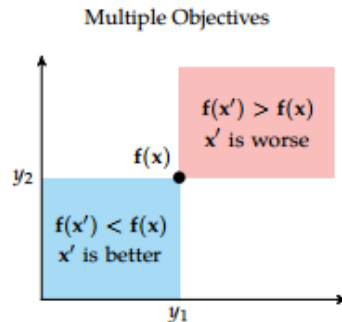


Figure 2.3: Objectively ranked design points in multiobjective optimization [97].

A Pareto frontier is defined as the set of Pareto-optimal points in the criterion space. There are some methods to generate a Pareto frontier, one of them being the Weighted sum method. This method makes use of a vector of weights  $\mathbf{w}$  to define priorities between objectives. The weight vector transforms the multiobjective functions  $\mathbf{f}$  into a combined single objective  $f$ :

$$f(x) = \mathbf{w}^T \mathbf{f}(x), \quad (2.24)$$

where the elements of  $\mathbf{w}$  are non-negative and sum to one when non-dimensionalized, and each one is associated with a different objective. If the selection of weights is not evident, the space of weights can be swept to generate the Pareto frontier. In a two-dimensional space,  $w_1$  varies from 0 to 1, while  $w_2$  is parameterized as  $w_2 = 1 - w_1$ . This procedure is shown in figure 2.4.

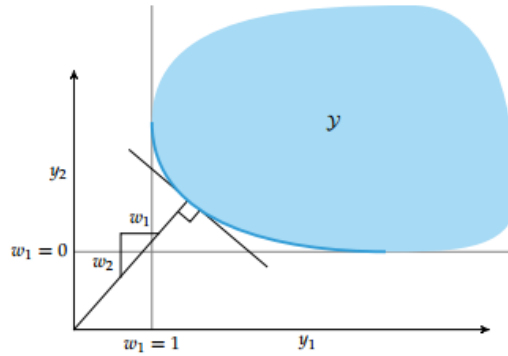


Figure 2.4: Pareto frontier generation using the weighted sum method [97].

## 2.3 Sampling Plan

Surrogate optimization is a good option for problems where the function evaluations are expensive. An initial set of points is required to generate these surrogate models. Furthermore, the points should be uniformly spread (space-filling), in order to achieve an uniform level of accuracy, as the approximations are more accurate closer to points where the objective function was evaluated.

There are multiple methods to select an initial set of points that cover the region as well as possible, one of which is the Latin-Hypercube Sampling and it is described in the subsection below.

### 2.3.1 Latin-Hypercube Sampling

Latin-Hypercube sampling is an uniform projection plan, that is, it has an uniform distribution of points over each dimension, meaning that projections on the axis of each dimension do not overlap [93].

A Latin-Hypercube is built by gridding the design space and splitting it in equal sized boxes. Points are then placed in these boxes, in such way that, when projected parallel with any of the axis, the points will not coincide. This is a generalization of a Latin square to any number of dimensions. A Latin square is a  $n \times n$  grid filled with  $n$  different numbers, where each row and each column has exactly one of each numbers [115] (figure 2.5). For a  $n \times n$  grid, the distribution of  $n$  points can be done with a permutation of  $n$  elements. Therefore, Latin-Hypercube samples can be obtained using a permutation in each dimension.

4	1	3	2
1	4	2	3
3	2	1	4
2	3	4	1

Figure 2.5: A  $4 \times 4$  Latin square constructed from the distribution of values  $\{1, 2, 3, 4\}$ [97].

### 2.3.2 Space-filling metrics - Pairwise Distances

Not all uniform projection plans provide a good cover of the search space (for example a sampling plan that covers the grid diagonal in a two-dimensional design space). Therefore, it is important to choose a good sampling plan that fills the design space, considering that the bigger the distance from the samples, the smaller is the ability of the model to generalize the response.

The best approach is to generate multiple sets of samples and choose the best. The selection is done based on a comparison criterion. The criterion used throughout this project is the pairwise distances [97].

First, all distances between any two points ( $\mathbf{x}$  and  $\mathbf{x}'$ ) of a sampling plan are calculated and all the different ones are stored in a vector in ascending order. To do this, the normalized distance, using the Euclidean norm [93] was used:

$$d(\mathbf{x}, \mathbf{x}') = \sqrt{\frac{\sum_{i=1}^k \left( \frac{x_i - x'_i}{x_{i_{max}} - x_{i_{min}}} \right)^2}{k}}, \quad (2.25)$$

where  $k$  is the number of dimensions and  $x_{i_{max}}$  and  $x_{i_{min}}$  are the maximum and minimum values of the  $i^{th}$  dimension of  $\mathbf{x}$ .

This is done for all the sampling plans. Afterwards, the vectors of each set are compared element by element. The one with the first pairwise distance that exceeds the other is chosen as it is considered more space-filling [97].

## 2.4 Surrogate Model

The model chosen for this project is the Kriging model, which will be briefly described bellow. First off, the sample points at which the real function was evaluated are denoted as  $\mathbf{x}^{(i)}$  ( $i = 1, \dots, n$ ), where  $n$  is the number of samples. Moreover, the function evaluations at these points are  $\mathbf{y} = [y^{(1)}, \dots, y^{(n)}]$

### 2.4.1 Kriging Model [93]

First developed and named after the mining engineer Danie Krige in [116], formalized by Matheron [117] and later introduced in engineering [118, 119], the Kriging model is used to estimate the response of a function at an unsampled location.

Assuming that the deterministic value of  $y(\mathbf{x})$  results from a combination of a deterministic plus a stochastic processes  $Y(\mathbf{x})$ , it can be represented by:

$$Y(\mathbf{x}) = \mu_m + \epsilon(\mathbf{x}), \quad (2.26)$$

where  $\mu_m$  is the mean of the response at a sampled design point and  $\epsilon(\mathbf{x})$  is the error that represents the fluctuations around the trend. The latest has zero expected value ( $E[\epsilon(\mathbf{x})] = 0$ ), arising out of a stationary Gauss process. The correlation between fluctuations depends only on the distance between

the considered locations. Having this, the correlation between two points in  $\chi$ ,  $\mathbf{x}$  and  $\mathbf{x}'$ , is given by the following common kernel (squared exponential kernel) function  $k_{se}(\mathbf{x}, \mathbf{x}')$ :

$$\text{cor}[Y(\mathbf{x}), Y(\mathbf{x}')] = k_{se}(\mathbf{x}, \mathbf{x}') = \exp\left(\sum_{j=1}^m \theta_j (x_j - x'_j)^2\right), \quad (2.27)$$

where  $m$  is the number of design variables. The covariance function is then expressed as

$$\text{Cov}[Y(\mathbf{x}), Y(\mathbf{x}')] = \sigma^2 \text{cor}[Y(\mathbf{x}), Y(\mathbf{x}')], \quad (2.28)$$

where  $\sigma^2$  is the variance of the Gaussian distribution. Accordingly, the correlation matrix for the observed data  $\Psi$  is defined as:

$$\Psi = \begin{pmatrix} \text{cor}[Y(\mathbf{x}^{(1)}), Y(\mathbf{x}^{(1)})] & \cdots & \text{cor}[Y(\mathbf{x}^{(1)}), Y(\mathbf{x}^{(n)})] \\ \vdots & \ddots & \vdots \\ \text{cor}[Y(\mathbf{x}^{(n)}), Y(\mathbf{x}^{(1)})] & \cdots & \text{cor}[Y(\mathbf{x}^{(n)}), Y(\mathbf{x}^{(n)})] \end{pmatrix}. \quad (2.29)$$

Additionally, the covariance matrix is then

$$\text{Cov}(\mathbf{Y}, \mathbf{Y}) = \sigma^2 \Psi. \quad (2.30)$$

It is necessary to choose the adequate parameters  $\theta$  in order to build a more accurate approximation model, as they affect the influence of each design variable on the function to be approximated. This selection is based on the maximum likelihood estimation (MLE) method.

The likelihood of a model measures the probability of the initial data set having resulted from the model, given the parameters set. This method maximizes the likelihood with the goal of reaching the most appropriate  $\theta$  parameters. As follows, the maximum likelihood estimates for  $\mu_m$  and  $\sigma^2$  are:

$$\hat{\mu}_m = \frac{\mathbf{1}^\top \Psi^{-1} \mathbf{y}}{\mathbf{1}^\top \Psi^{-1} \mathbf{1}}, \quad (2.31)$$

$$\hat{\sigma}^2 = \frac{(\mathbf{y} - \mathbf{1}\hat{\mu}_m)^\top \Psi^{-1} (\mathbf{y} - \mathbf{1}\hat{\mu}_m)}{n}, \quad (2.32)$$

where,  $\mathbf{1}$  is a  $n \times 1$  column vector of ones.

The prediction of the true function  $y(\mathbf{x})$  at an unsampled point should also be consistent with the data, as well as with  $\theta$ . Thus, the prediction  $\hat{y}(\mathbf{x})$  will be such that maximizes the likelihood of the sample data plus the prediction, given the hyperparameters, resulting in the following expression for the prediction:

$$\hat{y}(\mathbf{x}) = \hat{\mu}_m + \psi^\top \Psi^{-1} (\mathbf{y} - \mathbf{1}\hat{\mu}_m), \quad (2.33)$$

where  $\psi$  is the correlations vector between observed data and the new prediction, defined as:

$$\boldsymbol{\psi} = \begin{pmatrix} \text{cor}[Y(\mathbf{x}^{(1)}), Y(\mathbf{x})] \\ \vdots \\ \text{cor}[Y(\mathbf{x}^{(n)}), Y(\mathbf{x})] \end{pmatrix}. \quad (2.34)$$

In addition, it is also possible to calculate an estimate of the variance of the prediction:

$$\hat{s}^2(\mathbf{x}) = \sigma^2 \left[ 1 - \boldsymbol{\psi}^\top \boldsymbol{\Psi}^{-1} \boldsymbol{\psi} + \frac{1 - \mathbf{1}^\top \boldsymbol{\Psi}^{-1} \boldsymbol{\psi}}{\mathbf{1}^\top \boldsymbol{\Psi}^{-1} \mathbf{1}} \right]. \quad (2.35)$$

## 2.5 Surrogate Search

After defining the initial surrogate model, it is important to know how to evolve and improve the surrogate aiming to find a global optimum. There are various infill criteria to select a new design point to be evaluated in order to update the model and search for a minimum. The following criteria were used and tested for this project and a short description will be presented.

### 2.5.1 Prediction based

Prediction based exploitation is a local optimization technique that consists on minimizing the surrogate function. Thus, the region around the predicted optimum is exploited, resulting in new update points near the previous. Although it is an efficient optimizer with fast convergence, if the initial model is not a good approximation of the real function and the surrogate has long steep valleys, the optimization might get stuck on local minima, which will require the restart of the search from a different starting point hoping for it to be in a better region, closer to the global optimum [93].

In these situations of poor initial surrogates it is suitable to start searching away from the current minimum, making use of more global criteria.

### 2.5.2 Expected Improvement

Opposite from the previous method, there is the Expected Improvement (EI) exploration. It is a more global search criteria that focuses the exploration on maximizing the expected improvement over the current best function evaluation,  $y_{min}$ .

Improvement for a function sampled at  $\mathbf{x}$  producing  $y = f(\mathbf{x})$  is defined as [97]:

$$I(y) = \begin{cases} y_{min} - y, & \text{if } y < y_{min} \\ 0, & \text{otherwise} \end{cases}. \quad (2.36)$$

Correspondingly, the probability of such improvement can be calculated [93]:

$$P[I(\mathbf{x})] = \frac{1}{\hat{s}\sqrt{2\pi}} \int_{-\infty}^0 e^{-[I-\hat{y}(\mathbf{x})]^2/(2s^2)} dI. \quad (2.37)$$

At already sampled points, where the measurements are noiseless, the probability of improvement  $P[I(\mathbf{x})]$ , and thus the expected improvement  $E[I(\mathbf{x})]$ , will both be null as the objective values at those points are already known. Having this, and knowing  $\hat{y}$  and  $\hat{s}^2$ , the expected improvement using a distribution predicted by a Gaussian process is given by [93]:

$$E[I(y)] = \begin{cases} (y_{min} - \hat{y}(\mathbf{x}))\Phi\left(\frac{y_{min} - \hat{y}(\mathbf{x})}{\hat{s}(\mathbf{x})}\right) + s\phi\left(\frac{y_{min} - \hat{y}(\mathbf{x})}{\hat{s}(\mathbf{x})}\right), & \text{if } s > 0 \\ 0, & \text{if } s = 0 \end{cases}, \quad (2.38)$$

where,  $\Phi(\cdot)$  is the cumulative distribution function and  $\phi(\cdot)$  probability density function. Equation 2.38 is evaluated using the error function, which results in [93]

$$E[I(y)] = (y_{min} - \hat{y}(\mathbf{x})) \left[ \frac{1}{2} + \frac{1}{2} \operatorname{erf}\left(\frac{y_{min} - \hat{y}(\mathbf{x})}{\hat{s}(\mathbf{x})\sqrt{2}}\right) \right] + \hat{s}(\mathbf{x}) \frac{1}{\sqrt{2\pi}} \exp\left[-\frac{(y_{min} - \hat{y}(\mathbf{x}))^2}{2\hat{s}^2(\mathbf{x})}\right]. \quad (2.39)$$

This criterion takes into account the probability of improvement as well as the amount of improvement itself. This will allow the possible highlight of new samples further away from the current optimum that can be a local minimum. Moreover, as  $P[I(\mathbf{x})] = E[I(\mathbf{x})] = 0$  when  $\hat{s} = 0$ , even if the model ends up isolating a local minimum, an expectation of improvement in an unsampled area will still allow to find the global optimum. However, this process can be slow as it may take many iterations to converge [93].

### 2.5.3 WB2 and WB2S

On the other hand, the Watson and Barnes criterion (WB2), initially presented in [120], provides a balance between exploration and exploitation. It is more local than the EI criterion as it consists on a similar expression with an additional term corresponding to the predicted value [121]:

$$WB2 = \begin{cases} \hat{y}(\mathbf{x}) + (y_{min} - \hat{y}(\mathbf{x}))\Phi\left(\frac{y_{min} - \hat{y}(\mathbf{x})}{\hat{s}(\mathbf{x})}\right) + s\phi\left(\frac{y_{min} - \hat{y}(\mathbf{x})}{\hat{s}(\mathbf{x})}\right), & \text{if } s > 0 \\ 0, & \text{if } s = 0 \end{cases} \Leftrightarrow$$

$$\Leftrightarrow WB2 = \begin{cases} \hat{y}(\mathbf{x}) + E[I(y)], & \text{if } s > 0 \\ 0, & \text{if } s = 0 \end{cases}. \quad (2.40)$$

This criterion is used for "locating regional extremes" [120] aiming to minimize the expected value of the best evaluation after adding new infill samples.

Further, there is the WB2S method [96], that only differs from WB2 by adding a non-negative scaling factor  $s_f$  to the expected improvement:

$$WB2S = \begin{cases} \hat{y}(\mathbf{x}) + s_f E[I(y)], & \text{if } s > 0 \\ 0, & \text{if } s = 0 \end{cases}. \quad (2.41)$$

The scaling factor is added to keep the exploration property of the expected improvement, since in WB2 the magnitude of the term  $E[I(y)]$  is expected to decrease during the iterative process, possibly

leading the optimization to a local minimum [96].

Both methods are appropriate for expensive high-dimensional problems with limited time and computational resources, that require a convergence to the best possible solution while exploring multiple promising regions [96].

#### 2.5.4 Constrained search - Probability of feasibility

A possible approach for constrained problems, instead of constraining the optimization of the objective function, is to take into account the existing constraints along with the objective function and merge them all together in a new search function that will run unconstrained.

If the constraints are also modeled by surrogates, there are error measures for these quantities as well, besides the objective function. In a full probabilistic approach, if the constraint models present low predicted errors at a given point, and the surrogate shows a constraint violation, then the expectation of improvement will be low as well, but not zero, as there is still a finite chance that an evaluation of the constraint at that point proves to correspond to a feasible design. In opposition, large errors in the constraints, will imply a considerable possibility that the constraints predictions are wrong meaning that the new point will actually be feasible, thus there is a greater expectation of improvement [93].

Similarly to the calculation of the probability of improvement shown in equation 2.37, by following the same logic, the probability of the prediction being greater than the constraint limit, i.e., the probability that the constraint is met  $P[F(\mathbf{x})]$ , or probability of feasibility (PF) is obtained by:

$$P[F(\mathbf{x})] = \frac{1}{\hat{s}\sqrt{2\pi}} \int_0^{\infty} e^{-[F-\hat{g}(\mathbf{x})]^2/(2\hat{s}^2)} dG, \quad (2.42)$$

where  $g$  is the constraint function,  $g_{min}$  is the minimum allowed value,  $F = G(\mathbf{x}) - g_{min}$  is the measure of feasibility,  $G(\mathbf{x})$  is a random variable and  $\hat{s}^2$  corresponds to the variance of the model of the constraint [93].

A suggestion made by Schönlaui in [122], to include this concept in the search function, requires the assumption that the objective function and the constraints are uncorrelated. For example, since both models are independent,  $P[F(\mathbf{x})]$  can be coupled to the probability of improvement [93]:

$$P[I(\mathbf{x}) \cap F(\mathbf{x})] = P[I(\mathbf{x})]P[F(\mathbf{x})]. \quad (2.43)$$

Likewise,  $P[F(\mathbf{x})]$  can be combined with multiple search functions, such as the ones presented in 2.5.1, 2.5.2 and 2.5.3.

## 2.6 Optimization algorithm - Genetic Algorithm

Having defined the search method for the surrogate, follows the selection of an adequate optimization algorithm to operate the search.

Considering the case of a surrogate optimization with an initial data base of samples, population

methods are suitable as they make use of an initial set of design points, called individuals. Further, the collection of all individuals forms the population. The initial population is generated by random sampling. From multiple existing population methods, the one used to solve this problem was a genetic algorithm (GA).

Genetic algorithms are inspired in biological evolution, where fitter individuals have more probability of transmitting their genes to the next generations. The design point associated with each individual is called a chromosome [97]. Individuals with the best objective function values at each generation, are considered the fittest and will, in turn, pass their chromosomes to the next generation by means of crossover and mutation processes.

Initially, for a population of  $m$  chromosomes, a selection of  $m$  pairs is done to choose individuals to use as parents of the  $m$  children of the next generation. This selection is based on one of three criteria: truncation selection, tournament selection and roulette wheel selection. The first consists on randomly selecting a parent out of a subset of the best  $k$  chromosomes. In tournament selection,  $k$  chromosomes are randomly drafted and the parent will be the fittest of them. Lastly, roulette wheel selection, assigns to each chromosome a probability to be chosen, proportional to its performance in comparison with the rest of the population. The fitness of individual  $i$  can be set as  $\max\{y^{(1)}, \dots, y^{(m)}\} - y^{(i)}$  [97].

Crossover is the process that follows. It consists on combining the chromosomes of the parents to generate children. This can be achieved by applying either a single-point crossover, two-point crossover or uniform crossover. If only one crossover point is used, the first portion of the child chromosome will be identical to the one of one of the parents, and the final part to the other parent. The crossover point marks the position of the transition and it is established uniformly at random. Similarly, two crossover points will correspond to two transitions in the new chromosome. On the other hand, in uniform crossover, each element of the chromosome has the same probability (50%) of coming from either one of the two parents [97].

Finally, after the crossover, a mutation can occur. Mutations are important to introduce new traits that were not present in the initial population, that otherwise would not appear. In addition, it allows more exploration of the design space. Each element of the a chromosome has a small probability of suffering a mutation. For a chromosome with  $m$  elements, the mutation rate is usually  $1/m$  [97].

The population can widely cover the design space, allowing a better exploration that might avoid that the optimization gets stuck in local minima. Another advantage of this algorithm is that it is simple and straightforward to implement, however, it requires a large number of function evaluations, making it computationally expensive, especially for a large number of design variables [123].



# Chapter 3

## Optimization Problem - Implementation

### 3.1 Problem Formulation

#### 3.1.1 Mission Requirements

The first step to formulate the optimization problem is to identify and establish the requirements, their level of importance and priority. This is essential work in order to define the objective function and set constraints.

The aircraft's assigned mission is described in section 1.2. In addition to the mission profile, other requirements include a specified Maximum Take-Off Mass (MTOM), a minimum (dash) speed to allow progression in extreme wind conditions, minimum static stability requirements and maneuverability.

The following requirements were presented by DRDC thus they should be prioritized. Moreover, the list below does not cover anything related with the MAD sensor detection, as it falls out of the scope of this thesis.

1. Endurance: The aircraft is demanded to endure a flight that can range from 1 hour for a close-range surveillance mission, to more than 24 hours for a long-range mission;
2. Fuel: The total fuel weight to be carried will be directly related to the endurance. For close-range, the fuel mass must be as low as 10% of the aircraft's MTOM. This value may increase up to 50% when considering long-range;
3. Payload: The major concern regarding payload is being able to carry the MAD sensor and the electrical power supplies required for the correct functioning of the sensor. In addition, the positioning of the sensor must be such that the distance to engines and strong electrical currents does not affect the magnetic detection.
4. Speed and Wind: The aircraft must be able to track a submarine and withstand surface winds of approximately  $12m/s$ . Regarding speed, in the worst case scenario, the aircraft must be fast

enough to follow a submarine that is traveling in the same direction as the wind is coming from.

Taking into account all these demands, it was possible to define some problem parameters:

- MTOM equivalent to  $25kg$ . This value was selected due to current Canadian legislation on non-recreational UAV system operations stating that if the MTOM does not exceed  $25kg$ , there is an exemption from the requirement to obtain a Special Flight Operations Certificate (SFOC) [124].
- Cruise Speed of  $35m/s$ . Taking into account the claimed record speed of  $23m/s$  for a submerged vehicle held by the soviet K-222 Papa class, nuclear-powered submarine [125],  $V_{cr}$  was set to a higher value to ensure that the aircraft is able to follow any submarine, accounting for the average wind speed presented on the fourth item in the list of requirements above.
- Dash speed of  $60m/s$ , defined considering the value of  $V_{cr}$  and of stronger wind gusts velocity that may occur during storms in the Arctic, which rarely exceed  $25m/s$  [126].

The values set for each requirement were decided on team meetings and are displayed on table 3.1.

Table 3.1: Aircraft requirements for forward flight.

MTOM	$25kg$
Cruise speed	$35m/s$
Dash speed	$60m/s$
Stall speed	$20m/s$
Maximum operational Load factor	$3g$
Static margin ( $K_n$ )	10% MAC
$C_{VT}$	0.02

As mentioned earlier, this aircraft is intended to have VTOL capability. However, the configuration can be better optimized for cruise since the low speed landing requirement can be relaxed and a suitable higher stall speed can be selected that allows aerodynamic benefits in cruise, namely by increasing cruise ( $L/D$ ).

Although not a popular aircraft configuration, the canard configuration has the potential to be more aerodynamically efficient than a conventional configuration due to the always positive lift production on the canard surface for trimming purposes in any center of gravity (CoG) longitudinal position. This does not always happen in a conventional configuration. A static margin of 10% of the mean aerodynamic chord (MAC) was chosen for longitudinal stability.

One major drawback of the configuration is the requirement that the canard stalls before the wing for stability reasons, preventing the aircraft wing to achieve near stall  $C_L$  values which would be a penalty for landing speed and field length. Another would be the size or position of the vertical surfaces for lateral stability, particularly at low speeds. These drawbacks are both tackled by the VTOL capability that can potentially assist for stability and control during the low speed flight stages.

Thus, like stated in section 1.2, a canard configuration was chosen to be aero-structurally optimized according to the mission and aircraft requirements.

### 3.1.2 Objective Function

Taking into account the given requirements, the ultimate objective of the optimization problem is to maximize range. Range estimates can be calculated using the Breguet equation for propeller aircraft [127] shown below:

$$R = \frac{\eta (L/D)}{g BSFC} \ln \left( \frac{m_i}{m_f} \right), \quad (3.1)$$

where,  $\eta$ ,  $g$ ,  $(L/D)$ ,  $m_i$ ,  $m_f$  and  $BSFC$  are the propeller efficiency, the acceleration of gravity, the lift to drag ratio, the initial mass, the final mass at the end of the mission segment and the brake specific fuel consumption, respectively. The last is defined as the mass flow rate of fuel per unit of engine output power and it is measured in  $(kg/(W.s))$ , SI units. Since  $m_i$  and payload mass are assumed to be constant in this study, savings in structural mass will result in extended range due to increased fuel capacity and not exclusively because of a potential reduction in aerodynamic drag arising from a reduction in total aircraft mass.

However, at this stage of the design there is not enough information about the propulsion system to be used on the UAV, neither about all the different components that will be integrated and their masses. Hence, instead of setting equation 3.1 as the objective function, a multiobjective optimization including  $(L/D)$  and the structural mass  $m_S$  is chosen. The weighted sum method presented in section 2.2.2 allows to merge both objectives into a single function that measures the variation of range relative to a reference aircraft configuration.

It is now essential to establish criteria and assumptions to define the weights for each objective. As an approximation, range is assumed to vary linearly with both  $(L/D)$  and  $m_S$ . This translates into the following expression for the variation of range when compared to a reference:

$$\frac{\Delta R}{R_{ref}} = \frac{1}{R_{ref}} \frac{\partial R}{\partial(L/D)} \Delta(L/D) + \frac{1}{R_{ref}} \frac{\partial R}{\partial m_S} \Delta m_S. \quad (3.2)$$

The influence of the two components can be established from equation 3.1. It is straightforward that if the  $(L/D)$  ratio of a certain configuration is double of the reference  $(L/D)_{ref}$  while every other factor is equal, the range ( $R_{ref}$ ) will also increase 100% from the reference, accordingly. Thus, the derivative  $\frac{\partial R}{\partial(L/D)}$  can be easily obtained:

$$\frac{\partial R}{\partial(L/D)} = \frac{2R_{ref} - R_{ref}}{2(L/D)_{ref} - (L/D)_{ref}} = \frac{R_{ref}}{(L/D)_{ref}}. \quad (3.3)$$

The same process is used for the structural mass, which is considered to be a fraction of the final mass ( $m_S = m_S/m_f \times m_f$ ). Hence, if  $m_S$  is double of  $m_{S_{ref}}$ ,  $m_f$  will be  $(1 + m_{S_{ref}}/m_{f_{ref}})$  times higher. As follows, the derivative  $\frac{\partial R}{\partial m_S}$  is calculated:

$$\frac{\partial R}{\partial m_S} = \frac{\ln \left( \frac{m_i}{\left(1 + \frac{m_{S_{ref}}}{m_{f_{ref}}}\right) m_{f_{ref}}} \right) - \ln \left( \frac{m_i}{m_{f_{ref}}} \right)}{2m_{S_{ref}} - m_{S_{ref}}} \times \frac{\eta (L/D)}{g BSFC} = -\frac{\ln \left( 1 + \frac{m_{S_{ref}}}{m_{f_{ref}}} \right)}{m_{S_{ref}}} \times \frac{\eta (L/D)}{g BSFC}. \quad (3.4)$$

Substituting equations 3.3 and 3.4 in equation 3.2 results in:

$$\frac{\Delta R}{R_{ref}} = \frac{\Delta(L/D)}{(L/D)_{ref}} - \frac{\ln\left(1 + \frac{m_{S_{ref}}}{m_{f_{ref}}}\right)}{\ln\left(\frac{m_i}{m_{f_{ref}}}\right)} \frac{\Delta m_S}{m_{S_{ref}}}, \quad (3.5)$$

where,  $\Delta(L/D) = (L/D) - (L/D)_{ref}$  and  $\Delta m_S = m_S - m_{S_{ref}}$ .

Therefore, the weights of each component of the objective are defined as 1 and  $-\frac{\ln\left(1 + \frac{m_{S_{ref}}}{m_{f_{ref}}}\right)}{\ln\left(\frac{m_i}{m_{f_{ref}}}\right)}$  for  $(L/D)$  and  $m_S$ , respectively.

For the first reference configuration it was assumed that the structural mass was 50% of the empty aircraft mass ( $m_f$ ). This assumption was somewhat arbitrary but considered reasonable by the author.

At each iteration, the new final and structural reference masses ( $m_{f_{ref}}$  and  $m_{S_{ref}}$ ) will correspond to the previous plus the variation of structural weight from the prior best to the current best configuration (equation 3.6):

$$m_{f_{ref_i}} = m_{f_{ref_{i-1}}} + (m_{S_{best_i}} - m_{S_{best_{i-1}}}), \quad (3.6)$$

where  $i$  identifies the current iteration.

The reference design mentioned is updated during the optimization process and it will always correspond to the best configuration from the current set of analyzed samples. A configuration is considered the best if it is feasible and has the highest value of the prevailing objective function from all the samples.

Equation 3.5 is the objective function used for this optimization problem.

### 3.1.3 Design Variables and Parameterization

In order to evaluate the  $(L/D)$  and  $m_S$  values required to calculate the objective function value, aerodynamic and structural models were built based on the parameterization summarized in this section. A detailed description of the parameterization of the geometric model is presented on appendix A.

The design variables include geometric, aerodynamic and structural variables. The wing planform is defined using span ( $b_w$ ), leading edge sweep angle ( $\Lambda_w$ ) and bilinear chord and twist distributions defined with four parameters each ( $c_{root_w}, c_{disc_w}, c_{tip_w}, y_{c_{disc}}$  and  $\gamma_{w_{root}}, \gamma_{w_{disc}}, \gamma_{w_{tip}}, y_{\gamma_{disc}}$ ). The relative thickness and camber of the wing airfoil are also variable parameters ( $t_w$  and  $cbr_w$ ). The wingbox structure of the wing is defined in a similar way. The thickness distribution of the wing spars and skin are also defined by 4 parameters each ( $thk_{tip_{spar}}, thk_{disc_{spar}}, thk_{root_{spar}}$  and  $thk_{tip_{skin}}, thk_{disc_{skin}}, thk_{root_{skin}}$ , together with  $y_{c_{disc}}$ ). The chordwise position of the aft spar of the wing is fixed as 70% of the local chord while the position of the front spar ( $pos_{f_{spar}}$ ) can vary between 10% and 25% of the local chord.

A trapezoidal winglet geometry parameterization is also included with span ( $b_{w_{glt}}$ ), taper ratio ( $\lambda_{w_{glt}}$ ) and winglet sweep ( $\Lambda_{w_{glt}}$ ) as variable parameters. Relative thickness and camber of the winglet airfoil are also design parameters ( $t_{w_{glt}}$  and  $cbr_{w_{glt}}$ ). Figure 3.1 shows a possible configuration for the wing plus winglet.

The canard planform is rectangular with a variable area ( $S_c$ ) and span ( $b_c$ ). The camber of the canard

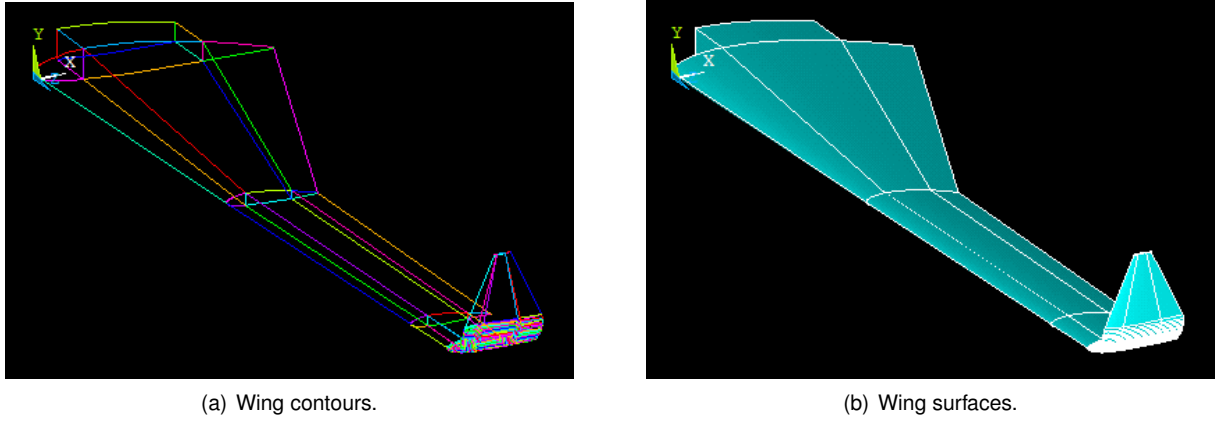


Figure 3.1: Wing representation.

airfoil is other variable parameters in the design ( $t_c$  and  $cbr_c$ ). A constant thickness tube is the structure modeled to support the canard loads and its radius and thickness values are design parameters ( $r_{tube}$  and  $thk_{tube}$ ).

Root chord, taper ratio and span are the parameters defining the vertical fin ( $c_{root_f}$ ,  $\lambda_f$  and  $b_f$ , respectively). It has a fixed symmetric airfoil and only one spar located at 70% of its chord.

All airfoils are defined by the NACA 4-digit airfoil parameterization [128].

Distance between wing and canard aerodynamic centers ( $l_c$ ) and canard vertical position ( $z_c$ ) are also variable and define the lifting surfaces completely in the configuration.

Lastly, the structure of the fuselage will consist on two identical laminate spars with constant thickness and parallel to each other along the length of the fuselage. Each spar is designed with a circular hole to fit the canard tube spar and a cut in the upper part to support the wingbox (seen in figure A.3 on section A.3 of appendix A).

As regards the baseline shape of the fuselage, it was previously defined using the SOLIDWORKS software [129] by Bruno Luís, as part of his master thesis [1], with the main focus of accommodating the MAD sensor on the nose of the aircraft. The resulting shape is presented on figure 3.2 and it is the one considered throughout this project. Thickness of fuselage spars ( $thk_{fuse}$ ) as well as spanwise and transverse fuselage scaling factors ( $y_{scale}$  and  $z_{scale}$ ) finalize the set of variable configuration parameters used as design variables during the optimization. Table 3.2 below summarizes the design variables used in this optimization.

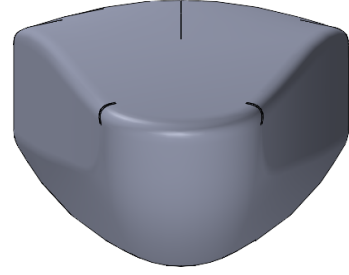
### 3.1.4 Constraints

Aiming to reduce the computational resources required for the optimization, namely HF CFD analyses, constraints related to geometry, trim conditions, longitudinal, directional and lateral stability and stall conditions were taken as considerations during the definition of the design variables and their boundaries and during the analysis of the different configurations.

The payload requires a minimum distance between the fuselage spars so it can fit inside and be attached to them. This limitation is considered in the bounds of the related geometric variables, always



(a) Longitudinal view of the fuselage.



(b) Front section view of the fuselage.

Figure 3.2: Fuselage geometry.

Table 3.2: Design variables plus correspondent lower and upper bounds with respective units.\*  $pos_{bot}$  and  $pos_{top}$  correspond to the positions on the fuselage spar with a safety margin to the lower and upper edges, respectively.

Variable	L.B	U.B	Variable	L.B	U.B
$y_{scale}$ [ ]	1	1.05	$\gamma_{w_{tip}}$ [deg]	$\gamma_{w_{disc}} - 3$	$\gamma_{w_{disc}}$
$z_{scale}$ [ ]	1	1.05	$y_{\gamma_{disc}}$ [m]	$0.3b_w/2$	$0.7b_w/2$
$thk_{fuse}$ [m]	0.002	0.005	$\Lambda_w$ [deg]	0	30
$r_{tube}$ [m]	$0.2c_c t_c$	$0.9c_c t_c$	$t_w$ [ ]	0.1	0.15
$thk_{tube}$ [m]	$0.2r_{tube}$	$r_{tube}$	$cbr_w$ [ ]	0	0.07
$pos_{fspar}$ [m]	$0.1c(y)$	$0.25c(y)$	$b_{wgl}$ [m]	0.05	0.2
$thk_{tip_{spar}}$ [m]	$8.0 \times 10^{-4}$	$1.5 \times 10^{-3}$	$\lambda_{wgl}$ [ ]	0.2	0.6
$thk_{disc_{spar}}$ [m]	$8.0 \times 10^{-4}$	$3.0 \times 10^{-3}$	$\Lambda_{wgl}$ [deg]	0	30
$thk_{root_{spar}}$ [m]	$1.0 \times 10^{-3}$	$5.0 \times 10^{-3}$	$t_{wgl}$ [ ]	0.08	0.12
$thk_{tip_{skin}}$ [m]	$6.0 \times 10^{-4}$	$1.5 \times 10^{-3}$	$cbr_{wgl}$ [ ]	0	0.02
$thk_{disc_{skin}}$ [m]	$6.0 \times 10^{-4}$	$2.0 \times 10^{-3}$	$b_c$ [m]	1	2
$thk_{root_{skin}}$ [m]	$6.0 \times 10^{-4}$	$3.0 \times 10^{-3}$	$S_c$ [m <sup>2</sup> ]	$0.15S_w$	$0.25S_w$
$b_w$ [m]	2.3	4	$l_c$ [m]	1.5	3.5
$c_{root_w}$ [m]	0.15	0.5	$z_c$ [m]	$pos_{bot}^*$	$pos_{top}^*$
$c_{disc_w}$ [m]	0.1	$c_{root_w}$	$cbr_c$ [ ]	0	0.07
$c_{tip_w}$ [m]	0.1	$c_{disc_w}$	$c_{root_f}$ [m]	0.1	0.2
$y_{disc}$ [m]	$0.3b_w/2$	$0.7b_w/2$	$\lambda_f$ [m]	0.2	0.6
$\gamma_{w_{root}}$ [deg]	-3	10	$b_f$ [m]	0.2	0.4
$\gamma_{w_{disc}}$ [deg]	$\gamma_{w_{root}} - 3$	$\gamma_{w_{root}}$			

assuring that the fuselage has the minimum width.

It is essential that the wing always stalls after the canard so that the aircraft can recover without entering an irreversible stall, which translates to  $C_{L_c} > C_{L_w}$ , where the subscripts c and w indicate canard and wing respectively. Assuming the wing generates 80% of the total lift and that the remaining lift is generated by the canard, the canard will have a high probability to stall first if the relation  $(S_c/S_w) < 0.25$  is verified, where  $S$  represents the lifting surface area. Said relation is included as a consideration in the parameterization of the geometry, once again limited by the bounds on the design variables.

Other constraints were included during the CFD analysis of a configuration, including two trim conditions: lift equal to the total weight; and zero pitching moment ( $C_m = 0$ ). Additionally, a positive static margin ( $K_n > 0$ ) that ensures a longitudinally stable aircraft [130] condition is also imposed. By allowing

the position of the CoG, the incidence of the canard and the angle of attack (AoA) to change in each analysis, it is guaranteed the mentioned constraints will be respected for a specific combination of the three parameters.

Directional and lateral stability requirements are attained by sizing the vertical fin geometry using the previously determined volume coefficient equal to 0.02, assumed to be sufficient for good handling conditions in flight [131].

The only constraint in this optimization procedure that requires a direct evaluation using a structural model is the structural failure criterion at the ultimate load case considered, with a vertical load factor of 4.5g. Since the modeled structure is assumed to be entirely made of Carbon Fiber Reinforced Polymers (CFRP), the Tsai-Wu failure criterion for composite materials (section 2.1.1.2) was used for this purpose. The feasible region regarding this constraint will be where the Tsai-Wu failure index is smaller than 1.

### 3.1.5 Optimization Statement

In summary, the optimization problem can be presented as the maximization of range, with respect to the design variables shown in table 3.2 limited to the respective bounds, and subject to the failure constraint, according to which the maximum Tsai-Wu ratio index must be smaller than 1.

As the goal is to maximize range, the function provided to the optimizer for minimization is the symmetric of equation 3.5.

Having this, the optimization problem can be stated as:

$$\begin{aligned}
 &\text{minimize} && -\frac{\Delta R}{R_{ref}} \\
 &\text{w.r.t} && y_{scale}, z_{scale}, thk_{fuse}, r_{tube}, thk_{tube}, pos_{fspar}, thk_{tip_{spar}}, thk_{disc_{spar}}, thk_{root_{spar}}, thk_{tip_{skin}}, \\
 & && thk_{disc_{skin}}, thk_{root_{skin}}, b_w, c_{root_w}, c_{disc_w}, c_{tip_w}, y_{c_{disc}}, \gamma_{w_{root}}, \gamma_{w_{disc}}, \gamma_{w_{tip}}, y_{\gamma_{disc}}, \Lambda_w, t_w, \\
 & && cbr_w, b_{w_{glt}}, \lambda_{w_{glt}}, \Lambda_{w_{glt}}, t_{w_{glt}}, cbr_{w_{glt}}, b_c, S_c, l_c, z_c, cbr_c, c_{root_f}, \lambda_f, b_f \\
 &\text{subject to} && \text{Max. Tsai-Wu failure index} < 1
 \end{aligned} \tag{3.7}$$

## 3.2 MDA Procedure

The MDA of this optimization problem is mostly based on two disciplines, structures and aerodynamics.

In order to have a fully defined MDA, on which the optimization will be based, it is necessary to establish a structured architecture that includes and couples all disciplines.

### 3.2.1 Discipline Coupling

The analysis conducted throughout this project can be divided in four major steps:

1. Generation of geometry based on the inputs for the design variables.
2. An initial LF estimation of the aerodynamic loading on the wing and the canard based on Prandtl's LLT (section 2.1.2.1).
3. A structural FEM analysis executed to calculate the structural mass as well as to evaluate the structural integrity and strength of the UAV by applying the previously determined aerodynamic loads.
4. A HF CFD analysis is used to determine both trim and stability conditions, and also to gather performance results.

The analysis of each configuration is sequential, following the presented order. Moreover, step 4 is only performed if the configuration proves to be structurally feasible on the previous step. A more detailed description of each main step mentioned above is presented below. In addition, the whole process is represented on the following flowchart (figure 3.3).

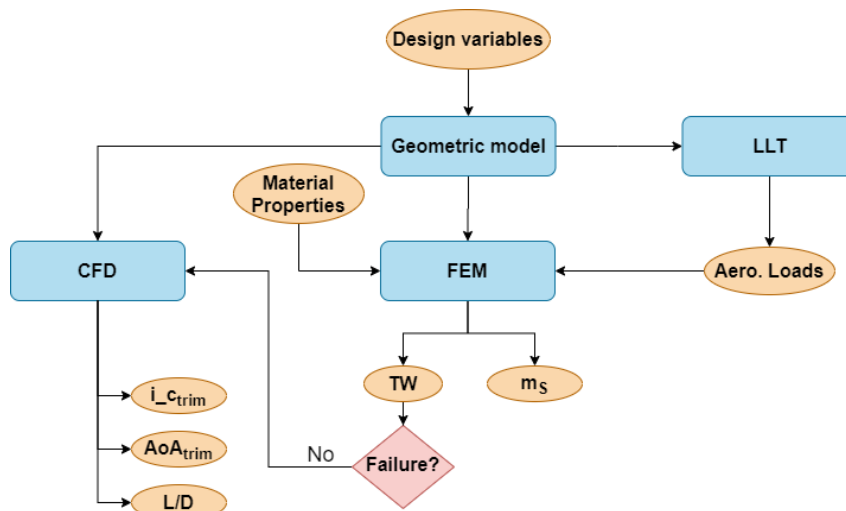


Figure 3.3: MDA architecture.

### 3.2.1.1 Geometric models

Two geometric models are generated from the set of design variables for each configuration, one corresponds to the structure of the aircraft, while the other represents the outer surface.

The structural model is created in ANSYS Mechanical APDL [102]. Besides the parameterization and dimensions, it is also necessary to supply the model with the materials correspondent to each component, along with the respective properties. As mentioned above, the whole structure is made of CFRP, in particular, carbon fiber laminate plates. The composite sheets used in the layers of the laminates can be either unidirectional (UD) carbon-epoxy, or bidirectional woven carbon-epoxy. The properties of both materials are presented on table 3.3. The minimum stress values with negative sign correspond to compression stresses.

Table 3.3: Materials properties.

	UD Carbon-Epoxy	Woven Carbon-Epoxy
$\rho_c [kg/m^3]$	1449.1	1422.9
$E_x [MPa]$	$1.17 \times 10^5$	67100
$E_y [MPa]$	6070	67100
$E_z [MPa]$	6070	7500
$\nu_{xy} [ ]$	0.3	0.05
$\nu_{yz} [ ]$	0.42	0.3
$\nu_{xz} [ ]$	0.3	0.3
$G_{xy} [MPa]$	3100	4000
$G_{yz} [MPa]$	1600	1600
$G_{xz} [MPa]$	3100	4000
$\sigma_{x_{max}} [MPa]$	1453	711
$\sigma_{x_{min}} [MPa]$	-368	-356
$\sigma_{y_{max}} [MPa]$	39.6	711
$\sigma_{y_{min}} [MPa]$	-45	-356
$\sigma_{z_{max}} [MPa]$	39.6	50
$\sigma_{z_{min}} [MPa]$	-45	-150
$\tau_{xy_{max}} [MPa]$	41	54
$\tau_{yz_{max}} [MPa]$	40	39
$\tau_{xz_{max}} [MPa]$	40	39
$h_n [mm]$	0.165	0.208

All spars are composed of a stacking of woven layers only, except the canard tube. The later is entirely made of UD carbon, with a minimum of 6 layers. The fuselage and wing plus winglet spars have a minimum of 10 and 4 layers, respectively. The vertical tail has a fixed number of 5 layers.

Regarding the skin laminates, the wingbox section has a minimum number of 3 woven layers, yet more layers are added according to the defined thickness. These layers can be either UD or woven, depending on the already existing layers. The stacking sequence with the addition of new layers follows the scheme displayed in figure 3.4. The remaining skin components of the wing, as well as the vertical fin have a fixed number of 3 woven layers.

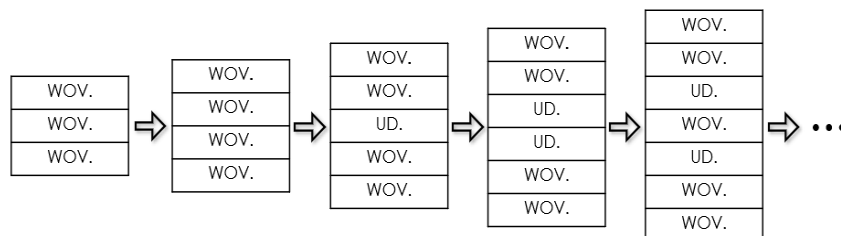


Figure 3.4: Stacking sequence of the wingbox skin with the addition of new layers.

Secondly, the outer mold line (OML) of the entire aircraft's surface in forward flight configuration is generated using SOLIDWORKS [129].

Figure 3.5 and Figure 3.6 depict the OML and the structural model of an example configuration, respectively.

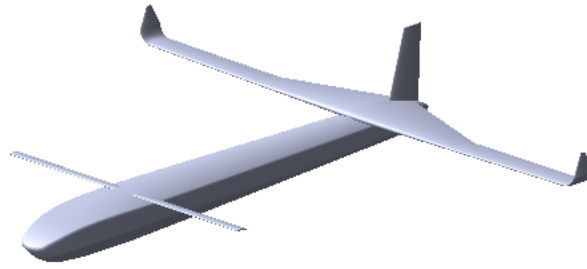


Figure 3.5: Outer mold line of an example configuration.

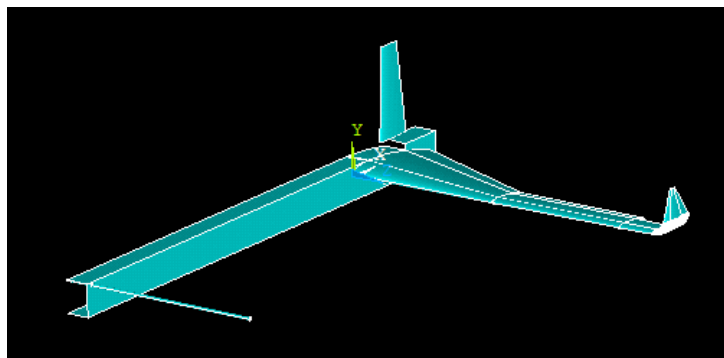


Figure 3.6: Structural model of an example configuration.

### 3.2.2 Aerodynamic Loading estimation

The load distribution on both wing and canard are obtained from Prandtl's LLT coupled with taking as inputs the geometries and position of the two lifting surfaces, considering an identical NACA 2412 airfoil for both surfaces. Moreover, the loads are obtained for a trimmed  $4.5g$  pull up maneuver, which is considered the ultimate load case.

### 3.2.3 Structural Analysis

In order to determine the structural weight and the Tsai-Wu failure index, two FEM simulations are performed making use of the ANSYS Mechanical APDL software [102]. In the first simulation, the geometry of half of the aircraft is imported. Additionally, the properties of the composite materials used, as well as the laminate stacking sequence for each component are also provided in the structural model. Two element types were considered, 'SHELL181' and 'MPC184'. The first is used to represent all structural elements of composite laminates, while the second is used for the connections between the different components of the structure.

As only half of the structure is represented, it is required to impose some boundary conditions in the symmetry plane, in particular, zero displacement in the pitch axis direction, as well as zero rotation in

the roll and yaw axes, for all the nodes on the symmetry plane of the aircraft.

From the first analysis it is possible to determine the mass of the structure and the associated CoG position. These are then used to calculate the mass and location for a mass point that is added to the model so that the total mass corresponds to the whole aircraft mass and the center of mass is at the desired location previously estimated from the trim equations with the aerodynamic loading.

Thereafter, the second simulation is run after loading the surfaces of the wing and the canard with the predetermined aerodynamic loads for a load factor of 4.5. After solving, the Tsai-Wu failure criterion is evaluated for the whole structure and the maximum value saved for the posterior surrogate model construction. The deformed shape together with the evaluation of the Tsai-Wu criterion for an example configuration are shown in figures 3.7 and 3.8

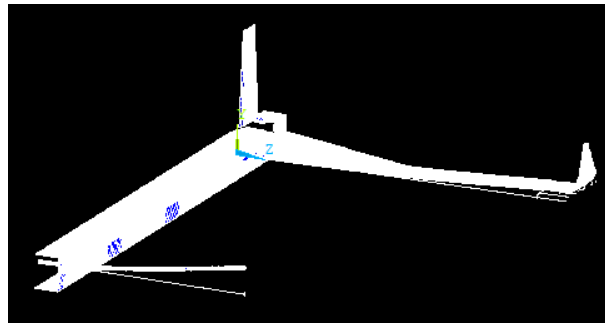


Figure 3.7: Deformed structure shape relative to undeformed shape contours.

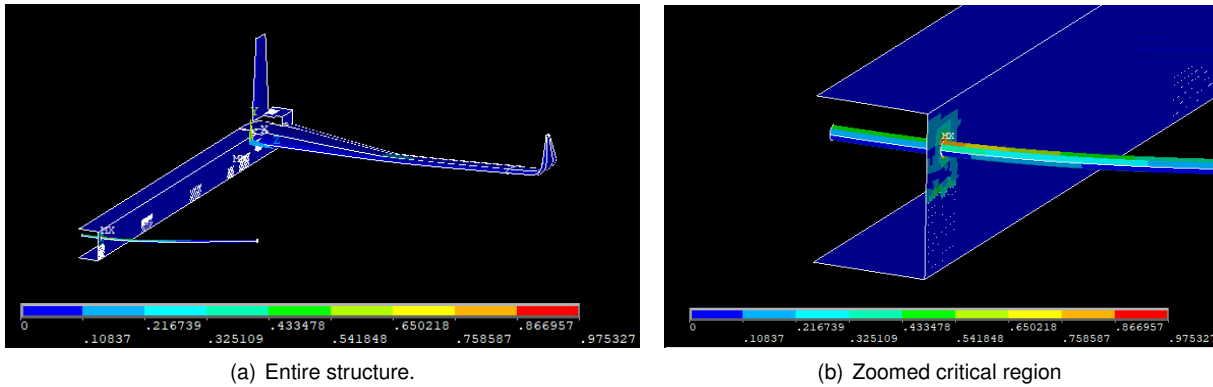


Figure 3.8: Evaluation of Tsai-Wu failure criterion.

If the configuration is feasible (the maximum value of the Tsai-Wu failure index is smaller than 1), said configuration will proceed to the CFD analysis.

### 3.2.4 CFD Analysis

The software employed to perform the HF aerodynamic analysis is the ANSYS CFX [109] with the SST set as the turbulence model (section 2.1.2.2). The analysis is executed on the OML model which is uploaded into the simulation.

Before running the simulation, it is essential to converge the mesh by setting the element size parameters, thus defining the number of elements. The parameters considered to vary the number of elements

are the maximum element size for both the UAV and the airflow, the growth rate and the curvature normal angle for the elements on the surface of the aircraft. Figure 3.9 shows the variation of drag in  $N$  with the number of elements of the OML.

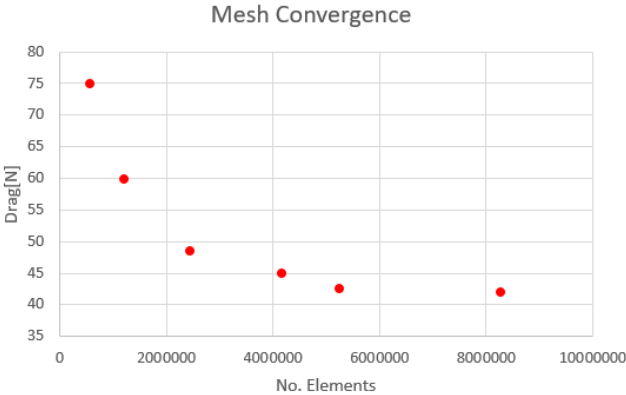


Figure 3.9: Mesh convergence test for the CFD analysis (Drag  $D[N]$  vs. total number of elements).

Figure 3.9 shows the mesh convergence test that was performed in order to set the number of elements for the model. It verifies that the drag decreases with the increasing number of elements. Furthermore, the drag shows a variation of only 1.2% for more than 5257669 elements. From these results, it can be assumed that the mesh is converged beyond this point. The selected number of elements, for which convergence was reached, corresponds to the following values for the defining parameters:

- Aircraft maximum element size of  $0.01m$
- Airflow maximum element size of  $0.5m$
- Growth rate of 1.2
- Curvature normal angle for the elements on the surface of the aircraft equal to 10 degrees.

The mesh used is unstructured, composed by tetrahedral elements and it is depicted in figure 3.10.

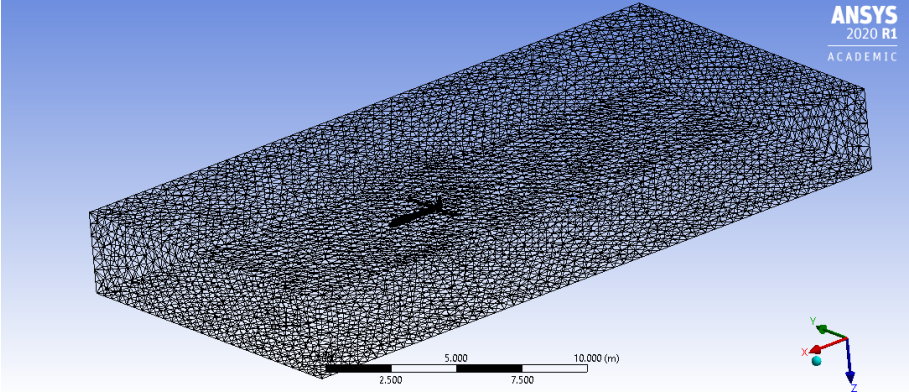


Figure 3.10: CFD mesh.

The evaluation of the aerodynamic performance is performed in 5 steps to attain the  $(L/D)$  for a trimmed flight condition at cruise speed:

1. In the first simulation the configuration is run with the canard incidence ( $i_c$ ) at 0 degrees and for three different angles of attack. By determining the values of  $C_L$  and pitching moment coefficient ( $C_m$ ) for all three conditions it is possible to estimate the position of the neutral point based on the AoA ( $\alpha$ ),  $dC_L/d\alpha$  and  $dC_m/d\alpha$  derivatives estimates, and subsequently the corrected CoG position, using the expression  $dC_m/d\alpha = -(dC_L/d\alpha)K_n$  [130] and assuming a static margin of 10%.
2. The newly obtained CoG position is used to update the  $C_m$  value for the three AoA.
3. A new CFD run with a deflected  $i_c$  by 2 degrees is used to determine the derivatives  $dC_L/di_c$  and  $dC_m/di_c$ . These derivatives are then employed to estimate the value of  $i_c$  which trims the aircraft at an AoA of zero degrees.
4. With the new estimation of  $i_c$  implemented to the geometry, a simulation run with the new model for the three angles of attack takes place, obtaining new values of  $dC_L/d\alpha$ ,  $dC_m/d\alpha$ ,  $C_{L\alpha=0}$  and  $C_{m\alpha=0}$  for this specific  $i_c$ . These new values allow for a more accurate linearization of the lift and pitching moment around the previously calculated near trim configuration.
5. Finally, a linear system of two equations for  $C_L$  and  $C_m$ , shown in Equation 3.8 ( $\Delta i_c$  is the difference between  $i_{c_{trim}}$  and the first estimation of  $i_c$  used in step 4), is built and solved for the  $i_{c_{trim}}$  and  $\alpha_{trim}$ , i.e., trim condition. A validation simulation is then executed to verify the trim as well as to retrieve the value of  $(L/D)$  for the aircraft trimmed configuration.

$$\begin{cases} C_{L_{trim}} = \frac{dC_L}{d\alpha} \alpha_{trim} + \frac{dC_L}{di_c} \Delta i_c + C_{L\alpha=0} \\ C_{m_{trim}} = 0 = \frac{dC_m}{d\alpha} \alpha_{trim} + \frac{dC_m}{di_c} \Delta i_c + C_{m\alpha=0} \end{cases} \quad (3.8)$$

### 3.3 MDO methodology

#### 3.3.1 Surrogate models

Three Kriging based stochastic surrogate models were built in MATLAB [132] for a complete approximation of the solution. Two of them were generated from the structural data, modeling the constraint value corresponding to the Tsai-Wu failure index, and the structural mass required for the objective function, respectively. These include all design variables and represent 37-dimensional spaces. The other model represents the performance ratio  $(L/D)$ , resultant from the aerodynamic data, and it is also used in the construction of the objective function. Differently, the  $(L/D)$  model does not include all 37 dimensions but only 27, as the aerodynamic analysis is completely independent of 10 structural variables, being these the two variables defining the canard spar tube ( $r_{tube}$  and  $thk_{tube}$ ), the position of the front spar of the wing ( $pos_{spar}$ ), as well as the 6 variables specifying the spar and skin thicknesses of the wing

( $thk_{tip_{spar}}$ ,  $thk_{disc_{spar}}$ ,  $thk_{root_{spar}}$ ,  $thk_{tip_{skin}}$ ,  $thk_{disc_{skin}}$  and  $thk_{root_{skin}}$ ) and the thickness of the fuselage spar ( $thk_{fuse}$ ).

The DACE MATLAB toolbox [133] was applied to produce the Kriging approximations of the computer models.

A sampling plan with 41 samples, obtained from Latin-Hypercube sampling (section 2.3.1), was employed to generate the initial surrogates.

A cross-validation comparison was performed for the structural models of both Tsai-Wu and structural mass with the purpose of selecting the regression model that better predicts the existing samples. Two regression models from the DACE toolbox were considered and implemented in the Kriging surrogates, a constant and a linear regression models. The average and maximum relative errors ( $e$ ) were registered for both quantities and for the two types of regression. Table 3.4 shows the collected results.

Table 3.4: Cross-validation results for the Tsai-Wu and structural mass models, with a constant and a linear regression.

Regression:	Tsai-Wu		Structural mass	
	Constant	Linear	Constant	Linear
$\bar{e}$	1.25	2412.88	0.20	36.89
$e_{max}$	7.59	98373.48	0.99	1527.62

The constant regression proved to be a better approximation of the initial samples for both the Tsai-Wu and  $m_S$ , thus being selected.

However, only 8 out of the 41 samples are structurally feasible, and thus available to build the model for ( $L/D$ ), as only the feasible design points proceed to the aerodynamic analysis. With 8 samples for a total of 27 design variables, a constant regression is used for the ( $L/D$ ) surrogate, since a linear regression requires a total of  $n + 1$  sampled points, being  $n$  the number of design variables [133].

In all three models, the fluctuations around the trend are determined by Gauss correlations also included in the used toolbox.

### 3.3.2 Search Algorithm

#### 3.3.2.1 Method comparison

A comparison between different search methods was made with the purpose of selecting the most adequate method for the problem defined in section 3.1, i.e., the most efficient, as well as effective and consistent.

The objective function chosen for minimization in this study was the Branin function [93]. It is a two-variable function defined by the following expression:

$$f(x) = \left( x_2 - \frac{5.1}{4\pi^2} x_2 + \frac{5}{\pi} x_1 - 6 \right)^2 + 10 \left[ \left( 1 - \frac{1}{8\pi} \right) \cos x_1 + 1 \right], \quad x_1 \in [-5, 10], x_2 \in [0, 15]. \quad (3.9)$$

This function has three global minima  $f(\mathbf{x}^*) = 0.397887$ , at  $\mathbf{x} = (-\pi, 12.275)$ ,  $(\pi, 2.275)$  and  $(9.42478, 2.475)$ .

A quadratic constraint function  $g(\mathbf{x})$  (equation 3.10) was considered during the optimization:

$$g(\mathbf{x}) = 0.9(x_1 - 6)^2 + x_2 - 10 \leq 0. \quad (3.10)$$

As a result, the minimum at  $\mathbf{x} = (\pi, 2.275)$  is the only one in the feasible region, near the boundary.

Figure 3.11 (a) illustrates in three dimensions the function from equation 3.9, while figure 3.11 (b) depicts a projected view of the same function in the considered design space, including the constraint boundary  $g(\mathbf{x})$ , delineated by the red dashed line, together with the global optimum, identified by the green cross.

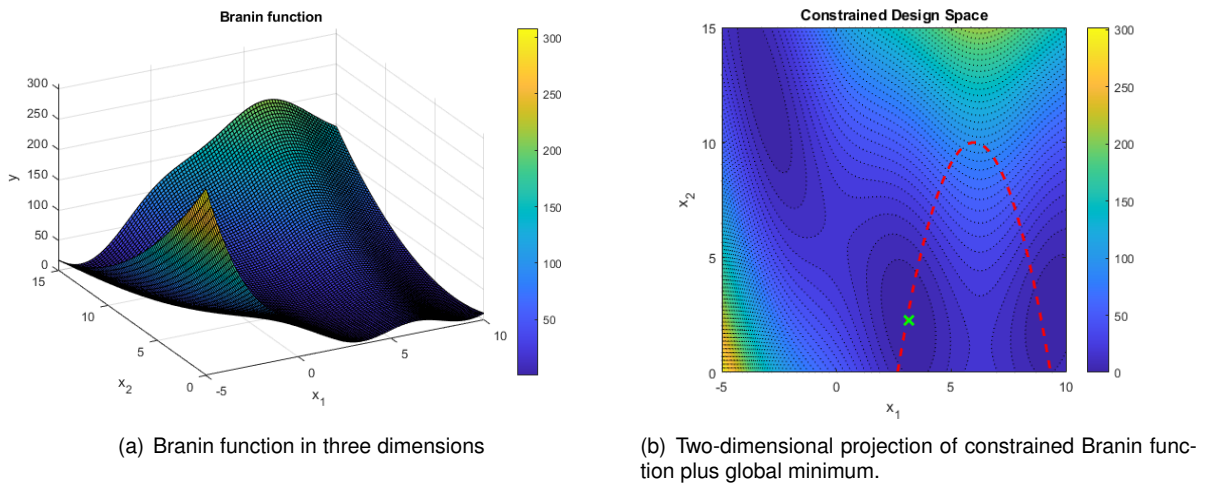


Figure 3.11: Representation of the Branin function.

The optimization problem is now constrained and admits only one global minimum, making it more representative of an engineering problem.

Four different search methods, previously presented in section 2.5, were chosen for comparison, being these, the EI, WB2, and the previous two plus the implementation of the probability of feasibility  $P[F(y)]$ .

The incorporation of the PF in the search function was done making use of a sinusoidal function as follows:

$$\begin{cases} f_{s_{PF}}(\mathbf{x}) = f_s(\mathbf{x}) \times \sin\left(P[F(y)] \times \frac{\pi}{2}\right)^n, & f_s < 0 \\ f_{s_{PF}}(\mathbf{x}) = f_s(\mathbf{x}) \times \left(1.1 - \sin\left(P[F(y)] \times \frac{\pi}{2}\right)^n\right), & f_s \geq 0 \end{cases}, \quad (3.11)$$

where,  $f_{s_{PF}}$  and  $f_s$  are the search functions with and without the probability of feasibility, respectively, and  $n$  is a factor that regulates the strictness of the boundaries.

Using the  $P[F(y)]$  in the sine function changes the trend of the feasibility quantity from linear to a curve, that returns higher values of feasibility than the  $P[F(y)]$  itself, thus making the search less conservative. The influence of  $n$  is shown in figure 3.12. The smaller  $n$  is, the greater the increase in

the probability of feasibility will be. Further, for smaller  $n$ 's, this difference is more significant for lower  $P[F(y)]$  values. For the comparison study,  $n$  was set to 0.25, allowing to increase the exploration in the optimization.

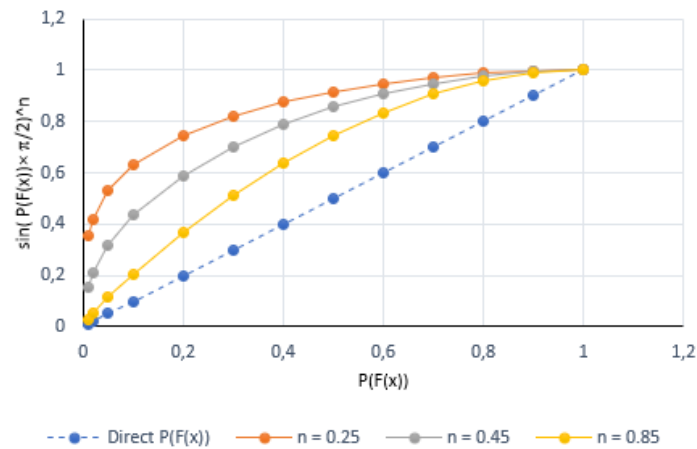


Figure 3.12: Variation of the influence of the probability of feasibility with the parameter  $n$ .

A GA (section 2.6) was used to search the surrogate. The optimization was performed in MATLAB [132] using the function 'ga' with the properties defined in figure 3.13.

```

Set properties:
ConstraintTolerance: 1.0000e-08
FunctionTolerance: 1.0000e-08
MaxGenerations: 40
PopulationSize: 50

```

Figure 3.13: Relevant properties of 'ga' function.

In order to accomplish a complete comparison, 14 different initial sampling plans were used. The sampling plans differ from each other in the number of samples, sampling method from which they were obtained, and also in the capacity to cover the design space, measured by the Pairwise distances method shown in section 2.3.2.

Table 3.5 shows the results of each method for all the sets of samples. Sampling plans 7 and 8 were randomly generated while the remaining result from Latin-Hypercube sampling (section 2.3.1).

It is verified that WB2+PF is the method with the fastest average convergence, with a global average of 6.5 iterations, followed closely by WB2 that presents an average of 7.8 iterations. Differently, EI and EI+PF show slower convergence rates, taking an average of 25.4 and 12.3 iterations to converge, respectively.

Additionally, EI+PF is the method with more successful optimizations, as none of the fourteen attempts failed. WB2 also shows effective results with 13 successful runs and 1 failed optimization, corresponding to sampling plan 3. WB2+PF failed one time more than WB2, with a total of 2 failures for sampling plans 2 and 4. On the other hand, EI is very inconsistent, as only 6 of the 14 optimization runs were successful. Failures are represented in the convergence column (Conv.) of table 3.5 by the symbol  $\times$ . Some of the failures are due to the GA reaching the defined number of maximum generations (50),

Table 3.5: Test optimization results for each method, including an indication of convergence along with the number of iterations.

Sampling Plan [no. samples]	Minimum Pairwise Dist.	WB2		EI		WB2+PF		EI+PF	
		Conv.	It	Conv.	It	Conv.	It	Conv.	It
1 [3]	0.3913	✓	9	×	Max.It	✓	7	✓	14
2 [3]	0.4420	✓	28	×	Max.It	×	–	✓	14
3 [3]	0.5029	×	–	×	–	✓	11	✓	8
4 [3]	0.7153	✓	8	✓	7	×	–	✓	18
5 [3]	0.7040	✓	7	✓	9	✓	10	✓	25
6 [3]	0.6582	✓	4	✓	16	✓	5	✓	10
7 [3]	0.5728	✓	4	×	–	✓	5	✓	14
8 [5]	0.0783	✓	6	✓	7	✓	5	✓	7
9 [5]	0.3079	✓	5	×	Max.It	✓	7	✓	9
10 [5]	0.2389	✓	13	×	–	✓	5	✓	15
11 [5]	0.3402	✓	7	×	–	✓	4	✓	9
12 [10]	0.1212	✓	3	✓	3	✓	10	✓	13
13 [10]	0.1007	✓	3	✓	12	✓	5	✓	5
14 [10]	0.0932	✓	4	×	Max.It	✓	4	✓	11

displayed by the expression "Max.It". The remaining failures, represented by "–", result from the inability of the 'ga' function to find new points within the population, that have better predicted objective values than the existing samples.

A thorough interpretation of the results allows to understand how the convergence changes with the number of initial samples. For the method using the WB2 alone, it is possible to see that the average number of iterations decreases significantly with the number of samples. The average changes from 10 to 7.75 and to 3.3 iterations, for 3, 5 and 10 initial samples, accordingly. This corresponds to a total improvement of 67%. WB2+PF and EI+PF also show a reduction, yet smaller, on the number of required iterations, with improvements of 17% and 34%, respectively. Differently, for EI, although a reduction of 18% is also verified, it is important to emphasize that the iterations of the sampling plans 1, 2, 9 and 14 are limited to the maximum of 50, and it would require more iterations for the optimization to converge.

From the observation of the results along iterations for sampling plan 12, it was noticed that the implementation of the PF shown in equation 3.11 is not well set for all possibilities, more specifically, when  $f_s$  is positive. Figures 3.14 and 3.15 depict this flaw for iterations 5 and 6 of the optimization with WB2+PF corresponding to sampling plan 12. These figures show the new design point prediction (black cross), the existing samples at the current iteration (white crosses), as well as the approximation of the constraint (red dashed line), represented on the plot of the surrogate of the Branin function (left side plots), and also on the plot of the objective search function (right side plots).

The way it is set, when the goal is to minimize the objective function and  $f_s$  is positive, a high  $P[F(y)]$  should influence  $f_s$  by decreasing its absolute value, while keeping it positive, thus the use of the term  $(1.1 - \sin(P[F(y)] \times \frac{\pi}{2})^n)$ . When a design point is certainly feasible ( $P[F(y)] = 1$ ), the sine will also be equal to 1 and the whole term will have its minimum possible value of 0.1. However, if the objective value keeps oscillating between negative and positive, the search function may not have the desired

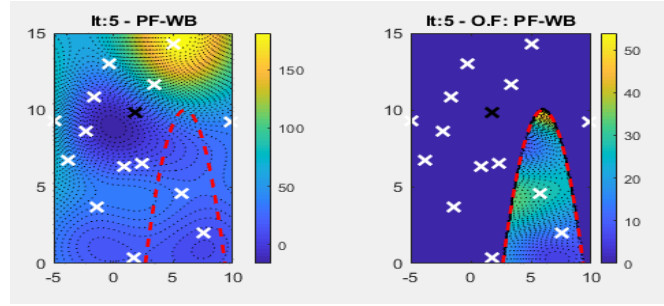


Figure 3.14: Fifth iteration prediction of sampling plan 12 with WB2+PF method.

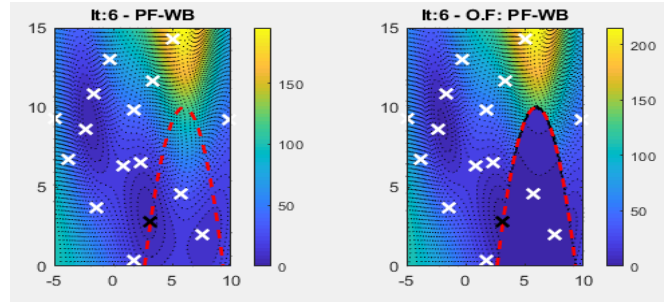


Figure 3.15: Sixth iteration prediction of sampling plan 12 with WB2+PF method.

behavior. Considering that, at a given iteration, there is a region with a correspondent negative value for  $f_s$  and it is surely unfeasible,  $P[F(y)]$  will be equal to zero, making  $f_{s_{PF}}$  also equal to zero. If there is any region where  $f_s$  is positive, even if the boundaries are well defined and  $P[F(y)]$  is equal to one,  $f_{s_{PF}}$  will always be positive. Figure 3.14 displays this specific situation, where the optimizer will prefer the point that is already acknowledged to be unfeasible, over the feasible points with positive values, which is not correct.

In opposition, on the given example, the values of the search function at the unfeasible region turned positive in the next iteration, driving the optimizer to make a new feasible prediction, close to the boundary and close to the real optimum (figure 3.15).

After analyzing all results in detail, EI showed to be the least consistent method, with only 43% success rate. Also, both methods using WB2 have significantly faster average convergence rates, with WB2+PF being the one with the lowest total average of iterations.

On the other hand, WB2 converges faster for higher numbers of initial samples, and it is the fastest method in the most number of sampling plans (7 against 5 of WB2+PF). Further, WB2+PF has the fragility of the possible inversion of the sign of the search function, that could be a problem for the problem defined in section 3.1, as the objective function for range variation will show relative improvements and the objective values are expected to be close to zero when reaching convergence, and may shift between positive and negative.

Overall, WB2 proved to be the most advantageous method out of the four tested, as well as the most adequate for the ongoing optimization problem. Nevertheless, depending on the initial samples and the shape of the surrogate model, WB2 is not always the best approach. Also, in some situations the convergence rate is much lower than average. For example, the results in table 3.5 for sampling

plan 2, exhibit a required number of 28 iterations to converge when using WB2, which is 360% higher than average. Aiming to improve this results, the optimization for this sampling plan was run again considering two methods for comparison, WB2 and WB2S (section 2.5.3) with a scaling factor  $s_f = 5$ .

From the observation of table 3.6, it can already be seen that WB2S was more effective than WB2, as the later was incapable of converging in the 50 maximum iterations. WB2S was also more efficient than the previous optimization with WB2 for the same sampling plan, reducing the number of iterations by 36%.

Table 3.6: Test optimization results for WB2 and WB2S, including an indication of convergence along with the number of iterations.

Sampling Plan [no. samples]	Minimum Pairwise Dist.	WB2		WB2S	
		Conv.	It	Conv.	It
2 [3]	0.4420	×	Max.It	✓	18

Figure 3.16 shows the eighteenth iteration for both methods, which is the last for WB2S. The predictions from the first ten iterations are very similar, with both methods selecting new samples in the lower right corner of the design space, where a local minimum is located. The scaling factor in WB2S enables the optimizer to jump out this region to explore the surrogate in less sampled regions with higher expected improvement, in particular, the valley close to the left-side of the boundary that includes the optimum. In contrast, WB2 persists locally exploiting around the local minimum, getting trapped there up to the fiftieth iteration (figure 3.17). The adaptation to WB2S showed an improvement in this situation.

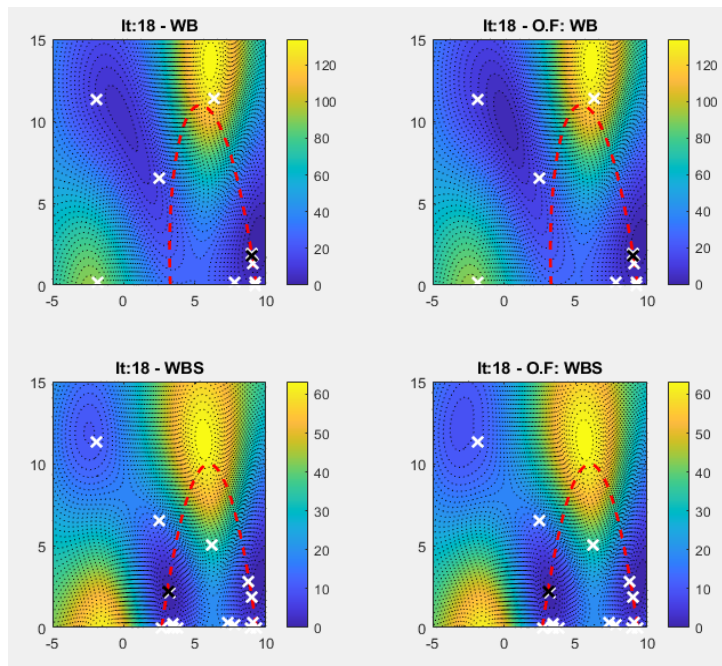


Figure 3.16: Eighteenth iteration prediction of sampling plan 2 with WB2 and WB2s methods.

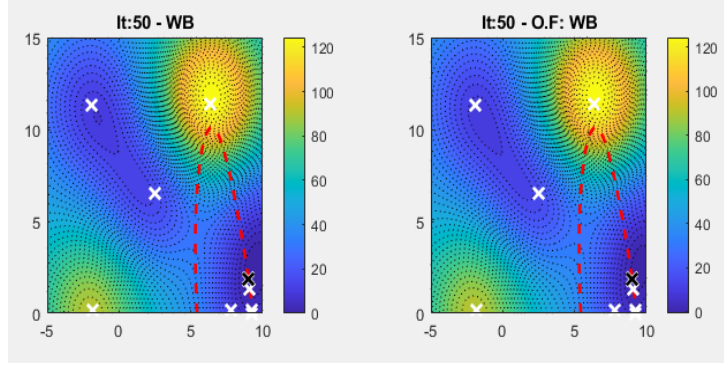


Figure 3.17: Fiftieth iteration prediction of sampling plan 2 with WB2 method.

### 3.3.2.2 Selection and implementation

Taking into account the comparison discussed above, eight search methods are considered for the optimization problem defined in 3.1.5, being these the EI, WB2, WB2S, prediction-based exploration ( $\hat{y}$ ), and all the previous with the implementation of PF. All the models are used at each iteration to define eight different search functions ( $f_S$ ). The following expressions were used to set up the search function for the different methods:

- EI:

$$f_{S_{EI}} = -A \frac{E[I(m_S)]}{m_{S_{ref}}} - B \frac{E[I(L/D)]}{(L/D)_{ref}}; \quad (3.12)$$

- WB2:

$$f_{S_{WB2}} = A \frac{\widehat{m_S} - m_{S_{ref}} - E[I(m_S)]}{m_{S_{ref}}} - B \frac{\widehat{(L/D)} - (L/D)_{ref} + E[I(L/D)]}{(L/D)_{ref}}; \quad (3.13)$$

- WB2S:

$$f_{S_{WB2S}} = A \frac{\widehat{m_S} - m_{S_{ref}} - 10 \times E[I(m_S)]}{m_{S_{ref}}} - B \frac{\widehat{(L/D)} - (L/D)_{ref} + 10 \times E[I(L/D)]}{(L/D)_{ref}}; \quad (3.14)$$

- $\hat{y}$ :

$$f_{S_{\hat{y}}} = A \frac{\widehat{m_S} - m_{S_{ref}}}{m_{S_{ref}}} - B \frac{\widehat{(L/D)} - (L/D)_{ref}}{(L/D)_{ref}}; \quad (3.15)$$

- EI+PF:

$$f_{S_{EI+PF}} = f_{S_{EI}} \times \sin \left( P[F(y)] \times \frac{\pi}{2} \right)^n; \quad (3.16)$$

- WB2+PF:

$$f_{S_{WB2+PF}} = \begin{cases} f_{S_{WB2}} \times \sin \left( P[F(y)] \times \frac{\pi}{2} \right)^n, & f_{S_{WB2}} < 0 \\ f_{S_{WB2}} \times (1.1 - \sin \left( P[F(y)] \times \frac{\pi}{2} \right)^n), & f_{S_{WB2}} \geq 0 \end{cases}; \quad (3.17)$$

- WB2S+PF:

$$f_{S_{WB2S+PF}} = \begin{cases} f_{S_{WB2S}} \times \sin \left( P[F(y)] \times \frac{\pi}{2} \right)^n, & f_{S_{WB2S}} < 0 \\ f_{S_{WB2S}} \times \left( 1.1 - \sin \left( P[F(y)] \times \frac{\pi}{2} \right)^n \right), & f_{S_{WB2S}} \geq 0 \end{cases} ; \quad (3.18)$$

- $\hat{y}$ +PF:

$$f_{S_{\hat{y}+PF}} = \begin{cases} f_{S_{\hat{y}}} \times \sin \left( P[F(y)] \times \frac{\pi}{2} \right)^n, & f_{S_{\hat{y}}} < 0 \\ f_{S_{\hat{y}}} \times \left( 1.1 - \sin \left( P[F(y)] \times \frac{\pi}{2} \right)^n \right), & f_{S_{\hat{y}}} \geq 0 \end{cases} ; \quad (3.19)$$

where,  $A = \ln \left( 1 + \frac{m_{S_{ref}}}{m_{f_{ref}}} \right) / \ln \left( \frac{m_i}{m_{f_{ref}}} \right)$  and  $B = 1$ .

The search is then performed by a GA. Once again, the MATLAB [132] 'ga' function is used for this purpose. The GA is set with a maximum number of 50 generations, a population size of 400 individuals and also, a function and constraint tolerances both of  $1 \times 10^{-8}$ . The initial population will correspond to all the feasible samples at each iteration.

All methods will generate one new potential sample point per iteration. The new point is then chosen by the author after an analysis based on a set of criteria and on experience.

The points originated from WB2 and WB2S have priority. The one with the best predictions for the objective function and/or higher uncertainty in the first iterations is selected. If both turn out to be structurally unfeasible, the previous criteria should be applied to the remaining methods. If none of the points is appropriate for evaluation or feasible, the points that had the structural mass and Tsai-Wu failure index calculated are added to update the two structural models and the optimization is reiterated.

### 3.3.3 Optimization Cycle

Each complete optimization iteration is performed according with the scheme displayed in figure 3.18. After everything is set up to start the optimization, the GA optimizer will provide 8 new samples together with their respective predictions, which are used to select the design point that should proceed to evaluation. The MDA is carried out as explained in section 3.2. Both structural and aerodynamic databases are then updated with the obtained results, which in turn allow to update the existing surrogate models. Finally, these models, along with the samples are supplied to the GA to generate new samples.

The cycle is repeated until either the outputs from the GA converge to an optimum or there is no more time available for further iterations. The last one being restricted by the deadline for the delivery of the master thesis.

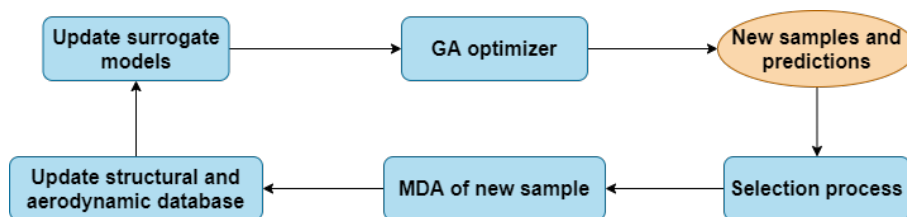


Figure 3.18: Optimization iteration cycle.



# Chapter 4

## Post-Processing

### 4.1 Discussion of Results

Before initiating the optimization, all 41 initial samples were evaluated, and number 5 was set as reference with the corresponding reference values:

- $m_{S_{ref}} = 9.731kg$ ;
- $m_{f_{ref}} = 19.462kg$ ;
- $(L/D)_{ref} = 13.6$ .

At each iteration of the optimization, during the evaluation of a new selected design point, the aerodynamic analysis is much more time-consuming, requiring approximately 8 hours to be completed versus 30 minutes, which is the approximate time required for the structural analysis. For this reason, it was decided to select multiple points per iteration to calculate  $m_S$  and the Tsai-Wu failure index, while only one of them would be fully evaluated. The CFD analysis of this last point runs in parallel with the structural analysis of the remaining points. This strategy aims to improve the approximation of the structural boundary allowing a more precise exploration and optimization within the feasible region.

Additionally, the computational resources available made it possible to run two CFD analyses at the same time in some occasions. When this was true, besides the configuration generated from the optimization algorithm, another one would be created by the author to run in parallel. The last would be based on the current best configurations with additional modifications towards a design with higher  $(L/D)$ , while maintaining the structural mass. The approach includes increasing the aspect ratio, changing the wing and canard incidences according with the AoA required for the trim condition and also adjusting the area ratio  $S_c/S_w$ . The insertion of these points to update the models was done with the objective of manually boosting the optimization.

Along the optimization, two cross-validation comparisons for the two regression models (constant and linear), identical to the one made before starting the optimization presented in section 3.3.1, were performed to adapt the models to better fit the samples and the design space.

The first was done after 37 iterations of structural evaluations of design points, of which only 12 proceeded to a CFD analysis. A total of 78 samples, for the two structural models were used for the cross-validation. Once again, there were not enough samples with a calculated  $(L/D)$  to build a model with a linear regression, as only 20 samples were available. The obtained errors are presented in table 4.1. This time, while a constant regression still provides smaller errors in the constraint model, the linear regression proved to be more precise for the mass prediction. Thus, a linear regression was implemented in the structural mass model from this iteration forward.

Table 4.1: Cross-validation results for the Tsai-Wu and structural mass models, with a constant and a linear regression.

Regression:	Tsai-Wu		Structural mass	
	Constant	Linear	Constant	Linear
$\bar{e}$	0.94	2.77	0.12	0.11
$e_{max}$	8.62	29.87	0.97	0.75

The last comparison of the regression models was done with an additional number of 120 and 15 samples, from the previous comparison, for the two structural and the  $(L/D)$  models, respectively. With a total of 35 aerodynamically evaluated samples, it was now possible to include the  $(L/D)$  model in the comparison. Table 4.2 displays the collected results of these cross-validations.

Table 4.2: Cross-validation results for the Tsai-Wu, structural mass and  $(L/D)$  models, with a constant and a linear regression.

Regression:	Tsai-Wu		Structural mass		$(L/D)$	
	Constant	Linear	Constant	Linear	Constant	Linear
$\bar{e}$	0.40	0.79	0.09	0.05	0.07	1.60
$e_{max}$	6.60	14.41	0.75	0.60	0.53	17.33

Regarding the structural models, the conclusion from the previous comparison is still verified, as the Tsai-Wu criterion is better approximated by a constant regression and the structural mass by a linear regression. For  $(L/D)$ , both the average and the maximum error are smaller for the constant regression, being this the one selected to continue using.

From the examination of the results from tables 3.4, 4.1 and 4.2, it can be seen that the bigger the number of samples used to build the surrogates, the more accurately approximated they are. The best average error for Tsai-wu and  $m_S$  decreased 68% and 75%, respectively, by adding 157 new samples. Additionally, it is verified that the difference in the errors between the constant and linear regressions also decreases with increasing number of samples. This is due to the approximation function having to interpolate all the samples, passing through all the points, meaning that the influence of the type of regression on the model accuracy decreases with the number of samples.

When comparing the two structural models, which both include all 37 design variables and always share the same samples for construction, the structural mass always shows better approximations than the Tsai-Wu model, indicating that the failure criterion is represented by a more complex function than

the structural mass. In contrast,  $(L/D)$  has small errors ( $\bar{\epsilon} = 7\%$ ), almost identical to  $m_S$  ( $\bar{\epsilon} = 5\%$ ), with significantly less samples for the model construction. This is due to the fact that the model of  $(L/D)$  has less dimensions than the structural models, as its construction is based on 27 design variables against the 37 used for the structural models.

Figures 4.1, 4.2, 4.3, plot the evolution along the optimization of  $m_S$ , the  $(L/D)$  ratio and the Tsai-Wu failure index, respectively. Only samples corresponding to iterations with complete aero-structural evaluations are displayed. The initial samples are represented in black on the negative side of the horizontal axis, green points correspond to samples generated by the optimization and blue points to the manually modified configurations introduced by the author.

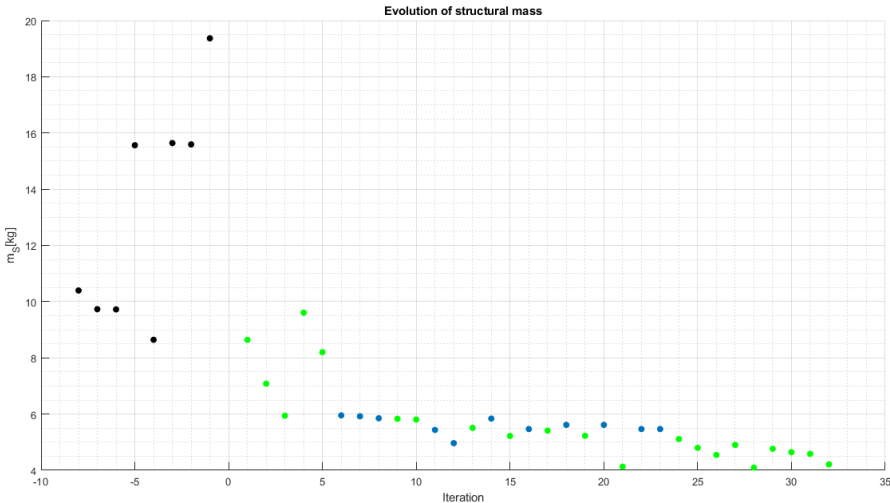


Figure 4.1: Evolution of  $m_S$  along the optimization.

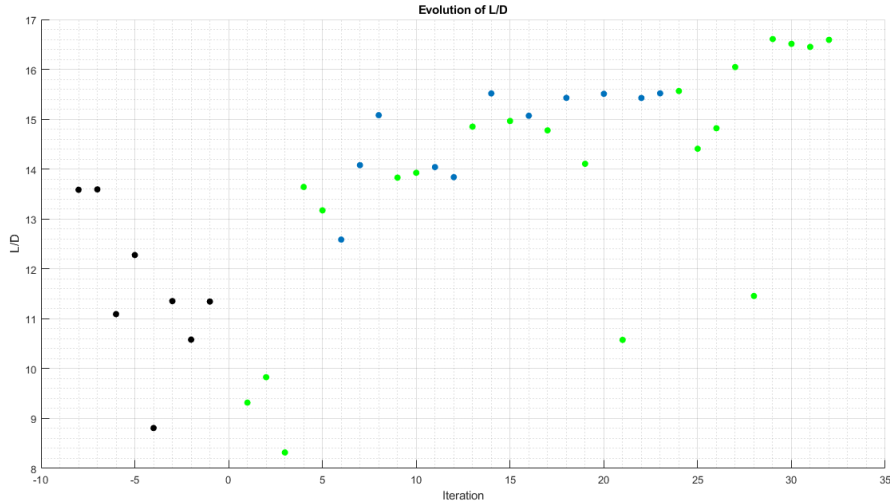


Figure 4.2: Evolution of  $(L/D)$  along the optimization.

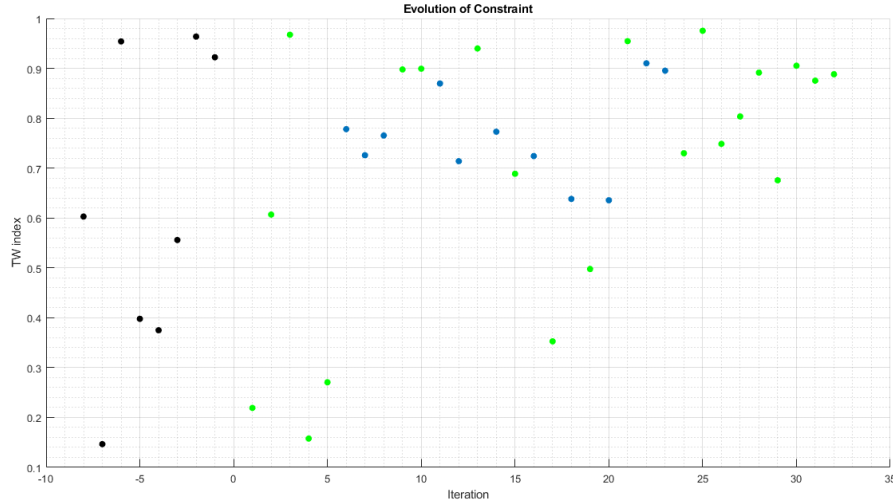


Figure 4.3: Evolution of the Tsai-Wu failure index along the optimization.

Besides 8 of the initial samples, a total of 32 new design points were fully evaluated, of which 11 were introduced by the author. These 40 samples represented on the plots correspond to 14.5% of the 276 configurations that went through structural analysis.

In the first 6 complete iterations a major decrease in the structural mass was verified,  $m_S$  permanently dropped below  $6kg$ , which is a reduction of more than 38% from the initial reference. At this stage, a total of 13 new samples were added to the structural models.

Differently, the  $(L/D)$  declines in the first 3 complete iterations, in comparison with the initial  $(L/D)_{ref}$ . In the subsequent iterations, the  $(L/D)$  trend increased gradually until it reached its optimum value at the end of the optimization.

Beyond the sixth complete iteration, the decrease in  $m_S$  became less significant between iterations. Further, the structural mass is predicted with more precision than the Tsai-Wu failure index, like previously noticed from tables 4.1 and 4.2, resulting in a high uncertainty in the constraint model, and thus an unreliable structural boundary. For this reason, many of the generated samples were unfeasible, particularly, from 57 selected and structurally analyzed samples, only 14 turned out to be feasible, which corresponds to only 25%.

At this stage of the optimization, due to the low percentage of feasibility from the selected design points, as well as to the fact that the wingbox structure showed almost no change between the 57 added samples, it was decided to sweep the structural design variables of the wing in order to identify their influence on the structural models, and also to improve the prediction of the Tsai-Wu boundary. Seven design variables were used for this approach,  $pos_{fspar}$ ,  $thk_{tip_{spar}}$ ,  $thk_{disc_{spar}}$ ,  $thk_{root_{spar}}$ ,  $thk_{tip_{skin}}$ ,  $thk_{disc_{skin}}$  and  $thk_{root_{skin}}$ . Each variable was selected and varied between the lower and upper bounds, non-dimensionally from zero to one, with a step of 0.1, while keeping the remaining 36 variables fixed (equal to the current best). This led to the generation of 11 configurations per design variable, thus a total of 77 configurations. Additionally, two more configurations were considered, one with all seven variables at the lower bound, and the other at the upper bound.

After performing the structural analysis on all 79 generated configurations, the uncertainty on the constraint model, measured by the averaged mean squared error (MSE) of all the predictions, decreased 34%, from 5.292 to 3.487.

Unlike the behavior of the  $(L/D)$  and  $m_S$  models, the evolution of the Tsai-Wu index values is less consistent, which was anticipated as the Tsai-Wu model demonstrates higher uncertainty and complexity. Nevertheless, a tendency to obtain higher indexes closer to one is verified, as most points after iteration 20 have the index value above 0.7, meaning that the optimization is evolving around the structural boundary as the structural mass decreases.

Figures 4.4 and 4.5 plot the evolution along the optimization of the objective function  $\Delta R$  and the ratio  $R/R_{ref_0}$ , respectively, where  $R_{ref_0}$  is the range of the initial reference configuration. The color scheme used to represent the design points at each iteration corresponds to the one applied in figures 4.1, 4.2 and 4.3.

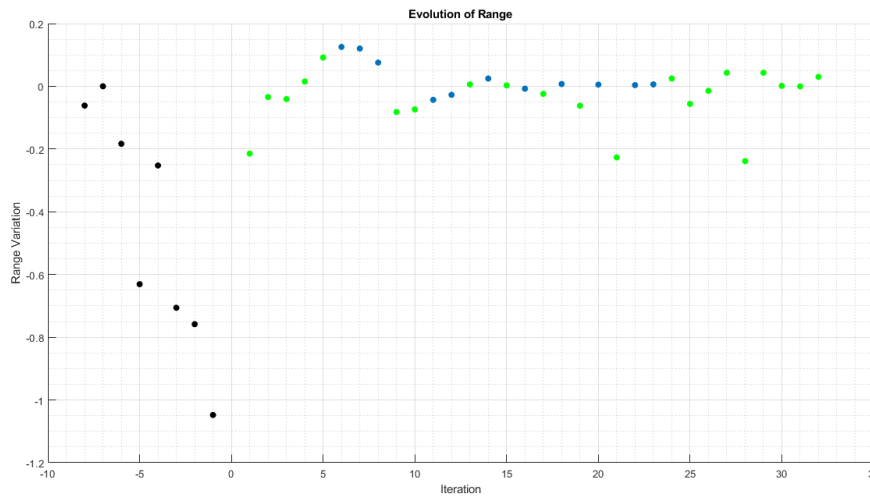


Figure 4.4: Evolution of the objective function along the optimization.

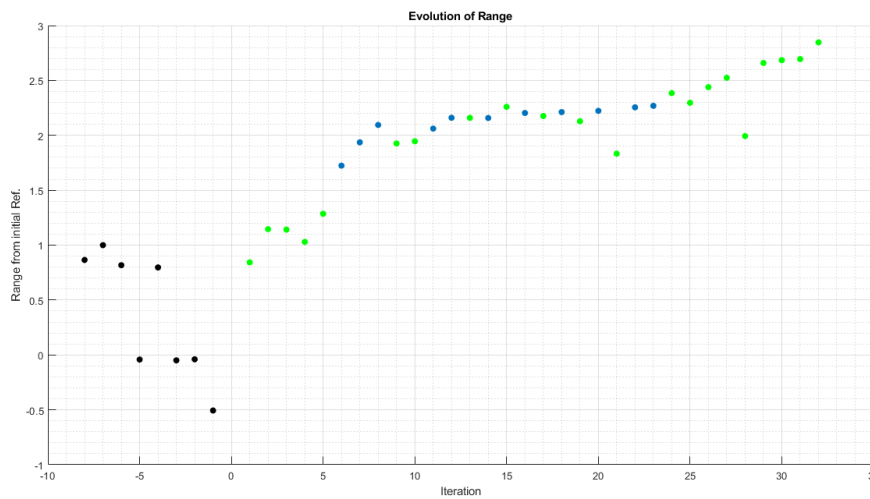


Figure 4.5: Evolution of range ratio,  $R/R_{ref_0}$  along the optimization.

Figures 4.4 and 4.5 allow the verification that range is increasing along the optimization and starts converging with  $\Delta R$  tending to zero with the number of iterations. Similarly to the  $(L/D)$ , the author's predictions represent most of the greater improvements in range, as  $(L/D)$  has a higher influence on range than  $m_S$ . This is due to the fact of the weight of the mass component in the objective function,  $-\ln\left(1 + \frac{m_{S_{ref}}}{m_{f_{ref}}}\right) / \ln\left(\frac{m_i}{m_{f_{ref}}}\right)$ , decreasing its magnitude with the reduction of  $m_S$ , having an initial magnitude of 0.8911, smaller than the weight of the  $(L/D)$  component in the objective function, which is constant and equal to 1.

It is also observed that once the structural models were updated with the design points from the sweeping of the structural variables, i.e., from iteration 24 forward, it was possible to almost double the increase in range at iteration 27, after two iterations to better estimate  $(L/D)$ . The enhanced focus of the optimizer on  $(L/D)$  was due to the significant improvement of the structural predictions.

The optimal configuration developed in such way to increase the aspect ratio of both wing and canard, in particular, the average aspect ratios of the first 10 iterations are 11.28 and 15.35, while for the last 10 iterations are 13.33 and 18.98, for the two lifting surfaces, respectively. It is also verified that the AoA is gradually smaller in magnitude, as the optimization adapts the incidence and twist angles of the wing, and along with  $i_c$ , tries to trim the aircraft aligned with the flow, thus reducing the fuselage drag for the same trimmed lift, as the aircraft mass is always equal to 25kg. Consequently,  $(L/D)$  and range increase.

Structurally, the component which had the highest Tsai-Wu failure index in almost all iterations was the fuselage spar in the region of the connection with the canard tube. A possible approach to improve this feature could be to strengthen the fuselage spar laminate in the region around the canard, allowing the rest of the spar to be thinner, thus significantly decreasing the structural mass.

The optimization was stopped after iteration 32 because the time limit was reached. Nevertheless, it can be considered approximately converged as in the last 5 iterations that had an improvement in range, the relative variation of range (objective function) is always smaller than 5%. However, the last iteration showed an improvement of 3%, whereas the previous improvement was only of 0.1%, meaning that the result could have achieved further convergence if more time was available.

It cannot be verified if the exploited optimum region corresponds to a local or a global optimum. Moreover, the existence of designs with negative objective values in the latter iterations indicate that the optimizer is not being able to easily find better predictions than the ones already existing samples, meaning that the current optimum is located in a valley of the design space.

Figure 4.6 displays the final population of the solved problem, with the horizontal and vertical axes corresponding to  $m_S$  and  $(L/D)$ , respectively.

The final population shows that 21 points, which correspond to 66% of the new fully-evaluated samples, are inside a good feasible region with the structural mass between 4 and 6 kilograms, and the  $(L/D)$  between 14 and 17.

Additionally, the optimization seems to be developing towards a utopia point, in the top left corner of figure 4.6, with  $m_S = 4kg$  and  $(L/D) = 17$ , although this point might not be possible to reach.

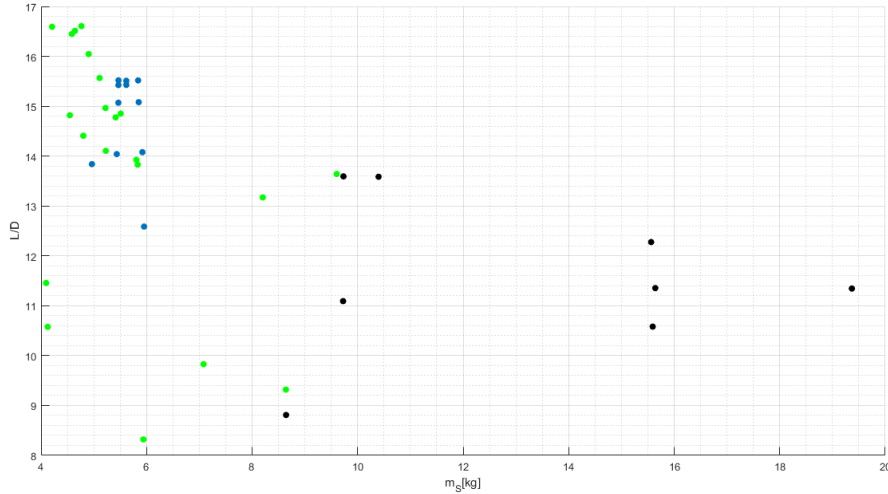


Figure 4.6: Final population.

## 4.2 Characterization and validation of final design

The achieved optimum design point at the end of the optimization has the following outputs:

- $m_S = 4.209kg$ ;
- $m_f = 13.940kg$ ;
- $(L/D) = 16.6$ ;
- $R/R_{ref_0} = 2.85$ .

The final design represents a reduction of 56.7% in the structural mass, which corresponds to 16.84% of the MTOM, along with an increase of 22.1% in the lift to drag ratio, from the initial reference sample, resulting in a range almost three times larger than  $R_{ref_0}$  in cruise. The trim conditions in cruise obtained from the CFD analysis were verified for a combination of an angle of attack  $\alpha_{trim}$  and a canard incidence angle  $i_{c_{trim}}$  equal to 1.6 and 1.3 degrees, respectively. Additionally, an identical analysis was carried out considering dash instead of cruise, resulting in a  $(L/D)$  of 7.9 for a trimmed aircraft at  $\alpha_{trim} = -1.9^\circ$  and  $i_{c_{trim}} = 0.9^\circ$ .

The CoG of the aircraft is located in front of the wing, at a longitudinal distance of  $l_w = 0.338m$  to the wing aerodynamic center. This position was obtained from the trim and longitudinal stability conditions.

This configuration is a product of the combination of the values of the design variables presented in table 4.3.

The resulting structure and outer shape are represented on figures 4.7 and 4.8, respectively. Additionally, figure 4.9 depicts the three main dimensions of the aircraft in meters.

Table 4.3: Values of the design variables for the final design.

Variable	Value	Variable	Value
$y_{scale}$ [ ]	1.00	$\gamma_{w_{tip}}$ [deg]	0.7897
$z_{scale}$ [ ]	1.00	$y_{\gamma_{disc}}$ [m]	$0.4681b_w/2$
$thk_{fuse}$ [m]	0.02	$\Lambda_w$ [deg]	2.4389
$r_{tube}$ [m]	0.0056	$t_w$ [ ]	0.1261
$thk_{tube}$ [m]	0.0049	$cbr_w$ [ ]	0.0177
$pos_{fspar}$ [m]	$0.2078c(y)$	$b_{wght}$ [m]	0.0949
$thk_{tip_{spar}}$ [m]	$1.3 \times 10^{-3}$	$\lambda_{wght}$ [ ]	0.2025
$thk_{disc_{spar}}$ [m]	$2.0 \times 10^{-3}$	$\Lambda_{wght}$ [deg]	22.5907
$thk_{root_{spar}}$ [m]	$1.0 \times 10^{-3}$	$t_{wght}$ [ ]	0.1081
$thk_{tip_{skin}}$ [m]	$9.2513 \times 10^{-4}$	$cbr_{wght}$ [ ]	0.0078
$thk_{disc_{skin}}$ [m]	$9.5602 \times 10^{-4}$	$b_c$ [m]	1.2994
$thk_{root_{skin}}$ [m]	$6.7512 \times 10^{-4}$	$S_c$ [m <sup>2</sup> ]	$0.1580S_w$
$b_w$ [m]	2.7384	$l_c$ [m]	1.5002
$c_{root_w}$ [m]	0.3977	$z_c$ [m]	0.0204
$c_{disc_w}$ [m]	0.1570	$cbr_c$ [ ]	0.0593
$c_{tip_w}$ [m]	0.1314	$c_{root_f}$ [m]	0.2
$y_{c_{disc}}$ [m]	$0.4649b_w/2$	$\lambda_f$ [m]	0.5657
$\gamma_{w_{root}}$ [deg]	2.2912	$b_f$ [m]	0.3387
$\gamma_{w_{disc}}$ [deg]	2.2890		

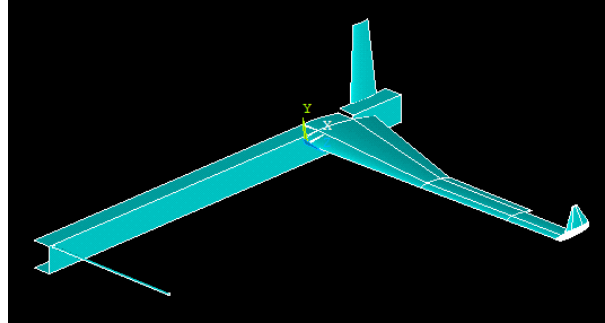


Figure 4.7: Representation of the structure of the final configuration.

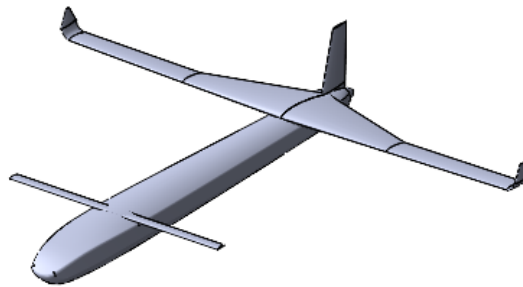


Figure 4.8: Representation of the outer shape of the final configuration.

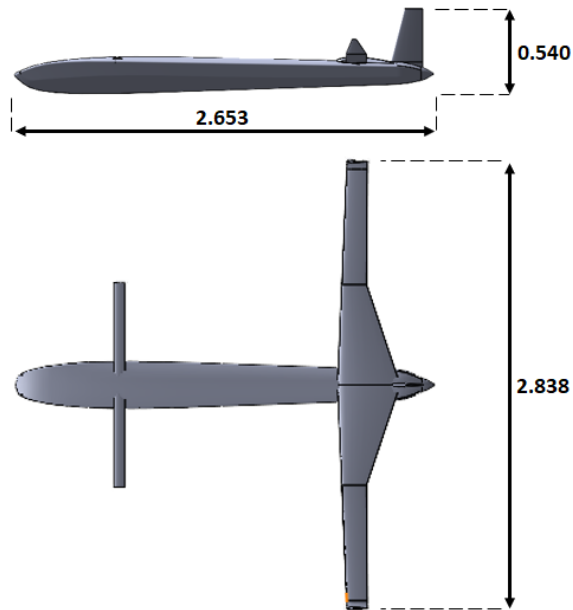


Figure 4.9: Aircraft dimensions.

It is possible to see that the two variables corresponding to the fuselage scale in the two transverse directions of the fuselage converged to the minimum value allowed, generating a slender fuselage in order to reduce the negative contribution of the fuselage drag to the  $(L/D)$ . These dimensions guarantee that the fuselage is just wide enough to fit the MAD sensor inside.

The fin dimensions are almost at the upper bounds set for the variables, increasing the area of the fin, therefore reducing its distance to the CoG, for a constant  $C_{VT}$ . This way, the fin is placed at the trailing edge of the wing. This combined with the value of  $l_c$ , that also converged to the minimum, leads to a short fuselage, reducing its surface area and consequently the fuselage drag.

The chord and twist discontinuities of the wing are almost coincident, and the wing displays a washout almost only after the discontinuity.

In addition, the wing presents an aspect ratio of 13.16. On the other hand, the aspect ratio of the canard is much higher, with a value of 18.75. The canard is placed at a high position, at the top of the fuselage. Moreover, figures 4.10 and 4.11 illustrate the stream lines around the aircraft and the pressure distribution on the surface, as well as on the symmetry plane of the aircraft, respectively. It is possible to see from the stream lines that the stream generated by the canard hits the wing directly. As a consequence, the surface of the wing covered by the canard stream suffers a downwash, unloading the wing surface, identified by the lower pressure in the leading edge of the wing after the discontinuity (dark blue region in the wing displayed in figure 4.11), in comparison with the pressure at the leading edge closer to the root. A possible approach to this problem would be to lower the canard, so it would not interfere with the airflow around the wing, allowing for more lift to be generated closer to the root, thus approximating the lift distribution to an elliptical shape and increasing  $(L/D)$ .

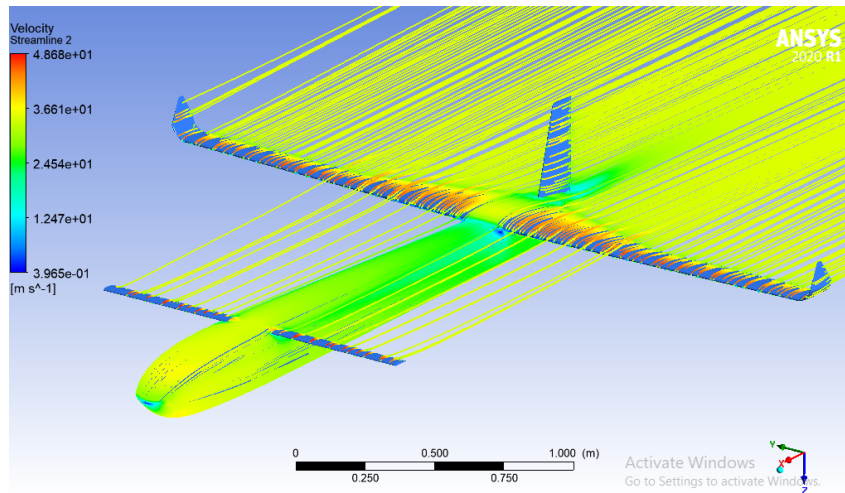


Figure 4.10: Stream lines around the aircraft.

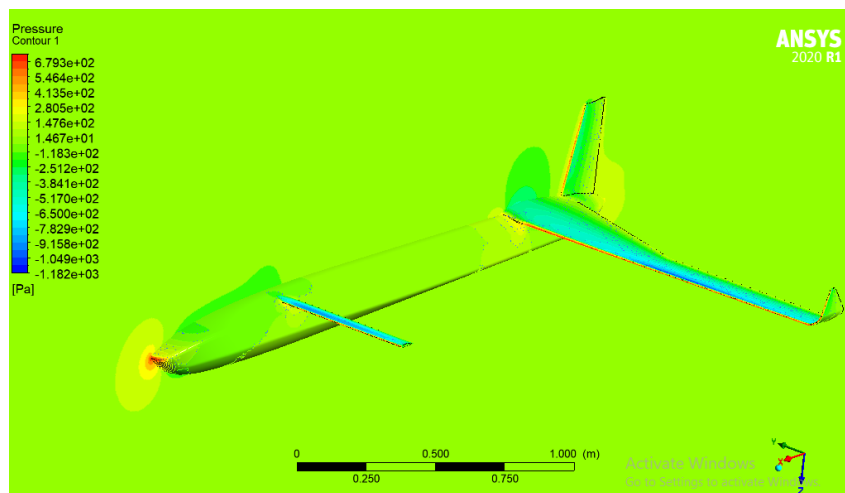


Figure 4.11: Pressure distribution on the surface and on the symmetry plane of the aircraft.

Still regarding the shape of the final configuration, the winglets have considerable dimensions as its defining variables are not set at the minimum allowed values, indicating that their influence is beneficial to the overall performance of the aircraft.

Further, the maximum Tsai-Wu failure index is close to one, as a result of the structural component of the optimization to reduce mass. Figure 4.12 shows the value of the Tsai-Wu failure index for all elements of the structure, while figures 4.13 (a) and (b) display the two most critical regions, in particular, the connection between the canard and the fuselage spar, and the wing root. The region of the fuselage spar supporting the canard tube was once again the element with the highest Tsai-Wu failure index with a value of 0.89. The upper surface of the canard tube also shows high failure index values closer to the root, in comparison with the rest of the structure. The wing skin also stands out from the rest of the structural components for displaying failure index values around 0.3 and 0.4 closer to the root, in particular near the front spar, while most of the structure exhibits an average value lower than 0.1.

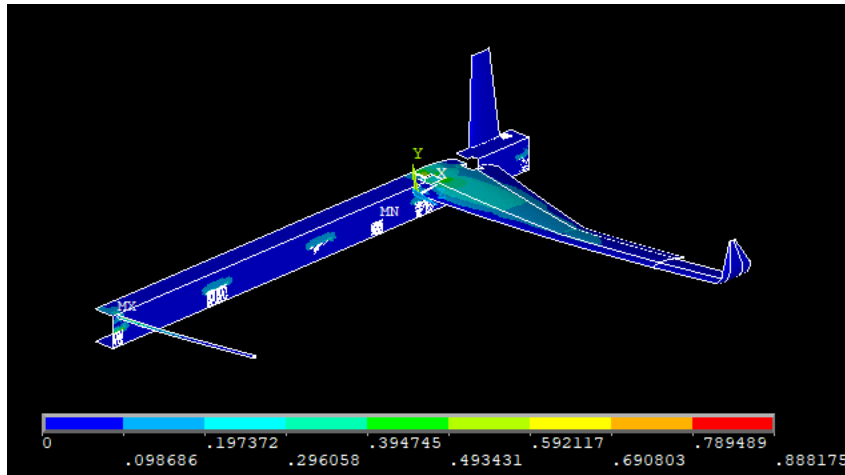
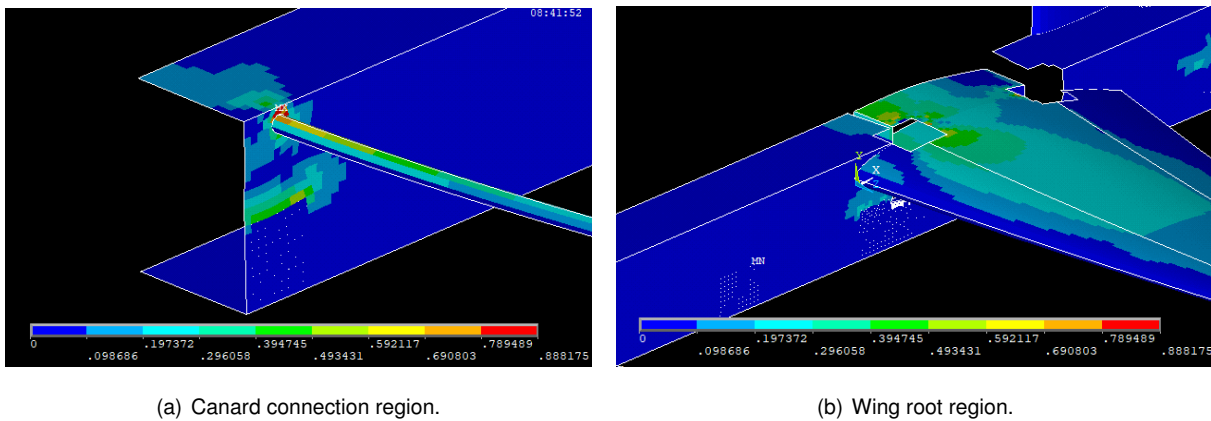


Figure 4.12: Tsai-Wu failure index values on entire structure.



(a) Canard connection region.

(b) Wing root region.

Figure 4.13: Tsai-Wu failure index values on critical regions.

Taking into account the thickness distributions defined by the obtained values for the structural design variables, the total number of layers and stacking sequence of each component translates in the following characterization for the different components.

The fuselage spar is composed by 10 woven carbon layers, which is the minimum imposed, indicating that it could possibly still be reduced while maintaining integrity.

The canard tube has a total of 30 UD carbon layers, in comparison with the imposed minimum of 6. Taking into account the large tube thickness obtained for a small canard, an alternative structure for this surface should be considered. For example, include a carbon fiber skin, similar to the wing skin, capable of bearing part of the aerodynamic loads and allowing a thinner tube.

Regarding the wingbox, both skin and spars are thinner at the root, with both these thicknesses being at the lower bound of the variables. The bigger thickness of both these components is at the discontinuity of the thickness distributions, which is located at 46.5% of the half span. Figures 4.14 and 4.15 show the distribution of the number of layers along half span, as well as the stacking sequence, for the wingbox skin and spars, respectively.

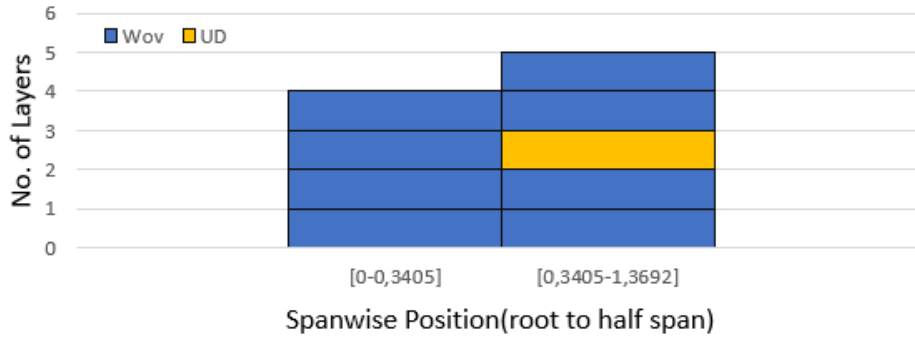


Figure 4.14: Distribution of the number of layers of wingbox skin along half span.

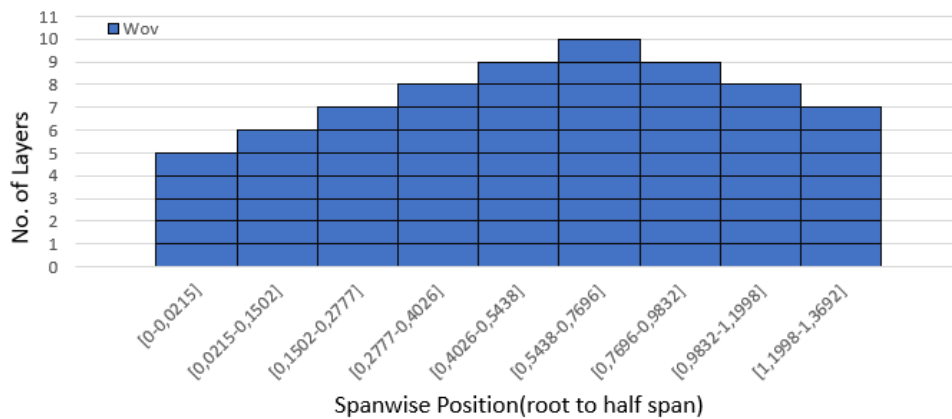


Figure 4.15: Distribution of the number of layers of wingbox spars along half span.

This thickness distribution is possibly due to the fact that the wing section is larger close to the root, which translates in a higher inertia, thus the required thickness is smaller. Contrarily, from the discontinuity to the tip the thickness is greater as a result of a smaller wing section.

#### 4.2.1 Computational Validation

To further validate the obtained design, two additional analyses were performed, one CFD analysis to obtain a detailed aerodynamic characterization of the aircraft, and a modal analysis on the structure to identify the vibration modes.

The CFD analysis was conducted in ANSYS CFX [109] like the previous ones. A total of 12 simulations with different AoA varying between -5 and 15 degrees, besides the one that trimmed the aircraft, were considered. With the gathered data it was possible to plot the curves of  $C_L vs. \alpha$  (figure 4.16),  $C_D vs. \alpha$  (figure 4.17),  $C_m vs. \alpha$  (figure 4.18), the drag polar  $C_D vs. C_L$  (figure 4.19) and also  $(L/D) vs. C_L$  (figure 4.20).

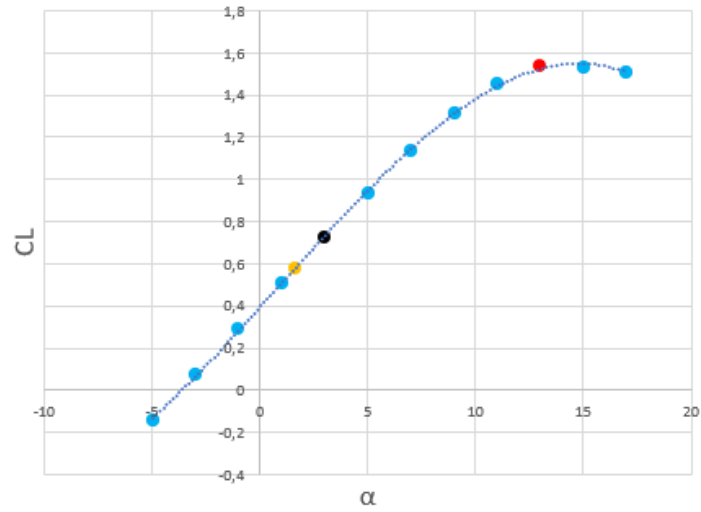


Figure 4.16:  $C_L$  vs.  $\alpha$  curve for final configuration.

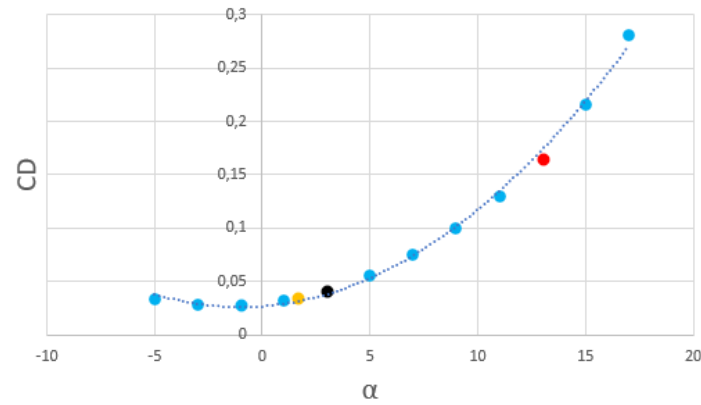


Figure 4.17:  $C_D$  vs.  $\alpha$  curve for final configuration.

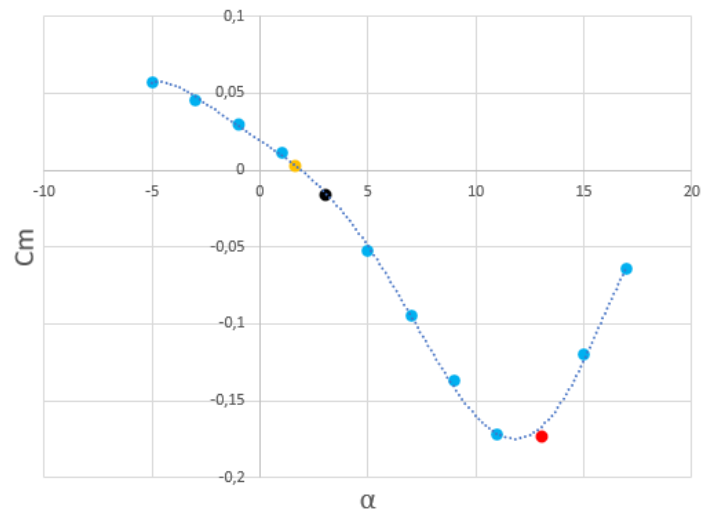


Figure 4.18:  $C_m$  vs.  $\alpha$  curve for final configuration.

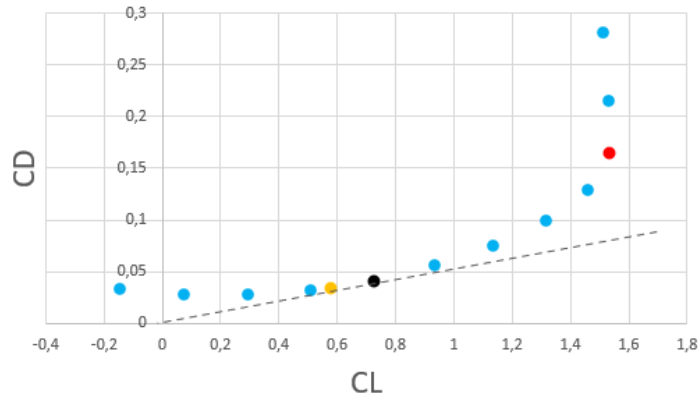


Figure 4.19: Drag polar for the final configuration.

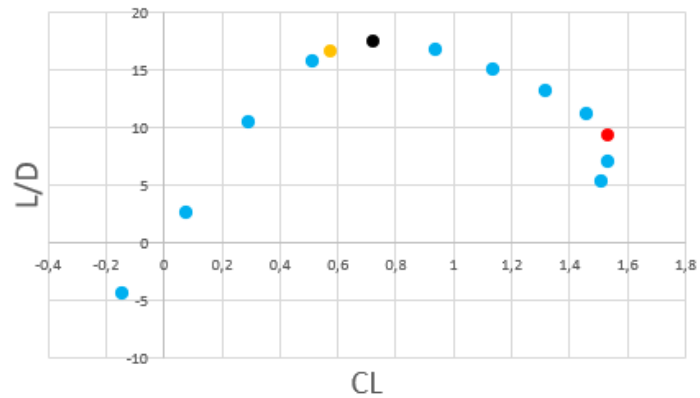


Figure 4.20:  $(L/D)$  vs.  $C_L$  curve for final configuration.

The trim condition mentioned above is represented by the yellow points on the plots.

Figures 4.19 and 4.20 allow to identify the point of higher  $(L/D)$ , marked in black. The maximum value observed for  $(L/D)$  is 17.39, which is 5% higher than the value obtained for the trim condition. It is verified for  $C_L = 0.724$  at an AoA of 3 degrees, which is a higher lift coefficient than  $C_{L_{trim}}$ . If  $V_{cr}$  was reduced, this configuration could be trimmed for the maximum  $(L/D)$ , as  $C_{L_{trim}}$  would increase. However, cruise speed cannot be reduced due to the mission requirements.

The value of the drag coefficient for  $C_L = 0$  can be determined from the plot on figure 4.19 and it is approximately  $C_{D0} = 0.029$ , which is higher than expected. Additionally, the drag coefficients of the wing, canard and fuselage were plotted separately in figure 4.21 in order to determine the influence of each component (orange, yellow and grey curves, respectively). The largest contribution to the drag is from the wing, as for the same condition of zero lift, it has an estimated  $C_{D0_w} = 0.012$ . Part of the verified high wing drag may be due to the interference of the canard air streams. Also, the fuselage exhibits a value of 0.011 for  $C_{D0_{fuse}}$ , being almost identical to  $C_{D0_w}$  for the condition of zero lift. The canard presents a  $C_{D0_c}$  of approximately 0.0056, which is also a high value considering the small size of the canard. Further, comparing the curves for the canard and for the fuselage in their whole extension for multiple AoA, it is possible to see that they are almost coincident. One of the causes of the canard

drag is its large camber on the airfoil, with a value of 5.9%.

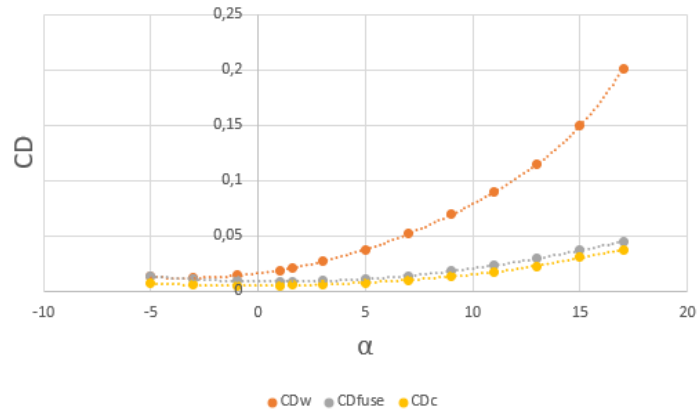


Figure 4.21:  $C_D vs. \alpha$  curves the wing, canard and fuselage of the final configuration.

Figure 4.16 shows that the maximum value for the lift coefficient,  $C_{L_{max}} = 1.533$ , was obtained for an angle of attack of  $\alpha = 13^\circ$  (identified by the red markers on the plots), meaning that this angle can possibly correspond to the stall angle. In turn, trimming the aircraft at  $C_{L_{max}}$  would translate to a stall speed of  $21.5m/s$ . However, a CFD analysis aiming to trim the aircraft with  $C_{L_{max}}$  proved that it is not possible to cancel the pitching moment as the canard cannot compensate the negative contribution of the wing to the pitching moment.

Further, four additional angles of attack around  $\alpha = 13^\circ$  were included in the simulations in order to plot the  $C_L vs. \alpha$  curves for both the wing and canard shown in figure 4.22, and clearly identify which lifting surface stalls first. The lifting coefficient of the canard  $C_{L_c}$  (orange curve) is always higher than the one of the wing,  $C_{L_w}$  (blue curve). Also, the canard enters stall at an angle of attack of  $12^\circ$  with  $C_{L_{c_{max}}} = 1.327$ , while for the wing this condition is only reached at an angle of attack of  $13.5^\circ$  and  $C_{L_{w_{max}}} = 1.204$ , thus confirming the requirement which imposes that the canard must stall before the wing, presented on section 3.1.1.

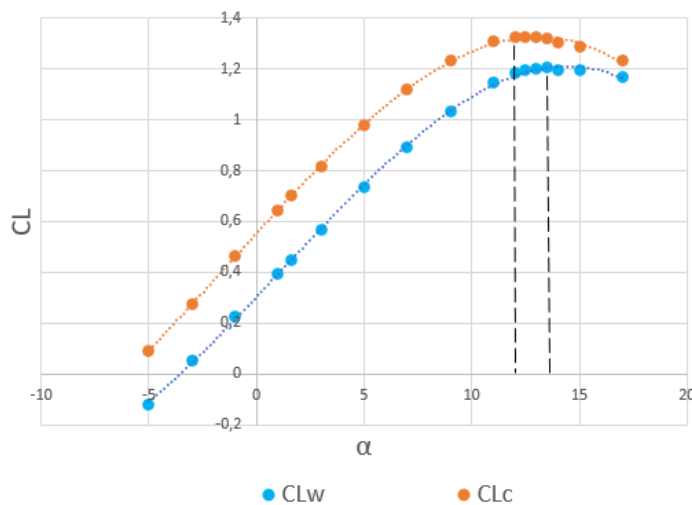


Figure 4.22:  $C_L vs. \alpha$  curves for the two lifting surfaces of the final configuration.

Knowing that stall is verified first on the canard, an estimation of the stall speed was determined by trimming the aircraft with  $C_{L_c} = C_{L_{c_{max}}}$  and considering only the pitching moment generated by the lifting forces. The system of equations 4.1 describes this trim condition:

$$\begin{cases} M = 0 \\ L_c + L_w = m_i g \end{cases} \Leftrightarrow \begin{cases} S_c C_{L_{c_{max}}} (l_c - l_w) - S_w C_{L_w} l_w = 0 \\ \frac{1}{2} \rho V_{stall}^2 (S_c C_{L_{c_{max}}} + S_w C_{L_w}) = m_i g \end{cases} . \quad (4.1)$$

Solving equation 4.1 for  $V_{stall}$  and  $C_{L_w}$ , the values of  $27.61m/s$  and  $0.72$  are obtained for the two variables, respectively. The corresponding stall angle is then obtain by interpolating the trending line that better fits the  $C_{L_w}$  curve in figure 4.22 at  $C_{L_w} = 0.72$ , which resulted in  $\alpha_{stall} = 4.746^\circ$ . The incidence of the canard can also be estimated. Knowing that  $C_{L_{c_{max}}}$  was verified for  $\alpha = 12^\circ$  with an incidence of the canard of  $i_{c_{trim}} = 1.316^\circ$ , thus a total canard angle of attack of  $\alpha_c = 12 + 1.316 = 13.316^\circ$ , the incidence of the canard for the obtained stall condition is then given by  $i_c = \alpha_c - \alpha_{stall} = 8.57^\circ$ . The estimated  $V_{stall}$  is 28.4% higher than the initial prediction of  $21.5m/s$ , which in turn is 7.5% higher than the desired  $V_{stall}$  of  $20m/s$ . The stall condition could be improved by increasing the area of the canard, as it corresponds to only 15.8% of  $S_w$ , which is almost at the lower bound of the variable. A bigger  $S_c$  would allow to trim the aircraft at a higher  $C_{L_w}$ , thus reducing the stall speed.

The modal analysis was performed in ANSYS Mechanical APDL [102], using the same structural model and boundary conditions as before. The first ten mode shapes were identified and registered in table 4.4. The axes  $X$ ,  $Y$  and  $Z$  indicated in table 4.4, correspond to the directions of the roll, pitch and yaw axes of the aircraft respectively. Figures 4.23 to 4.42 display the deformation of the aircraft for each of the identified modes.

Table 4.4: Vibration modes and respective frequencies.

Frequency[Hz]	Mode	Location
12.863	Bending $Z$	Wing
21.389	Bending $Z + X$	Canard
21.470	Bending $X + Z$	Canard
22.958	Bending $Z + X$	Canard
27.387	Bending $X$	Fin
43.023	Bending $Z$	Wing
61.991	Bending $X$	Wing
75.561	Bending $Z$	Fuselage
91.112	Torsion $Y$	Wing
109.74	1)Torsion $Y$	1)Wing
	2)Bending $X$	2)Fin

The first identified mode (figures 4.23 and 4.24) is obtained for a frequency of 12.863Hz and it corresponds to a bending of the wing in the  $Z$  direction.

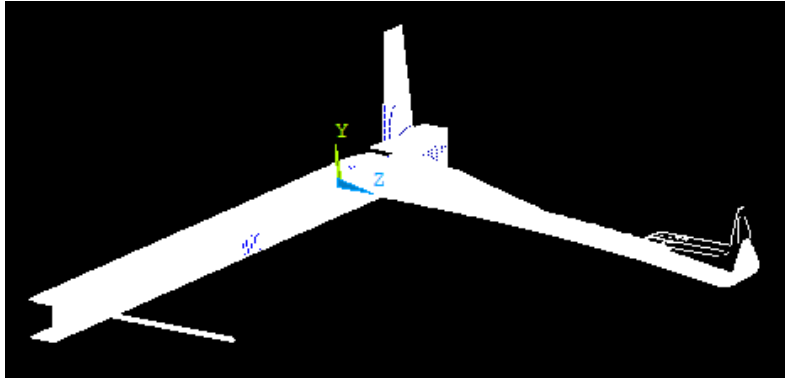


Figure 4.23: Mode shape 1 general aircraft deformation and undeformed aircraft contours.

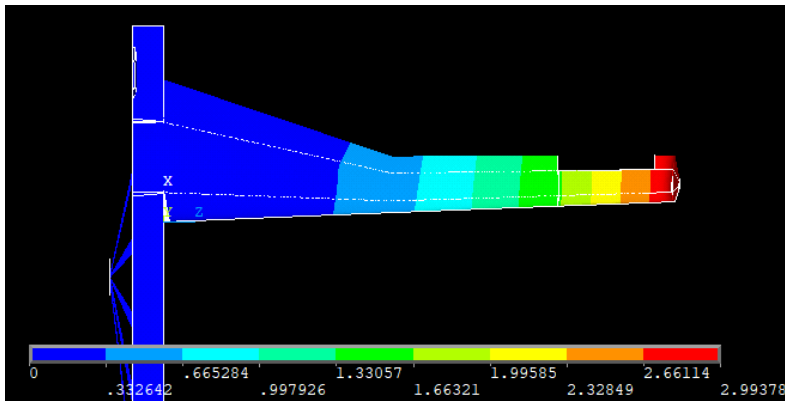


Figure 4.24: Mode shape 1 total deformation on critical region.

The next three natural frequencies are related to the bending of the canard in both  $X$  and  $Z$  directions (figures 4.25 to 4.30). At the frequencies of 21.389Hz and 22.958Hz, the bending is more noticeable in the  $Z$  direction, while for a vibration of 21.470Hz, the bending in  $X$  is more intense.

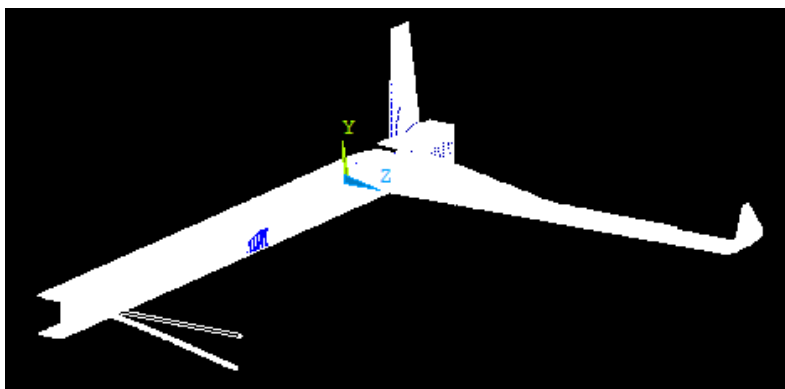


Figure 4.25: Mode shape 2 general aircraft deformation and undeformed aircraft contours.

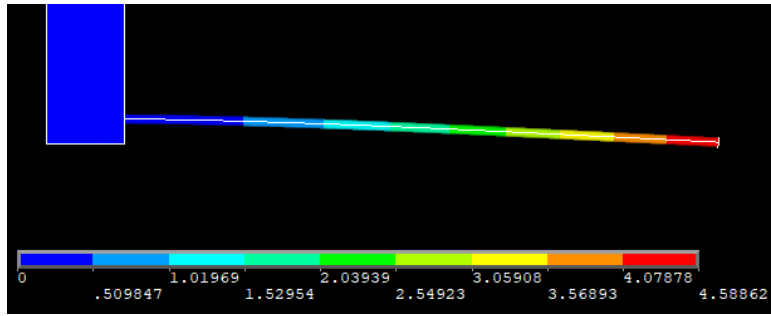


Figure 4.26: Mode shape 2 total deformation on critical region.

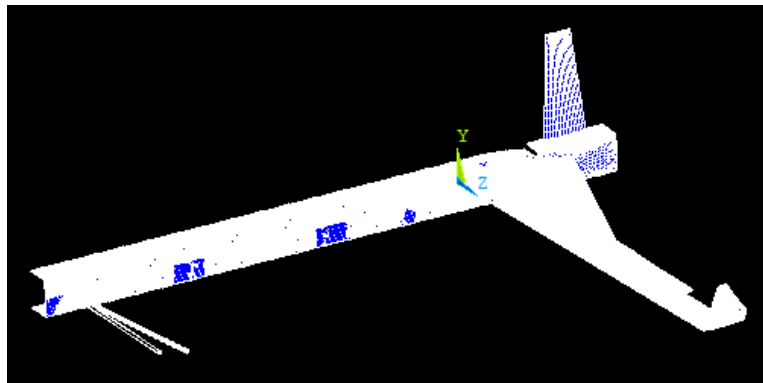


Figure 4.27: Mode shape 3 general aircraft deformation and undeformed aircraft contours.

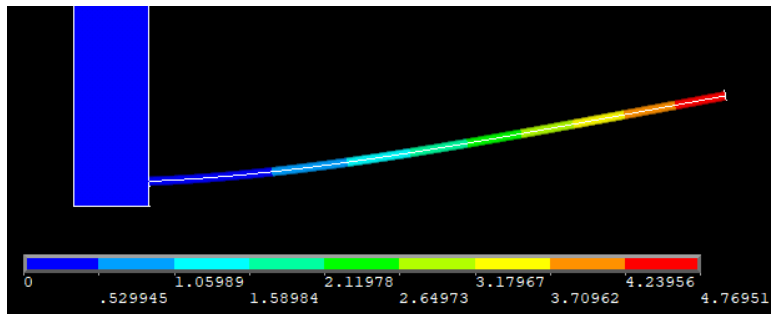


Figure 4.28: Mode shape 3 total deformation on critical region.

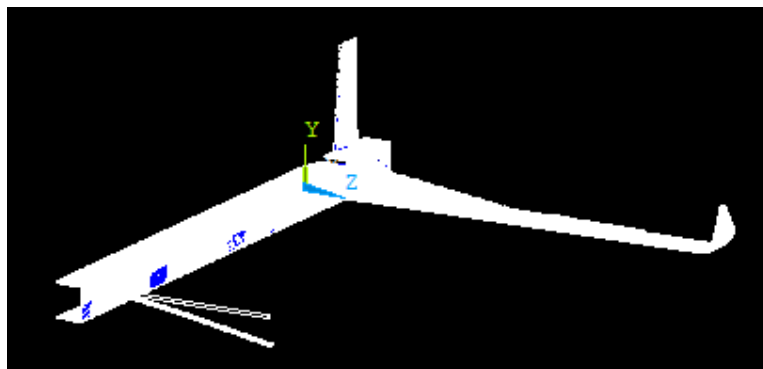


Figure 4.29: Mode shape 4 general aircraft deformation and undeformed aircraft contours.

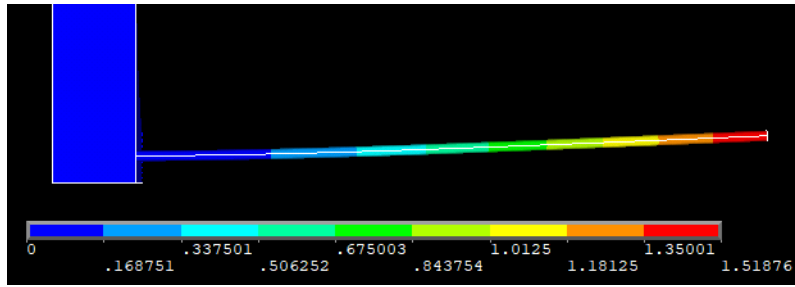


Figure 4.30: Mode shape 4 total deformation on critical region.

At a vibration frequency of 27.387Hz, the fin displays its first mode shape corresponding to a bending in  $X$  (figures 4.31 and 4.32).

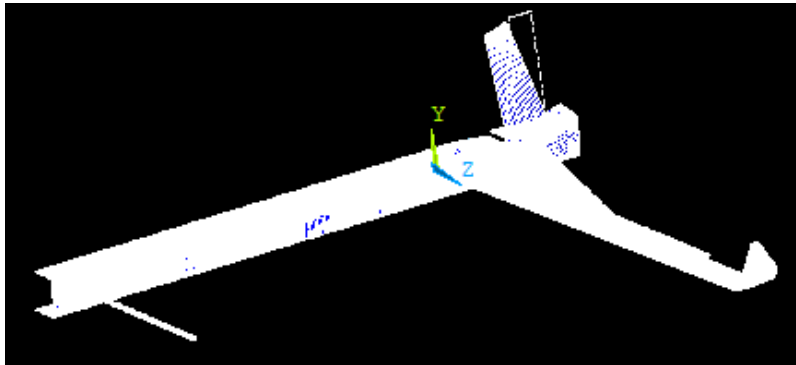


Figure 4.31: Mode shape 5 general aircraft deformation and undeformed aircraft contours.

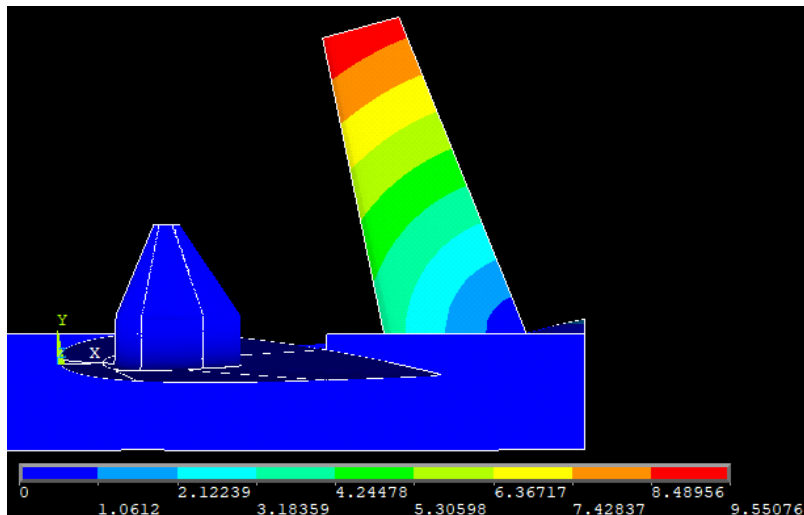


Figure 4.32: Mode shape 5 total deformation on critical region.

Both the sixth and seventh vibration modes occur on the wing, for bending in  $Z$  and  $X$  directions and frequencies of 43.023Hz and 61.991Hz, respectively (figures 4.33 to 4.36).

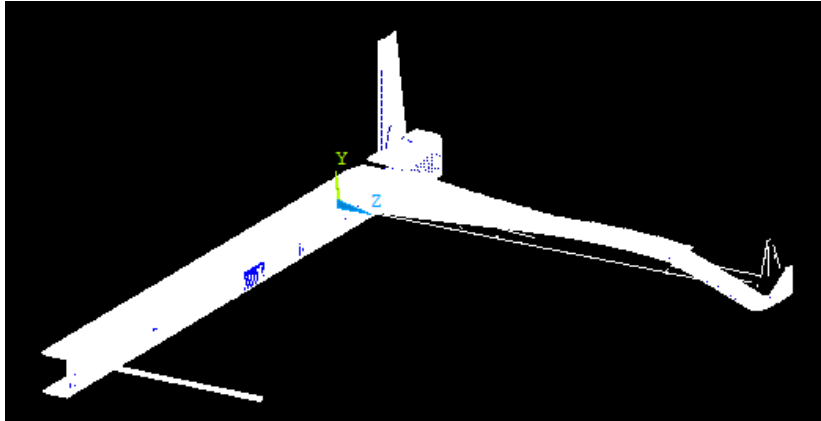


Figure 4.33: Mode shape 6 general aircraft deformation and undeformed aircraft contours.

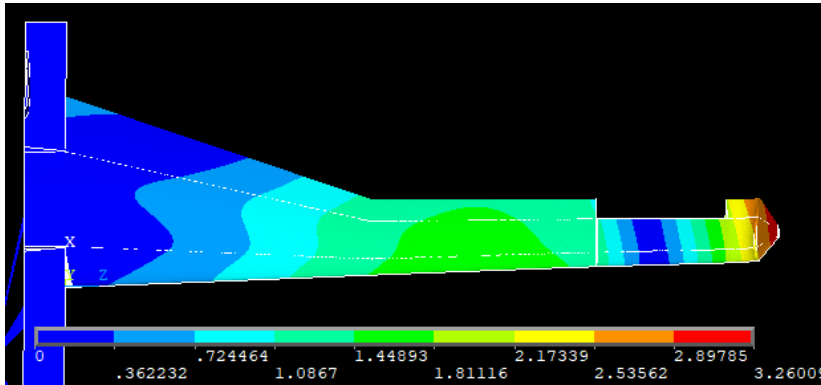


Figure 4.34: Mode shape 6 total deformation on critical region.

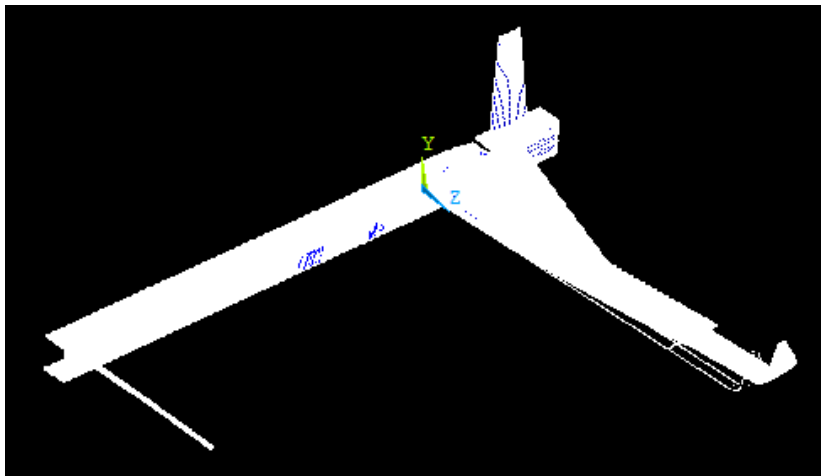


Figure 4.35: Mode shape 7 general aircraft deformation and undeformed aircraft contours.

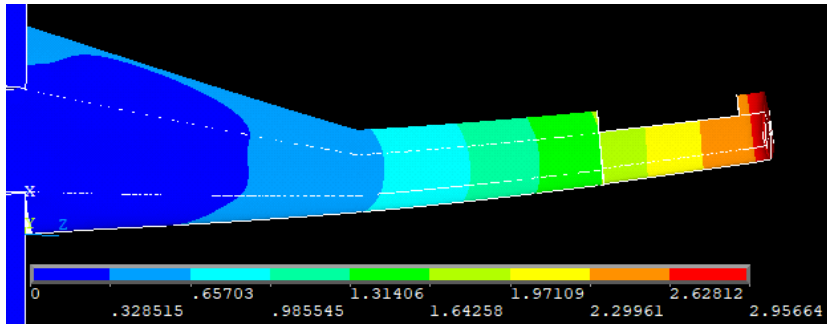


Figure 4.36: Mode shape 7 total deformation on critical region.

The fuselage also exhibits a modal frequency at 75.561Hz, associated with bending in the  $Z$  direction (figures 4.37 and 4.38).

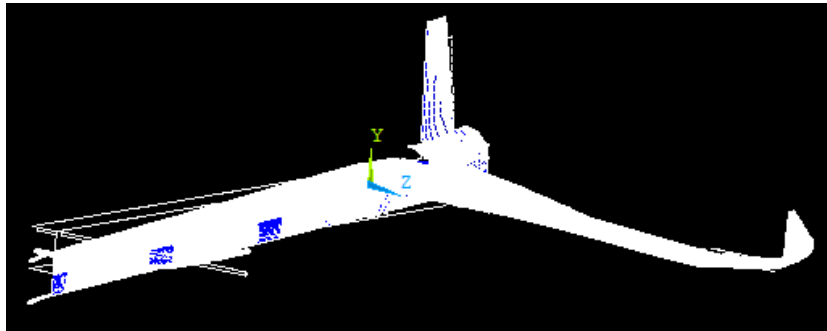


Figure 4.37: Mode shape 8 general aircraft deformation and undeformed aircraft contours.

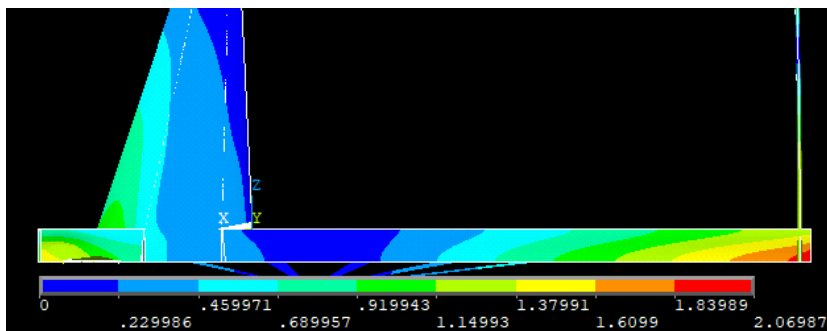


Figure 4.38: Mode shape 8 total deformation on critical region.

It was also possible to identify two torsion mode shapes in the wing, one at 91.112Hz and other at 109.74Hz. The identified torsion develops in the  $Y$  direction for the two frequencies (figures 4.39 to 4.42).

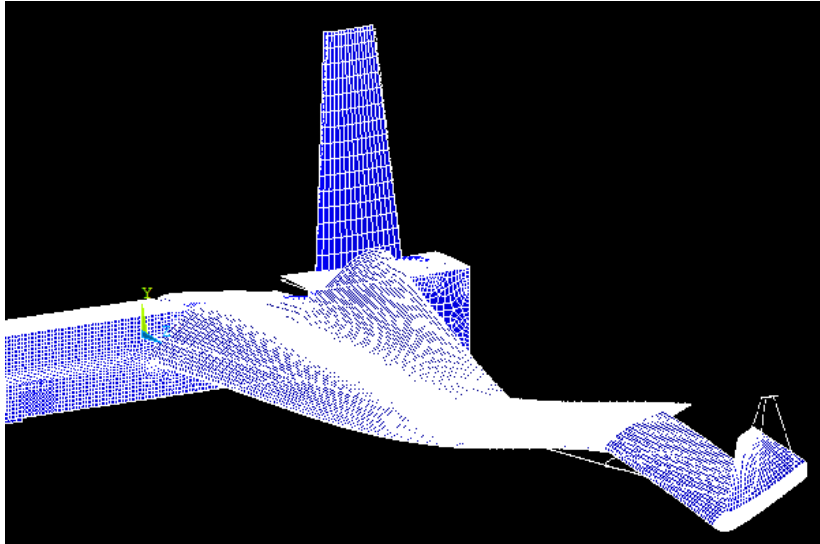


Figure 4.39: Mode shape 9 general aircraft deformation and undeformed aircraft contours.

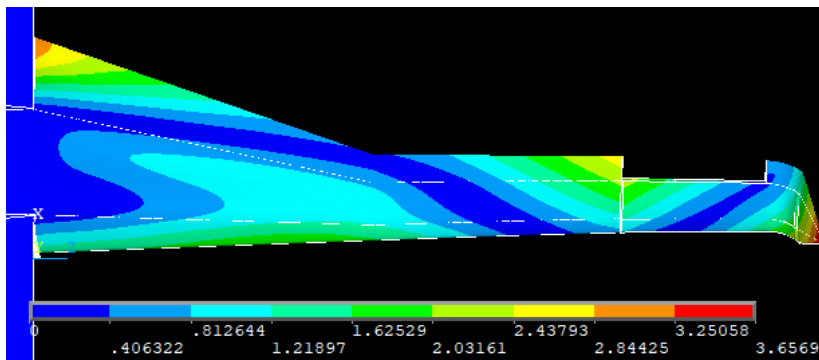


Figure 4.40: Mode shape 9 total deformation on critical region.

Moreover, a bending mode in the  $X$  direction is also visible in the fin for the last detected natural frequency (figures 4.41 and 4.42), coupled to the wing torsion mode mentioned above.

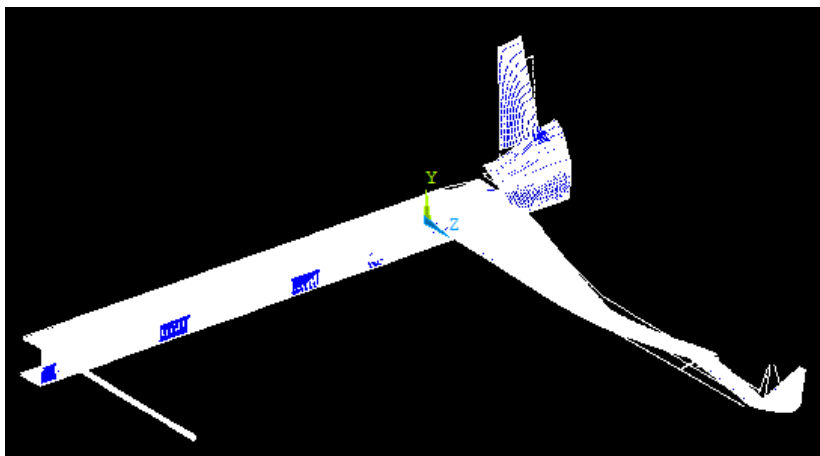


Figure 4.41: Mode shape 10 general aircraft deformation and undeformed aircraft contours.

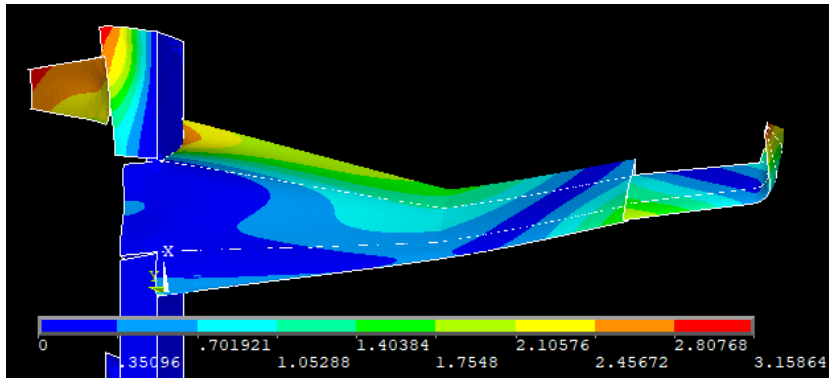


Figure 4.42: Mode shape 10 total deformation on critical region.



# Chapter 5

## Conclusions

### 5.1 Achievements

This master thesis addresses the entire process of a surrogate based, multiobjective, multi-fidelity MDO of the fixed-wing part of a VTOL canard configuration UAV, developed to fly close to sea level and to be capable of detecting and following submerged submarines making use of a MAD sensor. The aircraft was optimized to maximize range by formulating the objective function considering two different objectives, minimizing the structural mass as well as maximizing the lift to drag ratio.

The first step was to identify and select the design variables and constraints that were considered adequate and allowed to parameterize the aircraft in such way that the design variables have influence on the objective.

It was then possible to generate two parametric models to represent the structure and the exterior surfaces, taking into account most of the constraints, such as, dimensional restrictions and also trim, stability and stall conditions. The only exception was the structural integrity, measured by the Tsai-Wu failure criterion, being the only constraint applied directly to the optimization algorithm.

A decomposition architecture was prepared to run at each complete iteration of the optimization. It included a preliminary LF calculation of the aerodynamic loads based on Prandtl's LLT, a structural FEM analysis to calculate the structural mass as well as the Tsai-Wu failure index, and also a CFD analysis for the aerodynamic characterization of the aircraft and to determine the trim conditions.

An initial sample set with 41 different samples obtained from a Latin-Hypercube sampling was used to build three Kriging based surrogate models, for the structural mass, the lift to drag ratio, and also for the Tsai-Wu failure index. The employment of surrogate models reduced the number of design points that went through complete evaluations improving the efficiency of the optimization.

The exploration of the design space was carried out by applying a strategy integrating multiple search methods exploiting combinations of surrogate predictions, expected improvement and the probability of feasibility.

A GA was used at each iteration to assess the considered search functions, providing new points for evaluation that were estimated to be an improvement from the existing samples. The selected new

points were evaluated and subsequently added to the database to update the surrogate models at each complete cycle.

A final solution was obtained when the available time for the optimization expired. The optimum found exhibits a significant improvement in range in comparison with the initial best configuration, indicating a successful optimization, although convergence was not completely verified.

Finally, a more detailed characterization and validation of the the final configuration was carried out to increase confidence on the design, as well as to identify some of its handicaps, and also to verify that the constraints and requirements were met, except the one for the stall speed. The final design also revealed some drawbacks related to drag and interference between the wing and canard air flows. Modifications on the canard design should be considered targeting a better overall performance. In particular, increasing its area would allow to trim the aircraft for higher values of lift coefficient on the wing, consequently reducing the stall speed. Furthermore, lowering its position would reduce the interference on the airflow around the wing making the wing lift distribution more elliptical, thus reducing drag.

## 5.2 Future Work

Although the optimization was effective by increasing range to almost the triple, it would benefit of additional time to run more iterations, as the last iteration showed an increase in the variation of range, indicating that further improvements could still be achieved before reaching convergence. Also, the wing and canard drag are very significant, suggesting that both surfaces can possibly be further optimized.

The time limitation is mostly due to two reasons. First, the running time required for the HF simulations, in particular the CFD analysis, which corresponds to approximately 85% of the time of an entire optimization cycle. This factor can be less restraining with the development of new computational tools and more powerful computers that allow to run heavier simulations faster. On the other hand, the lack of automation between the different stages of each iteration, such as, the transfer of data from one software to another, as well as the update of the database and the surrogate models, made it necessary for the author to perform these tasks manually, which was very time consuming. A more continuous analysis considering multi-fidelity would allow the optimization to run autonomously for longer periods, reducing the number of manual interventions required.

The learning and prediction process of the Kriging surrogate models showed a slow development in this problem and it is mostly data driven, requiring a large quantity of sampled input information to make satisfactory predictions and explore desired regions of the design space, even when employing search methods like the EI and the PF. The author's input was essential to select the new samples to evaluate, as well as to introduce the new design points to guide the optimizer towards the optimum. A possible approach could be to remove some of the black-box limitations of surrogate modeling by adding features to the search methods that give preference to certain regions of the design space based on empirical knowledge. For example, promoting configurations with higher aspect ratios or configurations that can be trimmed at a small AoA, being aligned with the flow in an ideal condition, as these two factors are

known to have a beneficial influence on the increase of the lift to drag ratio. It could be implemented in a similar way to the PF, except instead of prioritizing designs that are more likely to be feasible, it would give more weight to designs that are expected to possess the desired properties.

Finally, the next task should be proceed to the detailed design of the UAV. It is important to identify all the components to integrate in the aircraft, as well as position them taking into account the desired CoG position. Additionally, the propulsive design should be of special focus, including the engine selection, power distribution, selection and sizing of the rotor blades, among others. A fully defined propulsion system will allow the absolute quantification of range, instead of the relative improvements obtained so far.



# Bibliography

- [1] B. M. W. Luís. Design and development of a magnetic anomaly detection unmanned aerial vehicle. Master's thesis, Instituto Superior Técnico, 2019.
- [2] J. Sobieszczanski-Sobieski and R. T. Haftka. Multidisciplinary aerospace design optimization: Survey of recent developments. *Structural Optimization*, 14(1):1–23, 1997. ISSN 09344373. doi: 10.1007/BF01197554.
- [3] A. Papageorgiou, M. Tarkian, K. Amadori, and J. Ölvander. Multidisciplinary design optimization of aerial vehicles: A review of recent advancements. *International Journal of Aerospace Engineering*, 2018, 2018. ISSN 16875974. doi: 10.1155/2018/4258020.
- [4] S. L. Padula and R. E. Gillian. Multidisciplinary environments: A history of engineering framework development. In *Collection of Technical Papers - 11th AIAA/ISSMO Multidisciplinary Analysis and Optimization Conference*, Portsmouth, Virginia, USA, 2006. ISBN 1563478234. doi: 10.2514/6.2006-7083.
- [5] F. A. Viana, T. W. Simpson, V. Balabanov, and V. Toropov. Metamodeling in multidisciplinary design optimization: How far have we really come? *AIAA Journal*, 52(4):670–690, 2014. ISSN 00011452. doi: 10.2514/1.J052375.
- [6] M. Amine Bouhlef, N. Bartoli, R. G. Regis, A. Otsmane, and J. Morlier. Efficient global optimization for high-dimensional constrained problems by using the Kriging models combined with the partial least squares method. *Engineering Optimization*, 50(12):2038–2053, 2018. ISSN 10290273. doi: 10.1080/0305215X.2017.1419344.
- [7] Q. Zhou, J. Wu, T. Xue, and P. Jin. A two-stage adaptive multi-fidelity surrogate model-assisted multi-objective genetic algorithm for computationally expensive problems. *Engineering with Computers*, (37):623–639, 2021. ISSN 14355663. doi: 10.1007/s00366-019-00844-8.
- [8] J. R. Martins and A. B. Lambe. Multidisciplinary design optimization: A survey of architectures. *AIAA Journal*, 51(9):2049–2075, 2013. ISSN 00011452. doi: 10.2514/1.J051895.
- [9] Z. Wang, W. Huang, and L. Yan. Multidisciplinary design optimization approach and its application to aerospace engineering. *Chinese Science Bulletin*, 59(36):5338–5353, 2014. ISSN 18619541. doi: 10.1007/s11434-014-0671-1.

- [10] W. Hurwitz, S. Donovan, J. A. Camberos, and B. German. A systems engineering approach to the application of multidisciplinary design, analysis and optimization (MDAO) for Efficient Supersonic Air-Vehicle Exploration (ESAVE). In *12th AIAA Aviation Technology, Integration and Operations (ATIO) Conference and 14th AIAA/ISSMO Multidisciplinary Analysis and Optimization Conference*, Indianapolis, IN, USA, 2012. ISBN 9781600869303. doi: 10.2514/6.2012-5491.
- [11] S. K. Rallabhandi and D. N. Mavris. Simultaneous airframe and propulsion cycle optimization for supersonic aircraft design. *Journal of Aircraft*, 45(1):38–55, 2008. ISSN 15333868. doi: 10.2514/1.33183.
- [12] L. o. E. Chan, M. o. E. Akrami, and A. o. E. Javadi. Optimisation of a conceptual aircraft model using a genetic algorithm and 3D Computational Fluid Dynamics (CFD). In *UK Association for Computational Mechanics Conference*, London, UK, 2019. URL <http://hdl.handle.net/10871/36789>.
- [13] O. Gur, M. Bhatia, W. H. Mason, J. A. Schetz, R. K. Kapania, and T. Nam. Development of a framework for truss-braced wing conceptual MDO. *Structural and Multidisciplinary Optimization*, 44(2):277–298, 2011. ISSN 1615147X. doi: 10.1007/s00158-010-0612-9.
- [14] M. Sadraey. A systematic approach in aircraft configuration design optimization. In *The 26th Congress of ICAS and 8th AIAA Aviation Technology, Integration and Operations (ATIO) Conference*, Anchorage, Alaska, 2008. doi: 10.2514/6.2008-8926.
- [15] J. Yoon, N. V. Nguyen, S. M. Choi, J. W. Lee, S. Kim, and Y. H. Byun. Multidisciplinary general aviation aircraft design optimizations incorporating airworthiness constraints. In *10th AIAA Aviation Technology, Integration and Operations Conference 2010, ATIO 2010*, Fort Worth, TX, USA, 2010. ISBN 9781617825132. doi: 10.2514/6.2010-9304.
- [16] S. Choi, J. J. Alonso, and H. M. Kroo. Two-level multifidelity design optimization studies for supersonic jets. *Journal of Aircraft*, 46(3):776–790, 2009. ISSN 15333868. doi: 10.2514/1.34362.
- [17] S. Rajagopal and R. Ganguli. Multidisciplinary design optimization of a uav wing using kriging based multi-objective genetic algorithm. In *50th Collection of Technical Papers - AIAA/ASME/ASCE/AHS/ASC Structures, Structural Dynamics and Materials Conference*, Palm Springs, CA, USA, 2009. ISBN 9781563479731. doi: 10.2514/6.2009-2219.
- [18] D. H. Di Bianchi, T. H. Orra, and P. Paglione. Monte Carlo based robust MDO applied to aircraft conceptual design: A technical-financial coupling optimization strategy. In *15th AIAA Aviation Technology, Integration, and Operations Conference, AIAA AVIATION Forum, (AIAA 2015-2737)*, Dallas, TX, USA, 2015. ISBN 9781624103698. doi: 10.2514/6.2015-2737.
- [19] T. Lukaczyk, A. D. Wendorff, E. Boteroz, T. Macdonaldz, T. Momosez, A. Variyarz, J. M. Veghz, M. Colonnox, T. D. Economon, J. J. Alonsok, T. H. Orra, and C. I. Da Silvayy. SUAVE: An open-source environment for multi-fidelity conceptual vehicle design. In *16th AIAA/ISSMO Multidisci-*

- iplinary Analysis and Optimization Conference, AIAA AVIATION Forum, (AIAA 2015-3087), Dallas, TX, USA, 2015. ISBN 9781624103681. doi: 10.2514/6.2015-3087.*
- [20] S. R. Dean, J. J. Doherty, and T. R. Wallace. MDO-based concept modelling and the impact of fuel systems on wing design. In *47th AIAA Aerospace Sciences Meeting including the New Horizons Forum and Aerospace Exposition*, Orlando, FL, USA, 2009. ISBN 9781563479694. doi: 10.2514/6.2009-434.
- [21] R. E. Perez, H. H. Liu, and K. Behdinan. Multidisciplinary optimization framework for control-configuration integration in aircraft conceptual design. *Journal of Aircraft*, 43(6):1937–1948, 2006. ISSN 15333868. doi: 10.2514/1.22263.
- [22] C. C. Morris, C. Sultan, D. L. Allison, J. A. Schetz, and R. K. Kapania. Towards flying qualities constraints in the multidisciplinary design optimization of a supersonic tailless aircraft. In *12th AIAA Aviation Technology, Integration and Operations (ATIO) Conference and 14th AIAA/ISSMO Multidisciplinary Analysis and Optimization Conference*, Indianapolis, IN, USA, 2012. ISBN 9781600869303. doi: 10.2514/6.2012-5517.
- [23] D. D. Smith, A. T. Isikveren, R. M. Ajaj, and M. I. Friswell. Multidisciplinary design optimization of an active nonplanar polymorphing wing. In *27th Congress of the International Council of the Aeronautical Sciences 2010, ICAS 2010*, Nice, France, 2010. ISBN 9781617820496.
- [24] A. Ceruti, G. Caligiana, and F. Persiani. Comparative evaluation of different optimization methodologies for the design of UAVs having shape obtained by hot wire cutting techniques. *International Journal on Interactive Design and Manufacturing*, 7(2):63–78, 2013. ISSN 19552513. doi: 10.1007/s12008-012-0164-x.
- [25] N. V. Nguyen, S. M. Choi, W. S. Kim, J. W. Lee, S. Kim, D. Neufeld, and Y. H. Byun. Multidisciplinary Unmanned Combat Air Vehicle system design using Multi-Fidelity Model. *Aerospace Science and Technology*, 26(1):200–210, 2013. ISSN 12709638. doi: 10.1016/j.ast.2012.04.004.
- [26] R. P. Henderson, J. R. Martins, and R. E. Perez. Aircraft conceptual design for optimal environmental performance. *Aeronautical Journal*, 116(1175):1–22, 2012. ISSN 00019240. doi: 10.1017/S000192400000659X.
- [27] J. P. Berends, M. J. Van Tooren, and D. N. Belo. A distributed Multi-Disciplinary Optimisation of a blended wing body UAV using a multi-agent task environment. In *Collection of Technical Papers - AIAA/ASME/ASCE/AHS/ASC Structures, Structural Dynamics and Materials Conference*, Newport, RI, USA, 2006. ISBN 1563478080. doi: 10.2514/6.2006-1610.
- [28] E. Alyanak, R. Kolonay, P. Flick, N. Lindsley, and S. A. Burton. Efficient supersonic air vehicle preliminary conceptual multi-disciplinary design optimization results. In *12th AIAA Aviation Technology, Integration and Operations (ATIO) Conference and 14th AIAA/ISSMO Multidisciplinary Analysis and Optimization Conference*, Indianapolis, IN, USA, 2012. ISBN 9781600869303. doi: 10.2514/6.2012-5518.

- [29] M. Laban and U. Herrmann. Multi-disciplinary analysis and optimization applied to supersonic aircraft part 1: Analysis tools. In *Collection of Technical Papers - AIAA/ASME/ASCE/AHS/ASC Structures, Structural Dynamics and Materials Conference*, Honolulu, Hawaii, 2007. ISBN 1563478927. doi: 10.2514/6.2007-1857.
- [30] A. Gazaix, P. Gendre, E. Chaput, C. Blondeau, G. Carrier, P. Schmollgruber, J. Brezillon, and T. Kier. Investigation of multi-disciplinary optimisation for aircraft preliminary design. In *SAE 2011 AeroTech Congress & Exhibition*, Toulouse, France, 2011. doi: 10.4271/2011-01-2761.
- [31] R. E. Perez and J. R. Martins. pyACDT: An object-oriented framework for aircraft design modelling and multidisciplinary optimization. In *12th AIAA/ISSMO Multidisciplinary Analysis and Optimization Conference, MAO*, Victoria, BC, Canada, 2008. ISBN 9781563479472. doi: 10.2514/6.2008-5955.
- [32] J. Brezillon, A. Ronzheimer, D. Haar, M. Abu-Zurayk, M. Lummer, W. Krüger, and F. J. Natterer. Development and application of multi-disciplinary optimization capabilities based on high-fidelity methods. In *53rd AIAA/ASME/ASCE/AHS/ASC Structures, Structural Dynamics and Materials Conference 2012*, Honolulu, Hawaii, 2012. ISBN 9781600869372. doi: 10.2514/6.2012-1757.
- [33] N. Kroll, M. Abu-Zurayk, D. Dimitrov, T. Franz, T. Führer, T. Gerhold, S. Görtz, R. Heinrich, C. Ilic, J. Jepsen, J. Jägersküpper, M. Kruse, A. Krumbein, S. Langer, D. Liu, R. Liepelt, L. Reimer, M. Ritter, A. Schwöppe, J. Scherer, F. Spiering, R. Thormann, V. Togiti, D. Vollmer, and J. H. Wendisch. DLR project Digital-X: towards virtual aircraft design and flight testing based on high-fidelity methods. *CEAS Aeronautical Journal*, 7(1):3–27, 2015. ISSN 18695590. doi: 10.1007/s13272-015-0179-7.
- [34] L. U. Iqbal and J. P. Sullivan. Multidisciplinary design and optimization (MDO) methodology for the aircraft conceptual design. In *50th AIAA Aerospace Sciences Meeting Including the New Horizons Forum and Aerospace Exposition*, Nashville, TN, USA, 2012. doi: 10.2514/6.2012-552.
- [35] S. Choi, J. J. Alonso, U. M. Kroo, and M. Wintzer. Multifidelity design optimization of low-boom supersonic jets. *Journal of Aircraft*, 45(1):106–118, 2008. ISSN 15333868. doi: 10.2514/1.28948.
- [36] P. W. Jansen and R. E. Perez. Coupled optimization of aircraft design and fleet allocation with uncertain passenger demand. In *2013 Aviation Technology, Integration, and Operations Conference, AIAA AVIATION Forum, (AIAA 2013-4392)*, Los Angeles, CA, USA, 2013. ISBN 9781624102257. doi: 10.2514/6.2013-4392.
- [37] P. Piperni, A. DeBlois, and R. Henderson. Development of a multilevel multidisciplinary-optimization capability for an industrial environment. *AIAA Journal*, 51(10):2335–2352, 2013. ISSN 00011452. doi: 10.2514/1.J052180.
- [38] C. G. Pak. Aeroelastic tailoring study of an N+2 low-boom supersonic commercial transport aircraft. In *16th AIAA/ISSMO Multidisciplinary Analysis and Optimization Conference, AIAA*

- AVIATION Forum, (AIAA 2015-2791)*, Dallas, TX, USA, 2015. ISBN 9781624103681. doi: 10.2514/6.2015-2791.
- [39] D. L. Allison, C. C. Morris, J. A. Schetz, R. K. Kapania, C. Sultan, L. T. Watson, J. D. Deaton, and R. V. Grandhiy. A multidisciplinary design optimization framework for design studies of an efficient supersonic air vehicle. In *12th AIAA Aviation Technology, Integration and Operations (ATIO) Conference and 14th AIAA/ISSMO Multidisciplinary Analysis and Optimization Conference*, Indianapolis, IN, USA, 2012. ISBN 9781600869303. doi: 10.2514/6.2012-5492.
- [40] N. V. Nguyen, J. W. Lee, M. Tyan, and D. Lee. Possibility-based multidisciplinary optimisation for electric-powered unmanned aerial vehicle design. *Aeronautical Journal*, 119(1221):1397–1414, 2015. ISSN 00019240. doi: 10.1017/S0001924000011313.
- [41] C. Davies, M. Stelmack, S. Zink, A. de la Garza, and P. Flick. High fidelity MDO process development and application to fighter strike conceptual design. In *12th AIAA Aviation Technology, Integration and Operations (ATIO) Conference and 14th AIAA/ISSMO Multidisciplinary Analysis and Optimization Conference*, Indianapolis, IN, USA, 2012. ISBN 9781600869303. doi: 10.2514/6.2012-5490.
- [42] F. Afonso, J. Vale, F. Lau, and A. Suleman. Multidisciplinary performance based optimization of morphing aircraft. In *22nd AIAA/ASME/AHS Adaptive Structures Conference, AIAA SciTech Forum, (AIAA 2014-0761)*, National Harbor, MD, USA, 2014. doi: 10.2514/6.2014-0761.
- [43] R. Navaratne and J. Murugaiyan. Multi disciplinary optimization of flight trajectories. In *IEEE Aerospace Conference Proceedings*, pages 1–15, Big Sky, MT, USA, 2012. ISBN 9781457705564. doi: 10.1109/AERO.2012.6187406.
- [44] B. Yan, P. W. Jansen, and R. E. Perez. Multidisciplinary design optimization of airframe and trajectory considering cost and emissions. In *12th AIAA Aviation Technology, Integration and Operations (ATIO) Conference and 14th AIAA/ISSMO Multidisciplinary Analysis and Optimization Conference*, Indianapolis, IN, USA, 2012. ISBN 9781600869303.
- [45] J. M. Longo, R. Dittrich, D. Banuti, M. Sippel, J. Klevanski, U. Atanassov, G. Carrier, P. Duveau, I. S. El Din, R. Thepot, A. Loubeau, F. Coulouvrat, R. Jarlas, H. Rabia, D. Perigo, and J. Steelant. Concept study for a Mach 6 transport aircraft. In *47th AIAA Aerospace Sciences Meeting including the New Horizons Forum and Aerospace Exposition*, Orlando, FL, USA, 2009. ISBN 9781563479694. doi: 10.2514/6.2009-435.
- [46] A. M. Morris, C. B. Allen, and T. C. Rendall. Wing design by aerodynamic and aeroelastic shape optimisation. In *26th AIAA Applied Aerodynamics Conference, Guidance, Navigation, and Control and Co-located Conferences*, Honolulu, Hawaii, 2008. doi: 10.2514/6.2008-7054.
- [47] K. Amadori, C. Jouannet, and P. Krus. A framework for aerodynamic and structural optimization in conceptual design. In *25th AIAA Applied Aerodynamics Conference, Fluid Dynamics and Co-located Conferences*, Miami, FL, USA, 2007. ISBN 1563478986. doi: 10.2514/6.2007-4061.

- [48] K. Geiselhart, L. Ozoroski, J. Fenbert, E. Shields, and W. Li. Integration of Multifidelity Multidisciplinary Computer Codes for Design and Analysis of Supersonic Aircraft. In *49th AIAA Aerospace Sciences Meeting including the New Horizons Forum and Aerospace Exposition, Aerospace Sciences Meetings*, Orlando, FL, USA, 2011. doi: 10.2514/6.2011-465.
- [49] T. Zhang, Z. Wang, W. Huang, and L. Yan. Parameterization and optimization of hypersonic-gliding vehicle configurations during conceptual design. *Aerospace Science and Technology*, 58: 225–234, 2016. ISSN 12709638. doi: 10.1016/j.ast.2016.08.020.
- [50] A. DeBlois and M. Abdo. Multi-fidelity multidisciplinary design optimization of metallic and composite regional and business jets. In *13th AIAA/ISSMO Multidisciplinary Analysis and Optimization Conference*, Fort Worth, TX, USA, 2010. ISBN 9781600869549. doi: 10.2514/6.2010-9191.
- [51] S. Ricci and M. Terraneo. Application of MDO techniques to the preliminary design of morphed aircraft. In *11th AIAA/ISSMO Multidisciplinary Analysis and Optimization Conference*, Portsmouth, VA, USA, 2006. ISBN 1563478234. doi: 10.2514/6.2006-7018.
- [52] F. Daoud, Ö. Petersson, S. Deinert, and P. Bronny. Multidisciplinary airframe design process: Incorporation of steady and unsteady aeroelastic loads. In *12th AIAA Aviation Technology, Integration and Operations (ATIO) Conference and 14th AIAA/ISSMO Multidisciplinary Analysis and Optimization Conference*, Indianapolis, IN, USA, 2012. ISBN 9781600869303. doi: 10.2514/6.2012-5715.
- [53] K. Alston, S. Doyle, T. Winter, H. Kim, and S. Ragon. High fidelity multidisciplinary optimization (HFMDO). In *13th AIAA/ISSMO Multidisciplinary Analysis and Optimization Conference*, Fort Worth, TX, USA, 2010. ISBN 9781600869549. doi: 10.2514/6.2010-9319.
- [54] L. Versiani Cabral, P. Paglione, and B. Silva De Mattos. Multi-objective design optimization framework for conceptual design of families of aircraft. In *44th AIAA Aerospace Sciences Meeting and Exhibit*, Reno, NV, USA, 2006. ISBN 1563478072. doi: 10.2514/6.2006-1328.
- [55] K. Reynolds and N. Nguyen. Multi-objective wing shape optimization of an elastically-shaped aircraft concept. In *51st AIAA Aerospace Sciences Meeting including the New Horizons Forum and Aerospace Exposition*, Grapevine (Dallas/Ft. Worth Region), TX, USA, 2013. ISBN 9781624101816. doi: 10.2514/6.2013-142.
- [56] K. S. Jeon, J. W. Lee, Y. H. Byun, and Y. H. Yu. Multidisciplinary UCAV system design and optimization using repetitive response surface enhancement technique. In *48th AIAA/ASME/ASCE/AHS/ASC Structures, Structural Dynamics, and Materials Conference, Structures, Structural Dynamics, and Materials and Co-located Conferences*, Honolulu, Hawaii, 2007. ISBN 1563478927. doi: 10.2514/6.2007-1902.
- [57] B. Morrissey and R. McDonald. Multidisciplinary design optimization of an extreme aspect ratio HALE UAV. In *9th AIAA Aviation Technology, Integration and Operations (ATIO) Conference*,

- Aircraft Noise and Emissions Reduction Symposium (ANERS)*, Hilton Head, SC, USA, 2009. ISBN 9781563479809. doi: 10.2514/6.2009-6949.
- [58] C. Jouannet and P. Krus. Direct simulation based optimization for aircraft design including systems. In *11th AIAA/ISSMO Multidisciplinary Analysis and Optimization Conference*, Portsmouth, VA, USA, 2006. ISBN 1563478234. doi: 10.2514/6.2006-7113.
- [59] S. A. Ning and I. Kroo. Multidisciplinary considerations in the design of wings and wing tip devices. *Journal of Aircraft*, 47(2):534–543, 2010. ISSN 15333868. doi: 10.2514/1.41833.
- [60] A. A. Mirzoyan. Studies on MDO of engine design parameters with mission, noise and emission criteria at SSBJ engine conceptual design. In *26th Congress of International Council of the Aeronautical Sciences 2008, ICAS 2008*, Anchorage, AK, USA, 2008. ISBN 9781605607153.
- [61] S. V. Subramanian and D. A. DeLaurentis. Application of Multidisciplinary Systems-of-Systems Optimization to an Aircraft Design Problem. *Systems Engineering*, 19(3):235–251, 2016. ISSN 15206858. doi: 10.1002/sys.21358.
- [62] Y. Deremaux, N. Pietremont, J. Négrier, E. Herbin, and M. Ravachol. Environmental MDO and uncertainty hybrid approach applied to a supersonic business jet. In *12th AIAA/ISSMO Multidisciplinary Analysis and Optimization Conference, MAO*, Victoria, BC, Canada, 2008. ISBN 9781563479472. doi: 10.2514/6.2008-5832.
- [63] U. Iemma and M. Diez. Optimal conceptual design of aircraft including community noise prediction. In *12th AIAA/CEAS Aeroacoustics Conference*, Cambridge, MA, USA, 2006. ISBN 1563478099. doi: 10.2514/6.2006-2621.
- [64] P. Piperni, M. Abdo, F. Kafyeke, and A. T. Isikveren. Preliminary aerostructural optimization of a large business jet. *Journal of Aircraft*, 44(5):1422–1438, 2007. ISSN 15333868. doi: 10.2514/1.26989.
- [65] N. Davendralingam and W. Crossley. Robust optimization of aircraft design and airline network design incorporating economic trends. In *11th AIAA Aviation Technology, Integration, and Operations (ATIO) Conference, including the AIAA Balloon Systems Conference and 19th AIAA Lighter-Than-Air Technology Conference*, Virginia Beach, VA, USA, 2011. ISBN 9781600869419. doi: 10.2514/6.2011-6927.
- [66] S. S. Ghoman, R. K. Kapania, P. C. Chen, D. Sarhaddi, and D. H. Lee. Multifidelity, multistrategy, and multidisciplinary design optimization environment. *Journal of Aircraft*, 49(5):1255–1270, 2012. ISSN 15333868. doi: 10.2514/1.C031507.
- [67] C. Werner-Westphal, W. Heinze, and P. Horst. Multidisciplinary integrated preliminary design applied to unconventional aircraft configurations. *Journal of Aircraft*, 45(2):581–590, 2008. ISSN 15333868. doi: 10.2514/1.32138.

- [68] P. W. Jansen, R. E. Perez, and J. R. Martins. Aerostructural optimization of nonplanar lifting surfaces. *Journal of Aircraft*, 47(5):1490–1503, 2010. ISSN 15333868. doi: 10.2514/1.44727.
- [69] L. Cavagna, S. Ricci, and L. Travaglini. NeoCASS: An integrated tool for structural sizing, aerodynamic analysis and MDO at conceptual design level. *Progress in Aerospace Sciences*, 47(8): 621–635, 2011. ISSN 03760421. doi: 10.1016/j.paerosci.2011.08.006.
- [70] E. Safavi, M. Tarkian, H. Gavel, and J. Ölvander. Collaborative multidisciplinary design optimization: A framework applied on aircraft conceptual system design. *Concurrent Engineering Research and Applications*, 23(3):236–249, 2015. ISSN 15312003. doi: 10.1177/1063293X15587020.
- [71] D. Neufeld, J. Chung, and K. Behdinan. Aircraft conceptual design optimization considering fidelity uncertainties. *Journal of Aircraft*, 48(5):1602–1612, 2011. ISSN 15333868. doi: 10.2514/1.C031312.
- [72] S. G. Lehner, L. B. Lurati, G. C. Bower, E. J. Cramer, W. A. Crossley, F. Engelsen, I. M. Kroo, S. C. Smith, and K. E. Willcox. Advanced multidisciplinary optimization techniques for efficient subsonic aircraft design. In *48th AIAA Aerospace Sciences Meeting Including the New Horizons Forum and Aerospace Exposition*, Orlando, FL, USA, 2010. ISBN 9781600867392. doi: 10.2514/6.2010-1321.
- [73] L. Travaglini, S. Ricci, and G. Bindolino. PyPAD: A multidisciplinary framework for preliminary airframe design. *Aircraft Engineering and Aerospace Technology*, 88(5):649–664, 2016. ISSN 17488842. doi: 10.1108/AEAT-02-2015-0061.
- [74] M. Muir, C. Muldal, E. Kolb, G. Robertson, A. Parkinson, O. M. Querin, R. W. Hewson, and V. V. Toropov. The use of MDO and advanced manufacturing to demonstrate rapid, agile construction of a mission optimized UAV. In *54th AIAA/ASME/ASCE/AHS/ASC Structures, Structural Dynamics, and Materials Conference, (AIAA 2013- 1675)*, Boston, MA, USA, 2013. ISBN 9781624102233. doi: 10.2514/6.2013-1675.
- [75] N. V. Nguyen, M. Tyan, and J. W. Lee. A modified variable complexity modeling for efficient multidisciplinary aircraft conceptual design. *Optimization and Engineering*, 16(2):483–505, 2015. ISSN 15732924. doi: 10.1007/s11081-014-9273-7.
- [76] M. Sohst, J. Vale, C. Crawford, and G. Potter. A framework for multi-fidelity multi-disciplinary kriging-based surrogate model optimization of novel aircraft configurations. In *NATO STO-MP-AVT-324*, 2020. doi: 10.14339/STO-MP-AVT-324-03\_PDF.
- [77] Y. Zhang, N. H. Kim, C. Park, and R. T. Haftka. Multifidelity surrogate based on single linear regression. *AIAA Journal*, 56(12):4944–4952, 2018. ISSN 00011452. doi: 10.2514/1.J057299.
- [78] T. Zill, P. D. Ciampa, and B. Nagel. A collaborative MDO approach for the flexible aircraft. In *54th AIAA/ASME/ASCE/AHS/ASC Structures, Structural Dynamics, and Materials Conference, (AIAA 2013-1677)*, 2013. ISBN 9781624102233. doi: 10.2514/6.2013-1677.

- [79] R. Reuter, S. Iden, R. Snyder, and D. L. Allison. An overview of the optimized integrated multidisciplinary systems program. In *57th AIAA/ASCE/AHS/ASC Structures, Structural Dynamics, and Materials Conference, AIAA Sci- Tech Forum, (AIAA 2016-0674)*, San Diego, CA, USA, 2016. ISBN 9781624103926. doi: 10.2514/6.2016-0674.
- [80] F. Daoud, S. Deinert, R. Maierl, and Ö. Petersson. Integrated multidisciplinary aircraft design process supported by a decentral MDO framework. In *16th AIAA/ISSMO Multidisciplinary Analysis and Optimization Conference, AIAA AVI- ATION Forum, (AIAA 2015-3090)*, Dallas, TX, USA, 2015. ISBN 9781624103681. doi: 10.2514/6.2015-3090.
- [81] K. S. Zhang, Z. H. Han, W. J. Li, and W. P. Song. Coupled aerodynamic/structural optimization of a subsonic transport wing using a surrogate model. *Journal of Aircraft*, 45(6):2167–2170, 2008. ISSN 15333868. doi: 10.2514/1.36047.
- [82] P. Gamboa, J. Vale, F. J. Lau, and A. Suleman. Optimization of a morphing wing based on coupled aerodynamic and structural constraints. *AIAA Journal*, 47(9):2087–2104, 2009. ISSN 00011452. doi: 10.2514/1.39016.
- [83] D. Bryson, B. Stanford, A. McClung, T. Sims, J. Miranda, P. Beran, and G. Parker. Multidisciplinary Optimization of a Hovering Wing with a Service-Oriented Framework and Experimental Model Validation. In *49th AIAA Aerospace Sciences Meeting including the New Horizons Forum and Aerospace Exposition, Aerospace Sciences Meetings*, Orlando, FL, USA, 2011. doi: 10.2514/6.2011-1133.
- [84] T. Long, L. Liu, J. Wang, S. Zhou, and L. Meng. Multi-objective multidisciplinary optimization of long-endurance UAV wing using surrogate models in model center. In *12th AIAA/ISSMO Multidisciplinary Analysis and Optimization Conference, MAO*, Victoria, BC, Canada, 2008. ISBN 9781563479472. doi: 10.2514/6.2008-5918.
- [85] A. Iwaniuk, W. Wisniowski, and J. Zóltak. Multi-disciplinary optimisation approach for a light turbo-prop aircraft-engine integration and improvement. *Aircraft Engineering and Aerospace Technology*, 88(2):348–355, 2016. ISSN 00022667. doi: 10.1108/AEAT-02-2015-0070.
- [86] S. Haghghat, J. R. Martins, and H. H. Liu. Aeroservoelastic design optimization of a flexible wing. *Journal of Aircraft*, 49(2):432–443, 2012. ISSN 15333868. doi: 10.2514/1.C031344.
- [87] P. S. Prakasha, P. D. Ciampa, L. Boggero, and M. Fioriti. Assessment of airframe-subsystems synergy on overall aircraft performance in a collaborative design environment. In *17th AIAA/ISSMO Multidisciplinary Analysis and Optimization Conference, AIAA AVIATION Forum, (AIAA 2016-3667)*, Washington, D.C, USA, 2016. ISBN 9781624104398.
- [88] A. Tfaily, K. Huynh, P. Piperni, and S. Liscouet-Hanke. Landing gear integration in an industrial multi-disciplinary optimization environment. In *SAE AeroTech Congress & Exhibition*, Montreal, Canada, 2013. doi: 10.4271/2013-01-2319.

- [89] R. P. Liem, G. K. Kenway, and J. R. Martins. Multimission aircraft fuel-burn minimization via multipoint aerostructural optimization. *AIAA Journal*, 53(1):104–122, 2015. ISSN 00011452. doi: 10.2514/1.J052940.
- [90] T. Kumano, S. Jeong, S. Obayashi, Y. Ito, K. Hatanaka, and H. Morino. Multidisciplinary design optimization of wing shape for a small jet aircraft using kriging model. In *44th AIAA Aerospace Sciences Meeting*, Reno, NV, USA, 2006. ISBN 1563478072. doi: 10.2514/6.2006-932.
- [91] T. Lefebvre, P. Schmollgruber, C. Blondeau, and G. Carrier. Aircraft conceptual design in a multi-level, multi-fidelity, multi-disciplinary optimization process. In *28th Congress of the International Council of the Aeronautical Sciences*, Brisbane, Australia, 2012. ISBN 9781622767540.
- [92] E. Safavi, M. V. Raghu Chaitanya, J. Ölvander, and P. Krus. Multidisciplinary optimization of aircraft vehicle system for conceptual analysis. In *51st AIAA Aerospace Sciences Meeting including the New Horizons Forum and Aerospace Exposition*, Grapevine (Dallas/Ft. Worth Region), TX, USA, 2013. ISBN 9781624101816.
- [93] A. S. A.I.J. Forrester and A. J. Keane. *Engineering design via surrogate modelling : a practical guide*. John Wiley & Sons Ltd., 1<sup>st</sup> edition, 2008.
- [94] E. Garnier, S. Langlet, P. Klotz, J. Cadillon, J. Simon, J. C. Castelli, and D. Levadoux. Surrogate-Based Conception for Aerodynamic / Stealth Compromise. In *NATO STO-MP-AVT-324*, pages 1–12, 2020. doi: 10.14339/STO-MP-AVT-324.
- [95] L. Brevault, M. Balesdent, A. Hebbal, and A. P. De Mirand. Surrogate model-based multi-objective mdo approach for partially reusable launch vehicle design. In *AIAA Scitech 2019 Forum*, San Diego, California, 2019. ISBN 9781624105784. doi: 10.2514/6.2019-0704.
- [96] N. Bartoli, T. Lefebvre, S. Dubreuil, R. Olivanti, R. Priem, N. Bons, J. R. Martins, and J. Morlier. Adaptive modeling strategy for constrained global optimization with application to aerodynamic wing design. *Aerospace Science and Technology*, 90:85–102, 2019. ISSN 12709638. doi: 10.1016/j.ast.2019.03.041.
- [97] M. J. Kochenderfer and T. A. Wheeler. *Algorithms for Optimization*. MIT Press, 1<sup>st</sup> edition, 2019.
- [98] N. Van Nguyen, J. W. Lee, Y. D. Lee, and H. U. Park. A multidisciplinary robust optimisation framework for UAV conceptual design. *Aeronautical Journal*, 118(1200):123–142, 2014. ISSN 00019240. doi: 10.1017/S0001924000009027.
- [99] T. Zill, D. Böhnke, and B. Nagel. Preliminary aircraft design in a collaborative multidisciplinary design environment. In *11th AIAA Aviation Technology, Integration, and Operations (ATIO) Conference*, Virginia Beach, VA, USA, 2011. ISBN 9781600869419. doi: 10.2514/6.2011-6959.
- [100] J. Neidhoefer, J. Ryan, B. Leahy, and V. Tripp. Cooperative multi-disciplinary design of integral load bearing antennas in small UAVs. In *47th AIAA Aerospace Sciences Meeting including the*

- New Horizons Forum and Aerospace Exposition*, Orlando, FL, USA, 2009. ISBN 9781563479694. doi: 10.2514/6.2009-1653.
- [101] K. Amadori, D. Lundström, and P. Krus. Automated design and fabrication of micro-air vehicles. *Proceedings of the Institution of Mechanical Engineers, Part G: Journal of Aerospace Engineering*, 226(10):1271–1282, 2011. ISSN 09544100. doi: 10.1177/0954410011419612.
- [102] ANSYS. *Mechanical APDL, 2020 R1*. ANSYS Inc., Canonsburg, PA, USA, 2020.
- [103] J. N. Reddy. *An Introduction to the Finite Element Method*. Mc-Graw-Hill, Inc., 2nd edition, 1993.
- [104] *Theory Reference for the Mechanical APDL and Mechanical Applications*. ANSYS, Inc., April 2009.
- [105] F. Campbell. *Structural Composite Materials*, chapter 16. ASM International, 2010.
- [106] R. M. Jones. *Mechanics of composite materials*, chapter 2. Taylor & Francis, Inc., 1999.
- [107] M. Koc, F. O. Sonmez, N. Ersoy, and K. Cinar. Failure behavior of composite laminates under four-point bending. *Journal of Composite Materials*, 50(26):3679–3697, 2016. ISSN 1530793X. doi: 10.1177/0021998315624251.
- [108] H. Debski and J. Jonak. Failure analysis of thin-walled composite channel section columns. *Composite Structures*, 132:567–574, 2015. ISSN 02638223. doi: 10.1016/j.compstruct.2015.05.067.
- [109] ANSYS. *CFX, 2020 R1*. ANSYS Inc., Canonsburg, PA, USA, 2020.
- [110] S. Gudmundsson. *General Aviation Aircraft Design: Applied Methods and Procedures*, chapter 9, pages 379–389. Butterworth-Heinemann, 2014.
- [111] Aerodynamics for Students. 3d prandtl lifting line theory. <http://www.aerodynamics4students.com/subsonic-aerofoil-and-wing-theory/3d-prandtl-lifting-line-theory.php>. [Online: accessed on July 2020].
- [112] M. D. F. Moukalled, L. Mangani. *The Finite Volume Method in Computational Fluid Dynamics*. Springer International Publishing AG, 2016.
- [113] H. K. Versteeg and W. Malalasekera. *An Introduction to Computational Fluid Dynamics*. Pearson Education Limited, 2nd edition, 2007.
- [114] *ANSYS CFX-Solver Theory Guide*. ANSYS, Inc., November 2011.
- [115] W. W. D. George, John C. *Introduction to combinatorics*. CRC Press, 1st edition, 2011.
- [116] D. G. Krige. A Statistical Approach to Some Basic Mine Valuation Problems on the Witwatersrand. *Journal of the Chemical, Metallurgical and Mining Society of South Africa*, 52(6):119–139, 1951. ISSN 0038-223X.

- [117] G. Matheron. Principles of geostatistics. *Economic Geology*, 58(8):1246–1266, 1963. ISSN 03610128. doi: 10.2113/gsecongeo.58.8.1246.
- [118] J. Sacks, W. J. Welch, T. J. Mitchell, and H. P. Wynn. Design and analysis of computer experiments. *Statistical Science*, 4(4):409–423, 1989. ISSN 08834237. doi: 10.1214/ss/1177012413.
- [119] D. R. Jones, M. Schonlau, and W. J. Welch. Efficient Global Optimization of Expensive Black-Box Functions. *Journal of Global Optimization*, 13(4):455–492, 1998. URL <https://link.springer.com/content/pdf/10.1023-%}2FA-%}3A1008306431147.pdf>.
- [120] A. G. Watson and R. J. Barnes. Infill sampling criteria to locate extremes. *Mathematical Geology*, 27(5):589–608, 1995. ISSN 08828121. doi: 10.1007/BF02093902.
- [121] P. Papalambros, P. Goovaerts, and M. J. Sasena. Exploration of Metamodeling Sampling Criteria for Constrained Global Optimization. *Engineering Optimization*, 34(3):263–278, 2002. doi: 10.1080/03052150211751.
- [122] M. Schonlau. *Computer Experiments and Global Optimization*. PhD thesis, University of Waterloo, 1997.
- [123] A. C. Marta. Lecture 04 - heuristic methods. Aircraft Optimal Design, 2019.
- [124] Government of Canada. Exemption from sections 602.41 and 603.66 of the canadian aviation regulations. <https://perma.cc/4SD4-ZHA6>, March 2016. [Online: accessed on May 2020].
- [125] J. Gallant. Diving almanac and book of records - fastest submarine. <https://divingalmanac.com/fastest-submarine/>, September 2017. [Online: accessed on May 2020].
- [126] R. Przybylak. *The Climate of the Artic*. Springer, 2016.
- [127] IAW. Unified lecture 2: The breguet range equation. Technical report, Massachusetts Institute of Technology, 2008. URL: [https://web.mit.edu/16.unified/www/FALL/Unified\\_Concepts/Breguet-Range-U2-notes-Fall08\(2\).pdf](https://web.mit.edu/16.unified/www/FALL/Unified_Concepts/Breguet-Range-U2-notes-Fall08(2).pdf).
- [128] K. E. W. Eastman N. Jacobs and R. M. Pinkerton. The characteristics of 78 related airfoil sections from tests in the variable-density wind tunnel. Report 460, National Advisory Committee for Aeronautics, 1933.
- [129] DS SolidWorks. *SOLIDWORKS 2020*. Dassault Systèmes SolidWorks Corporation, Waltham, MA, USA, 2020.
- [130] J. Oliveira. Apontamentos de estabilidade de voo. September 2018.
- [131] T. C. Corke. *Design of Aircraft*. Pearson Education, 2002.
- [132] MATLAB. *version 9.7 (R2019b)*. The MathWorks Inc., Natick, MA, USA, 2019.
- [133] H. B. N. Søren N. Lophaven and J. Søndergaard. Dace - a matlab kriging toolbox. Technical Report IMM-TR-2002-12, Technical University of Denmark, August 2002. Version 2.0.

# Appendix A

## Geometric parameterization

The entire parameterization of the aircraft was performed in MATLAB. Three orthogonal dimensions were considered,  $x$ ,  $y$  and  $z$ , corresponding to the chordwise, spanwise and transverse directions of the aircraft, respectively. Also, the origin of the referential is the leading edge point of the wing root airfoil, assuming an incidence of zero degrees.

The parameterization of the airfoils will be identical for all lifting surfaces plus the vertical stabilizer, being these, wing, winglets canard and fin. Each airfoil will correspond to a NACA Four-Digits airfoil [128]. In the NACA Four-Digit series, the first digit corresponds to maximum camber ( $cbr$ ) in percentage of the chord ( $c$ ), the second specifies the maximum camber position ( $p$ ) in tenths of chord, and finally, the last two digits indicate the maximum airfoil thickness ( $t$ ) in percentage of the chord. The mean camber line ( $z_{cbr}$ ) and thickness distribution ( $z_t$ ) are defined by equations A.1 and A.2, respectively:

$$\begin{cases} z_{cbr} = \frac{cbr}{p^2}(2px - x^2) & , 0 \leq x < p \\ z_{cbr} = \frac{cbr}{(1-p^2)}[(1-2p) + 2px - x^2] & , p \leq x \leq c \end{cases} \quad , \quad (\text{A.1})$$

$$z_t = \pm \frac{t}{0.2}(0.2969\sqrt{x} - 0.1260x - 0.3516x^2 + 0.2843x^3 - 0.1015x^4) . \quad (\text{A.2})$$

Having this, the upper and lower surface points are given by equation A.3, where the subscripts  $u$  and  $l$  refer to the upper and lower surfaces, respectively and  $\theta$  corresponds to the angle between the  $x$  axis and the tangent to the mean camber line and is defined as presented in equation A.4:

$$\begin{cases} x_u = x - z_t \sin\theta \\ z_u = z_{cbr} + z_t \cos\theta \\ x_l = x + z_t \sin\theta \\ z_l = z_{cbr} - z_t \cos\theta \end{cases} \quad , \quad (\text{A.3})$$

$$\theta = \tan^{-1} \left( \frac{dz_{cbr}}{dx} \right) . \quad (\text{A.4})$$

For every different airfoil in the aircraft, a non-dimensional airfoil with an unitary chord is generated.

A total of 200 points are considered to define each airfoil. The coordinates of said airfoil points are then multiplied by the chord at a determined location, thus sizing the airfoil to scale.

## A.1 Wing

Like mentioned in section 3.1.3, the chord, twist and thickness distributions of the wing skin and spars are defined with four parameters each, specifically, the value at the root, the value at the tip, as well as the value and position of the discontinuity. It is then possible to define a bilinear distribution, like seen in equation A.5 for the chord  $c$ , for example:

$$\begin{cases} c(y) = \frac{c_{discw} - c_{rootw}}{y_{c_{disc}}} y + c_{rootw} & , 0 \leq y \leq y_{c_{disc}} \\ c(y) = \frac{c_{tipw} - c_{discw}}{\frac{b_w}{2} - y_{c_{disc}}} y - \frac{c_{tipw} - c_{discw}}{\frac{b_w}{2} - y_{c_{disc}}} \frac{b_w}{2} + c_{tipw} & , y_{c_{disc}} < x \leq \frac{b_w}{2} \end{cases} \quad (A.5)$$

In equation A.5,  $y$  represents the spanwise position and  $y_{c_{disc}}$  is the position of the chord discontinuity. The same reasoning is used for the twist, skin and spar thickness distributions, replacing the variable  $c$  for  $\gamma$ ,  $thk_{skin}$  and  $thk_{spar}$ , respectively. The position of the discontinuity of both thickness distributions is the same used for the chord distribution.

The wing airfoil is constant along the whole wing, and the only fixed parameter is the maximum camber position ( $p_w$ ), which is located at 40% of the chord. Considering the bilinear chord distribution, three airfoils were sized, positioned and rotated in order to generate the wing, one at the root, one at the discontinuity and other at the tip. The wing spars are placed perpendicular to the chord line in each airfoil according to their position. The 100 airfoil points on the upper camber are iterated to find the two points that are before and after the spar chordwise position, respectively. The coordinates of the spar points are then interpolated from the coordinates of those two points. If one the airfoil points corresponds exactly to the position of the spar, its coordinates are used instead. An identical procedure is applied to the lower camber, thus identifying a total of four points that define the two spars in each spanwise section.

Equation A.6 depicts the process of airfoil generation, and allows the determination of the airfoil points final coordinates  $[x_{aflw}, z_{aflw}]$  for each spanwise position:

$$\begin{cases} x_{aflw}(y) = [(adx_{aflw} \times c(y) + \tan(\Lambda_w) \times y) - x_{rot}(y)] \cos(\gamma(y)) \\ \quad + adz_{aflw} \times c(y) \sin(\gamma(y)) + x_{rot}(y) \\ z_{aflw}(y) = -[(adx_{aflw} \times c(y) + \tan(\Lambda_w) \times y) - x_{rot}(y)] \sin(\gamma(y)) \\ \quad + adz_{aflw} \times c(y) \cos(\gamma(y)) \end{cases} \quad (A.6)$$

where,  $[adx_{aflw}, adz_{aflw}]$  are the coordinates of the non-dimensional wing airfoil located at the origin,  $\Lambda_w$  is the wing sweep angle,  $\gamma(y)$  is the wing twist angle at the spanwise position  $y$  and  $x_{rot}(y)$  is the chordwise position of the elastic axis, assumed to be located at 30% of the chord line at each spanwise section.

A wingbox extension to the region inside the fuselage is also considered. The wingbox section at

the wing root is extended, perpendicularly to the airfoil section, to the symmetry plane of the aircraft, which is located at a distance of  $d_{fuse}/2$  to the wing root, with  $d_{fuse}$  being the spanwise dimension of the fuselage. This dimension is defined as  $d_{fuse} = y_{scale} \times 0.17m$ , where  $0.17m$  is the spanwise dimension of the original fuselage from [1].

The wing aerodynamic center is assumed to be above the CoG at a distance of  $z_w = 0.07m$ , while the horizontal distance  $l_w$  is obtained from the calculation of the aerodynamic loads in trim conditions with Prandtl's LLT (section 2.1.2.1). These two parameters fully define the position of the wing.

## A.2 Winglet

Identically to the wing airfoil, the maximum camber position of the winglet  $p_{wgl}$  is the only fixed airfoil parameter for the winglet, and also equal to 40% of the chord.

The spanwise distance, as well as the vertical distance (in the  $z$  axis), between the leading edge of the winglet root section and the wing tip are both equal to  $r = 0.05m$ , like seen in figure A.1. The chord line of the winglet is then located at  $y = b_w/2 + r$ .

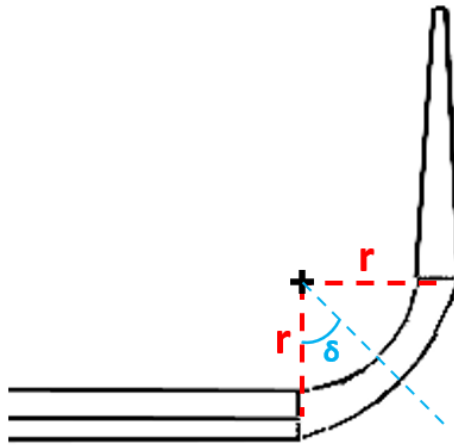


Figure A.1: Winglet position.

The winglet root chord  $c_{root_{wgl}}$  is calculated by extending the wing chord distribution to the a position of  $y = b_w/2 + r$ :

$$c_{root_{wgl}} = \frac{c_{tip_w} - c_{disc_w}}{\frac{b_w}{2} - y_{disc}} r + c_{tip_w} . \quad (A.7)$$

As the winglet chord distribution is parameterized by the taper ratio  $\lambda_{wgl}$ , only two sections are required to define the winglet, in particular, the root and tip sections. The winglet tip chord is then given by  $c_{tip_{wgl}} = c_{root_{wgl}} \lambda_{wgl}$ .

The chordwise distance between the leading edge at the wing tip and the leading edge at the winglet root, is also determined by considering an extension of the wing leading edge sweep, allowing to parameterize the airfoils at the root ( $z' = 0m$ ) and at the tip of the winglet ( $z' = b_{wgl}$ ):

$$\begin{cases} x_{aflwgt}(z') = adx_{aflwgt} \times c(z') + \tan(\Lambda_w) \times (b_w/2 + r) + \tan(\Lambda_{wgt}) \times z' \\ y_{aflwgt}(z') = ady_{aflwgt} \times c(z') + \frac{b_w}{2} + r \end{cases} \quad (A.8)$$

The transition between the wingtip and the root of the winglet is created by considering the sizing of airfoil sections and posterior rotation of 25 angular increments  $\delta$  (figure A.1), with  $\delta \in [0; 85]$  degrees. The non-dimensional airfoil used for this area is the same as for the wing, and the twist is identical to the wingtip twist  $\gamma_{tip}$ .

Like before, the chord at each position is obtained from the wing chord distribution at the tip, and depends on the spanwise position, which in turn is determined by  $\delta$ :

$$y = \frac{b_w}{2} + r \sin \delta, \quad (A.9)$$

$$\Rightarrow c_{trans}(\delta) = \frac{c_{tip_w} - c_{disc_w}}{\frac{b_w}{2} - y_{disc}} r \sin \delta + c_{tip_w}. \quad (A.10)$$

The transition airfoil points coordinates require a transformation in all three dimensions due to the rotation  $\delta$ . The sizing and positioning of the airfoils at each section is then given by equation A.11:

$$\begin{cases} x_{afl_{trans}}(\delta) = \left[ adx_{afl_w} \times c_{trans}(\delta) + \tan(\Lambda_w) \times \frac{b_w}{2} - x_{rot}(y) \right] \cos(\gamma_{tip}) \\ \quad + adz_{afl_w} \times c_{trans}(\delta) \sin(\gamma_{tip}) + x_{rot}(y) + r \sin \delta \tan(\Lambda_w) \\ y_{afl_{trans}}(\delta) = \frac{b_w}{2} + r \sin \delta \\ z_{afl_{trans}}(\delta) = - \left[ adx_{afl_w} \times c_{trans}(\delta) + \tan(\Lambda_w) \times \frac{b_w}{2} - x_{rot}(y) \right] \sin(\gamma_{tip}) \\ \quad + adz_{afl_w} \times c_{trans}(\delta) \cos(\gamma_{tip}) + r(1 - \cos \delta) \end{cases} \quad (A.11)$$

The wing-winglet transition is terminated by linearly connecting the winglet root airfoil points with the corresponding transition airfoil points for  $\delta = 85^\circ$ .

### A.3 Canard

The position of the canard is fully defined by the longitudinal and vertical distances between the aerodynamic centers of the two lifting surfaces,  $l_c$  and  $z_c$ , respectively. Both these distances are set as design variables. Like the wing, the aerodynamic center of the canard is assumed to be at 25% of the chord.

Regarding the canard airfoil, the only design variable is the maximum camber  $cbr_c$ , as the maximum camber position is set as  $p_c = 0.4$  and the airfoil relative thickness is also fixed at  $t_c = 0.12$ . Two identical airfoils are generated in order to represent the canard, one at  $y = 0$  and other at  $y = b_c/2$ .

The constant chord of the canard is obtained by dividing its surface area by the span (equation A.12), which are both set as design variables:

$$c_c = \frac{S_c}{b_c}. \quad (A.12)$$

The canard tube outer circumference is generated similarly to the airfoils, as 200 points are considered for each section. And also like the airfoils, two circumferences are generated, one at  $y = 0$  and other at  $y = b_c/2$ . The tube is centered at the aerodynamic center of the canard and the 200 points are placed by considering rotation increments of  $\phi_c$  with a radius of  $r_{tube}$  and  $\phi_c \in ]0; 360]$  (figure A.2). Thus, the two-dimensional coordinates of the tube section are determined by equation A.13:

$$\begin{cases} x_{tube}(\phi_c) = r_{tube} \cos \phi_c - (l_c - 0.25c_{root_w}) \\ z_{tube}(\phi_c) = r_{tube} \sin \phi_c + z_c \end{cases} \quad (A.13)$$

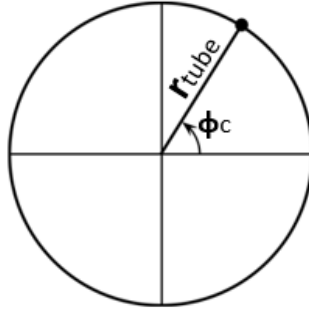


Figure A.2: Canard tube section parameterization.

The lower and upper bounds of the variable  $z_c$  mentioned in table 3.2 of section 3.1.3, i.e.,  $pos_{bot}$  and  $pos_{top}$ , correspond to the positions on the fuselage spar with a safety margin of  $s_{mg} = 5mm$  to the lower and upper edges, respectively, measured from the aerodynamic center of the wing. The geometry of the fuselage spar is displayed in figure A.3. Thereby,  $pos_{bot}$  and  $pos_{top}$  are determined by equation A.14:

$$\begin{cases} pos_{bot} = z_{f_{spar}} - h_{fuse} + r_{tube} + s_{mg} \\ pos_{top} = z_{f_{spar}} - r_{tube} - s_{mg} \end{cases} \quad (A.14)$$

where,  $z_{f_{spar}}$  and  $h_{fuse}$  are the coordinate of the top point of the front spar at the wing root section in the  $z$  axis, which corresponds to the coordinate of top edge of the fuselage spar, and the height of the fuselage spar measured in the  $z$  axis, respectively.

## A.4 Fin

Identically to the winglet, the fin can be completely defined by two airfoil sections, as the airfoil parameters are constant and fixed and the chord distribution is characterized by the taper ratio  $\lambda_f$ . The airfoil is symmetric, meaning that  $cbr_f = 0$  and  $p_f = 0$ , and also the relative thickness is set as  $t_f = 0.10$ . The chord at the root,  $c_{root_f}$ , and at the tip,  $c_{tip_f} = c_{root_f} \lambda_f$  are used to dimension the two airfoil sections.

The fin has one spar located at 70% of the chord, and it is parameterized the same way as those of the wing.

The position of the fin is such that its root section is aligned with the top of the fuselage spar, being

located at  $z = z_{f_{spar}}$ . Further, the fin is placed symmetrically on the aircraft, meaning that its chord line is on the symmetry plane  $y = -d_{fuse}/2$ . On the other hand, the longitudinal position is determined by the distance between the center of gravity and the aerodynamic center of the fin (assumed to be at 25% of its root),  $l_f$ , which is calculated from the volume coefficient  $C_{VT} = 0.02$ , required for stability [131]:

$$l_f = \frac{C_{VT} b_w S_w}{S_f}, \quad (\text{A.15})$$

where,  $S_f = b_f \bar{c}_f$  is the surface area of the fin. In turn,  $\bar{c}_f$  is the mean aerodynamic chord of the fin and it is given by the following equation:

$$\bar{c}_f = \frac{2}{3} \frac{c_{root_f} (1 + \lambda_f + \lambda_f^2)}{1 + \lambda_f}. \quad (\text{A.16})$$

It is then possible to establish the two-dimensional coordinates of the fin airfoil sections at the root:

$$\begin{cases} x_{afl_f}(z) = adx_{afl_f} \times c_f(z) + l_f - l_w + 0.25c_{root_w} - 0.25c_f(z) \\ y_{afl_f}(z) = ady_{afl_f} \times c_f(z) - \frac{d_{fuse}}{2} \end{cases}. \quad (\text{A.17})$$

## A.5 Fuselage

The outer surface of the fuselage is parameterized by three scaling factors, applied to the three dimensions of the original fuselage shape, in particular,  $x_{dim_i} = 3.49m$ ,  $y_{dim_i} = 0.17m$  and  $z_{dim_i} = 0.12m$ . The parameters  $y_{scale}$  and  $z_{scale}$  are design variables and, identically to the calculation of  $d_{fuse}$  from  $y_{scale}$  and  $y_{dim_i}$ , the height of the fuselage spar is given by  $h_{fuse} = z_{scale} z_{dim_i}$ . Differently, the longitudinal sizing of the fuselage is done by applying  $x_{scale}$ , which is obtained from equation A.18:

$$x_{scale} = \frac{l_{fuse} + 0.622}{3.49}, \quad (\text{A.18})$$

where,  $l_{fuse}$  is the total length of the fuselage spar and 0.622 the longitudinal distance, in meters, required in the nose of the fuselage to fit the MAD sensor.

A representation of the fuselage spar is shown in figure A.3, where the red markers represent the aerodynamic centers of each surface.

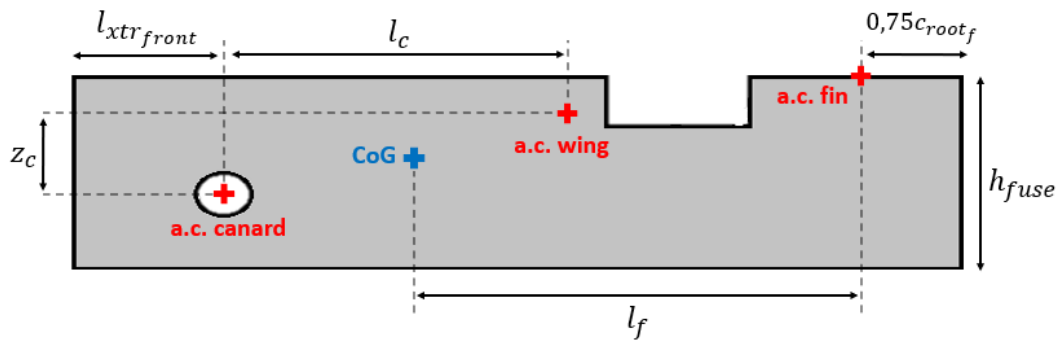


Figure A.3: Geometry of fuselage spar.

The spar is coincident with the wing and canard root sections, being placed at the plane  $y = 0$ . The top edge of the spar is at  $z = z_{f_{spar}}$ , while the lower edge is at  $z = z_{f_{spar}} - h_{fuse}$ . The front edge of the spar is set at a longitudinal distance of  $l_{xtr_{front}} = 5r_{tube}$  to the aerodynamic center of the canard, and the rear edge coincides with the position of the trailing edge of the fin, therefore at a distance of  $0.75c_{root_f}$  to the aerodynamic center of the fin. Thus, the total length of the fuselage spar is determined by:

$$l_{fuse} = l_{xtr_{front}} + l_c - l_w + l_f + 0.75c_{root_f} . \quad (\text{A.19})$$

## A.6 Stacking of laminate layers

The number and type of layers of each component of the structure of the aircraft is defined by the thickness, stacking sequence and minimum number of layers set for each component.

First, the laminate is generated with the minimum number of layers and the laminate thickness is calculated by multiplying the number of layers of each type of carbon fiber sheet by the corresponding nominal thickness  $h_n$ .

Some structural elements have their required thickness determined by the design variables. In these cases, if the required thickness is bigger than the laminate thickness, a new layer is added, according to the stacking sequence, and the new laminate thickness is now equal to the previous plus  $h_n$  of the added layer. This process is repeated until the laminate thickness is larger or equal to the required thickness of that component.

